Assessing solar radiation components over the alpine region

Advanced modeling techniques for environmental and technological applications.

Mariapina Castelli

UNIVERSITY OF TRENTO - Italy

Department of Civil, Environmental and Mechanical Engineering

2015

Doctoral thesis in Environmental Engineering, XXVI cycle

Faculty of Engineering, University of Trento

Academic year 2014/2015

Supervisors:
Prof. Dino Zardi, University of Trento
Dott. Marcello Petitta, European Academy of Bolzano

University of Trento

Trento, Italy

2015

To my little daughter Viola,
who taught me to catch nimbly the flying time,
and to my sweet husband Marco,
the safety net of my acrobat's life.

Acknowledgments

Contents

List of Figures

List of Tables

Summary

This thesis examines various methods for estimating the spatial distribution of solar radiation, and in particular its diffuse and direct components in mountainous regions. The study area is the Province of Bolzano (Italy). The motivation behind this work is that radiation components are an essential input for a series of applications, such as modeling various natural processes, assessing the effect of atmospheric pollutants on Earth's climate, and planning technological applications converting solar energy into electric power. The main mechanisms that should be considered when estimating solar radiation are: absorption and scattering by clouds and aerosols, and shading, reflections and sky obstructions by terrain. Ground-based measurements capture all these effects, but are unevenly distributed and poorly available in the Italian Alps. Consequently they are inadequate for assessing spatially distributed incoming radiation through interpolation. Furthermore conventional weather stations generally do not measure radiation components. As an alternative, decomposition methods can be applied for splitting global irradiance into the direct and diffuse components. In this study a logistic function was developed from the data measured at three alpine sites in Italy and Switzerland. The validation of this model gave MAB = 51 Wm^{-2}, and MBD = -17 Wm^{-2} for the hourly averages of diffuse radiation. In addition, artificial intelligence methods, such as artificial neural networks (ANN), can be applied for reproducing the functional relationship between radiation components and meteorological and geometrical factors. Here a multilayer perceptron ANN model was implemented which derives diffuse irradiance from global irradiance and other pre-

dictors. Results show good accuracy (MAB $\in$ [32, 43] Wm^{-2}, and MBD$\in$ [-7, -25] Wm^{-2}) suggesting that ANN are an interesting tool for decomposing solar radiation into direct and diffuse, and they can reach low error and high generality. On the other hand, radiative transfer models (RTM) can describe accurately the effect of aerosols and clouds. Indeed in this study the RTM libRadtran was exploited for calculating vertical profiles of direct aerosol radiative forcing, atmospheric absorption and heating rate from measurements of black carbon, aerosol number size distribution and chemical composition. This allowed to model the effect of aerosols on radiation and climate. However, despite their flexibility in including as much information as available on the atmosphere, RTM are computationally expensive, thus their operational application requires optimization strategies. Algorithms based on satellite data can overcome these limitations. They exploit RTM-based look up tables for modeling clear-sky radiation, and derive the radiative effect of clouds from remote observations of reflected radiation. However results strongly depend on the spatial resolution of satellite data and on the accuracy of the external input. In this thesis the algorithm HelioMont, developed by MeteoSwiss, was validated at three alpine locations. This algorithm exploits high temporal resolution METEOSAT satellite data (1 km at nadir). Results indicate that the algorithm is able to provide monthly climatologies of both global irradiance and its components over complex terrain with an error of 10 Wm^{-2}. However the estimation of the diffuse and direct components of irradiance on daily and hourly time scale is associated with an error exceeding 50 Wm^{-2}, especially under clear-sky conditions. This problem is attributable to the low spatial and temporal resolution of aerosol distribution in the atmosphere used in the clear-sky scheme. To quantify the potential improvement, daily averages of accurate aerosol and water vapor data were exploited at the AERONET stations of Bolzano and Davos. Clear-sky radiation was simulated by the RTM libRadtran, and low values of bias were found between RTM simulations and ground measurements. This confirmed

that HelioMont performance would benefit from more accurate local-scale aerosol boundary conditions. In summary, the analysis of different methods demonstrates that algorithms based on geostationary satellite data are a suitable tool for reproducing both the temporal and the spatial variability of surface radiation at regional scale. However better performances are achievable with a more detailed characterization of the local-scale clear-sky atmospheric conditions. In contrast, for plot scale applications, either the logistic function or ANN can be used for retrieving solar radiation components.

Chapter 1

Introduction

1.1 Aim of the thesis

The research project behind this thesis raised from the demand of spatially distributed solar radiation in the Alps for computing the photovoltaic (PV) potential at the regional scale. Since atmospheric aerosols and clouds modify the quality and quantity of surface radiation, we specifically focused on estimating the influence of the atmosphere on surface incoming radiation and on climate. In addition, another application requiring radiation data which motivated the present work is the modeling of land-atmosphere exchanges of water and carbon, which requires net radiation as input. From these two fields, two more specific research interests derived, which drove the focus of this thesis on discriminating the diffuse and direct components of irradiance: from one side, studying the performances of different technologies converting radiation into electric power, which respond variously to direct and diffuse radiation, and from the other side examining the effect of climate change, and of the consequent different levels of diffuse radiation, on photosynthesis and evapotranspiration.

This thesis is a first attempt to satisfy these requirements by answering to the following questions:

- Which are the necessary theoretical bases for modeling solar radiation?

- What is the coverage of ground based measurement instruments in the area of interest?

- How reliable are decomposition methods and artificial neural networks for retrieving radiation components in this region?

- How can we characterize and model the effects of atmospheric aerosols on solar radiation?

- How can we model spatially distributed irradiance in the Alps?

- Which are the expected performances of the state-of-the-art remote sensing based algorithms for modeling surface incoming solar radiation?

- Is it possible to enhance the performances of these algorithms?

1.2 Outline of the thesis

The structure of this thesis is the following:

Chapter 1 describes the importance of solar radiation data in different fields and introduces the estimation methods which are examined and tested in this thesis.

Chapter 2 presents the main definitions and units used for working with solar radiation. Furthermore it discusses the factors affecting the incoming solar radiation, i.e. the atmosphere, clouds and topography.

Chapter 3 describes ground based instruments used for measuring solar radiation and its components. In addition it evaluates the availability of ground based data in the study area.

Chapter 4 summarizes two experiments: in the first the diffuse fraction of solar radiation was estimated by decomposition models, and in the second

artificial neural networks were exploited, with global irradiance and other meteorological parameters as input features.

Chapter 5 illustrates the equation of radiative transfer and one particular radiative transfer model which is used in this work, namely libRadtran.

Chapter 6 reports on the estimation of radiative forcing and heating rate of measured aerosol profiles, performed by libRadtran.

Chapter 7 deals with satellite remote sensing of incoming radiation in general, and in particular with the HELIOSAT method and its latest formulation, called HelioMont, which was proposed by MeteoSwiss.

Chapter 8 presents the validation of the algorithm HelioMont performed at some measurement sites in the Alps. Furthermore it proposes improvements in the clear-sky model, which are based on an optimization of the input data on atmospheric aerosols.

Chapter 9 draws up important conclusions from the present work and discusses the potential for future applications.

1.3   The importance of solar radiation data

Solar radiation is the main energy source for the Earth. Radiation entering the Earth's atmosphere is partly absorbed, partly scattered, and partly reflected by atmospheric gases, aerosols and clouds. The portion of radiation reaching the surface is absorbed and reflected by land and oceans. In order to maintain the long-term quasi-static equilibrium of the climate system, the absorbed energy must be balanced by an equal amount of energy emitted to the space by the atmosphere and the surface of the Earth (Peixoto and Oort, 1992). Since solar energy governs the radiative balance of the Earth's atmosphere and surface, an accurate estimation of the incoming radiation is a key requirement for climate monitoring. Furthermore,

many hydrological, biophysical and biochemical processes on the Earth surface are driven by solar radiation, with feedbacks to the rest of the climate system (Bonan, 2002).

These processes include the diurnal development of the atmospheric boundary layer (ABL), which is the lowest part of the troposphere whose thermodynamics and kinematics undergo pronounced diurnal changes in response to the exchanges of energy, mass and momentum between the atmosphere and the Earth surface. Most of the ABL turbulence is driven by forcings from the ground. In fact solar heating of the ground during the day causes the rise of warmer air and the formation of large eddies. In mountainous areas solar radiation is also responsible for thermally driven flows over complex terrain (Serafin and Zardi, 2010a,b, 2011). In fact, the inhomogeneous heating of a valley generates a baroclinic atmosphere. In this conditions air density depends not only on pressure, but also on temperature, whose variations can produce vorticity.

The spatial and temporal quantification of solar radiation is required for planning and modeling purposes in various areas, such as agriculture, forestry and oceanography. Solar radiation, in fact, is a main driver for plant photosynthesis and evapotranspiration (Sellers et al., 1997). The efficiency of photosynthesis depends on the solar spectrum, and in particular on the amount of photosynthetically active radiation (PAR), which denotes solar radiation in the spectral range between 400 and 700 nm. Land surface evapotranspiration, which is a major input in soil water balance analyses, includes transpiration from vegetation, evaporation of water intercepted by the canopy of plants and trees, evaporation from the soil surface and evaporation from small water surfaces. Its estimation has a wide range of applications in hydrological modeling, drought monitoring, water resource management, ecosystem health assessment, and crop yield forecasting. In models quantifying evapotranspiration, solar radiation in an important input, together with other meteorological variables and soil properties (Carrer et al., 2012; Sellers et al., 1996; Anderson et al., 2011). Solar radiation, in fact, is one compo-

nent of net radiation, which is balanced by sensible, latent, and conduction heat fluxes in the energy balance of a surface.

The assessment of solar energy is also essential in applications converting solar radiation into electricity, such as PV plants and Concentrated Solar Power (CSP) systems. In last decades the production of power from PV and CSP is being more and more identified as a main contributor to the future energy mix. In fact PV produce 2% of the demand in Europe and roughly 4% of peak demand, and 44832 GWh of electricity from solar PV power were produced in 2011. PV systems offer manifold benefits, e.g. they exploits an unlimited energy source, they are available all over the world, during operation they produce electricity with no waste production nor air pollution. Furthermore, also considering the whole life cycle, PV has a low carbon footprint (16-32 g CO_2 per kWh) compared to fossil fuels (300-1000 g CO_2 per kWh) (Alsema et al., 2006). Another advantage is that as a relatively young, high-tech industry, PV helps job creation and economy strengthening. However the production of power from PV plants and CSP systems is not competitive with other sources of energy because of the high costs of the active solar materials. Beside the current research on innovative and more economic semiconductor materials, another way towards abating the costs of solar power is working for more accurate estimation of the solar resource. In fact, the evaluation of the direct and diffuse components of solar radiation is essential for supporting the choice of the best available technology, i.e. the one that most effectively exploits the radiation available in a target area. Conventional CSP systems, for example, only exploit direct radiation, although the hybrid arrangement of visible and infrared absorbing solar cells is currently being explored (Barber et al., 2011). In contrast flat plate PV modules also use the diffuse component, but their cost is proportional to the efficiency and to the active surface. Furthermore the correct estimation of the daily and seasonal cycle of solar radiation allows an efficient integration of PV systems into the electricity grid, because it demonstrates to which

extent PV plants meet the electrical grid peak demand and contribute to cover it.

In the next subsections the main methods for assessing surface incoming solar radiation are introduced. This thesis tests and exploits the following methods in the Alps.

1.4 Ground based measurements of radiation

Ground based radiometers are the most used instruments for monitoring solar irradiance at surface. The expected error in irradiance measurement is due to the difference between operation and calibration conditions. For high quality and well maintained instruments, the World Meteorological Organization (WMO) guidelines admit maximum errors in the hourly radiation totals of 3% (World Meteorological Organization, 2008). Unfortunately in most cases ground networks of radiometers do not cover sufficiently the area of interest. For example in the province of Bolzano, in the Italian Alps, which is the area of major interest for the project which motivated the present work, all measurement stations are located more than 5 km from each other, whereas the spatial autocorrelation of solar radiation is generally less than 1 km (Dubayah, 1992b; Dubayah and Paul, 1995). In addition conventional weather stations usually include global radiometers and only few of them are equipped with radiometers measuring either the diffuse or direct component of radiation.

Considering the limitations of the network of ground based instruments for radiation measurements in such a complex terrain as the Alps, it is necessary to consider other ways for addressing the problem of estimating surface radiation. This means, for instance, working out numerical models simulating the incoming solar radiation on the basis of suitable algorithms, and possibly taking into account ground based measurements. A good model should include the interactions of the extraterrestrial radiation with the Earth's atmosphere and surface. The main actors in this process are the atmosphere, clouds and topography. Atmospheric

gases absorb solar radiation. In addition, Rayleigh scattering by atmospheric molecules and Mie scattering by aerosols and clouds generate diffuse radiation. Clouds scatter visible light, either toward the Earth or back to space, produce surface shadowing, and absorb infrared radiation. In the mountains the effect of topography is crucial due to the high spatial variability of terrain altitude, slope steepness and orientation. Furthermore the shadows from the portion of terrain visible from the target area reduce beam radiation.

1.5 Data-driven decomposition methods

Decomposition models can be used for retrieving the direct and diffuse components where only global radiation is measured. They exploit global irradiance, clearness index, solar elevation and other meteorological or derived variables as predictors. Several methods are available, which can be classified according to the functional type or relation between the diffuse fraction and the predictors: polynomial models (Liu and Jordan, 1960; Skartveit and Olseth, 1987; Reindl et al., 1990), model based on a logistic function (Ridley et al., 2010; Boland et al., 2013), and exponential models (Maxwell, 1987; Perez et al., 1990). Here we consider the first two categories. In addition, we develop a decomposition method which is based on artificial neural networks (ANN). ANN are structures constituted by layers of neurons, which are multiple-input, multiple-output processing units resembling the functionality of biological neurons. In fact, they can adapt themselves to the problem to solve. ANN are mostly exploited for classification problems, clustering, and for approximating non-linear functions.

1.6 Radiative Transfer Modeling

Among the factors influencing the amount of energy available at surface, the interactions of solar radiation with the Earth's atmosphere are of major concern to this

work. They are described by the theory of light scattering for diffuse radiation, and by the Beer-Bouguer-Lambert law for the extinction of the direct component, which are modeled by the differential equation of radiative transfer. This equation states that the intensity of solar radiation traveling through a medium undergoes weakening due to extinction, strengthening due to emission, and deviation due to scattering.

The equation of atmospheric radiative transfer allows for various solutions differing in the modeling of absorption, scattering and emission (Liou, 2002). Numerical codes for implementing these solutions are usually called Radiative Transfer Models (RTMs), and tipically take into account a simplified atmospheric structure. RTMs can be classified according to either the absorption model or the scattering model. As to the former, *line-by-line* (LBL) models (e.g. Stamnes et al. (2000)) numerically integrate individual absorption lines to produce optical depth or transmittance profile as a function of wavelength; *band* models (Kato et al., 1999; Kotchenova et al., 2006) fit to LBL at narrow spectral interval; *fast* models (Saunders et al., 1999; Matricardi et al., 2001) do a statistical fit to LBL model transmittance for different atmospheres for specific instrument bandpass. Concerning the scattering model, *discrete ordinate* models (Stamnes et al., 1988; Spurr, 2008) do not consider radiative intensity as a function of azimuth. They use N streams, the larger N, the better are the result, but the more expensive is the simulation. In *adding/doubling* models (Minnis et al., 1993; Liu and Weng, 2006) the atmosphere is divided into homogeneous layers characterized by a transmission, reflection and source emission function. Reflection and transmission of combined layers are obtained by computing successive reflections between two layers. *Monte Carlo* (Chen and Liou, 2006) models consider light as photons. Absorption, scattering and reflection are described as probability functions. The path of many photons through the atmosphere, taking into account absorption, scattering and reflection is calculated. Due to a large number of photons statistical analysis can

be done. According to the number of photons the Monte Carlo approach can be very accurate, but the computational effort is very high. The disadvantage of using RTMs is that accurate calculations are time consuming, thus not convenient for application to large areas. In addition the most common RTMs consider the atmosphere as plane-parallel, thus only account for vertical variations of physical parameters, while 3-D models, especially useful for describing the horizontal variations of clouds structure, are an emerging research topic and are not yet in operational use.

1.7 Remote sensing of solar radiation

RTMs require a substantial amount of information concerning rapidly changing atmospheric conditions, such as clouds and aerosol properties. However, the radiative forcing of clouds and, to a certain degree, also aerosol properties can be retrieved from satellite observations. In particular, geostationary satellite data offer a high frequency of observation, thus allowing to observe the daily variability of cloud cover. The main drawbacks of using geostationary satellite data are their coarse spatial resolution and large view angles for higher latitudes. These limitations are particularly severe in mountainous regions, where the altitude varies sharply and not only affects surface related parameters, but also the state of the atmosphere. Furthermore satellite radiometers measure visible radiation reflected by the Earth's atmosphere, thus the retrieval of downward radiation at the Earth surface is not trivial, and requires the modeling of the physical interactions between radiation and aerosols, gases and clouds.

The main effort for retrieving solar radiation at the Earth surface from meteorological satellite data was done in the late Eighties (Cano et al., 1986) for Meteosat radiometers data. The idea was to correlate the observed reflectivity of each pixel with its cloudiness. The original radiation retrieval method was called

HELIOSAT and was proposed in many formulations following different sensor generations (Beyer et al., 1996; Hammer et al., 2003; Rigollier et al., 2004), mainly changing the clear-sky model used for calculating cloud free irradiance and the relation between n and K.

One version of HELIOSAT which analyzes the peculiar conditions of mountainous areas was proposed by Dürr and Zelenka (Dürr and Zelenka, 2009) specifically for the Alps. This model includes snow detection, pixel georeferencing, satellite view angle distortion fixing, and terrain shading calculation. Despite its comprehensiveness, this algorithm approximates the transmissivity of the atmosphere only through monthly climatological values of the Linke turbidity coefficient (Remund et al., 2003). The turbidity is included in the empirical clear-sky model of Kasten et al. (1984), and does not affect the procedure used to calculate the diffuse radiation fraction. At the same time a new clear-sky model for HELIOSAT was proposed: the algorithm SOLIS (Müller et al., 2004). The latter is based on RTM simulations of clear-sky irradiance. Later on SOLIS was modified introducing the computationally efficient Look Up Tables (LUT) approach, which means that RTM runs were performed for discrete values of the atmospheric parameters, and then an interpolation was performed in dependence of atmospheric input data. This model was called MAGIC (Müller et al., 2009). Radiation values obtained with the LUT approach differ from the exact RTM solutions by no more than 1-2 Wm^{-2}. Recently MeteoSwiss has coupled the MAGIC clear-sky model with a new processing scheme for the all-sky retrieval of solar radiation at surface (Stöckli, 2013a). This new algorithm is called HelioMont.

Chapter 2

Fundamentals of solar radiation

2.1 Concepts and definitions

Radiation designates all the phenomena describing the transport of energy in space. It is characterized by a frequency, ν, [Hz], and a wavelength, λ, [μm]. ν and λ are inversely proportional to each other, the constant of proportionality being the speed of an electromagnetic wave in vacuum, $c = 2.998 \times 10^8$ ms^{-1}:

$$\nu = \frac{c}{\lambda} \tag{2.1}$$

The electromagnetic spectrum is obtained by classifying radiation according to ν and λ (Figure 2.1)

Consider the radiant energy dE_λ, in the wavelength interval between λ and $\lambda + d\lambda$, that in the time interval dt crosses an element of area dA, in directions limited to the differential solid angle $d\Omega$, which is oriented to an angle θ with respect to the normal to dA (Figure 2.2). This energy is expressed in terms of the monochromatic intensity, or radiance I_λ:

$$dE_\lambda = I_\lambda \cos\theta \, dA \, d\Omega \, d\lambda \, d\theta \tag{2.2}$$

Thus *radiance* is defined as follows:
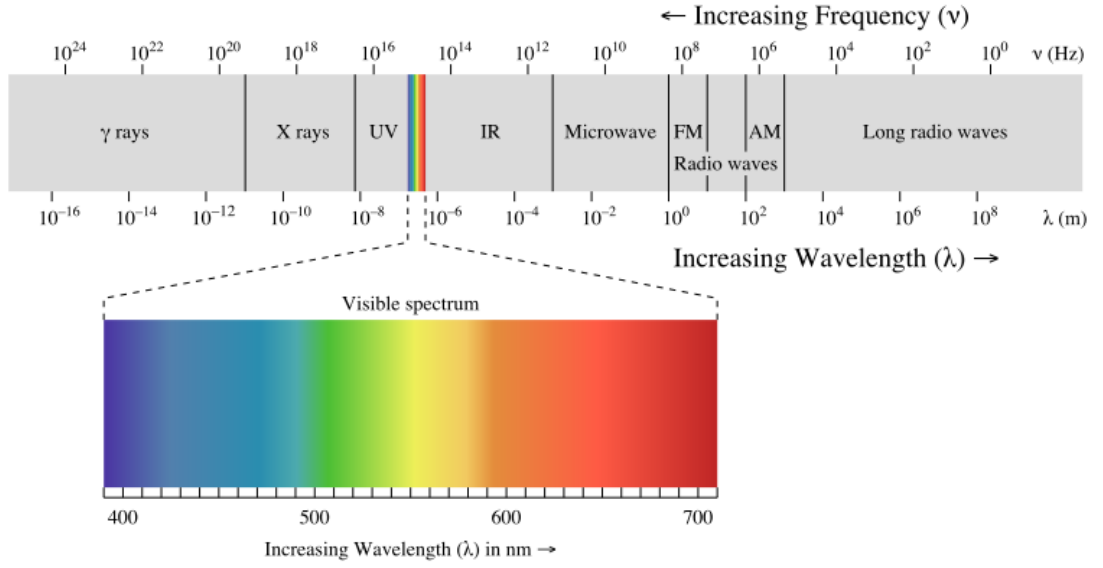
Figure 2.1: Spectrum of electromagnetic radiation. From Wikipedia (2015).

$$I_\lambda = \frac{dE_\lambda}{cos\theta \, dA \, d\Omega \, d\lambda \, d\theta} \qquad (2.3)$$

and is measured in W m^{-3} sr^{-1}.

The *monochromatic irradiance* is defined as the normal component of I_λ integrated over the hemispheric solid angle:

$$F_\lambda = \int_\Omega I_\lambda \, cos\theta \, d\Omega \qquad (2.4)$$

In polar coordinates:

$$F_\lambda = \int_0^{2\pi} \int_0^{\pi/2} I_\lambda(\theta, \, \phi) \, cos\theta \, sin\theta \, d\theta \, d\phi \qquad (2.5)$$

For isotropic radiation:

$$F_\lambda = \pi \, I_\lambda \qquad (2.6)$$

The *total irradiance F* is obtained by integrating the monochromatic irradiance over the electromagnetic spectrum:
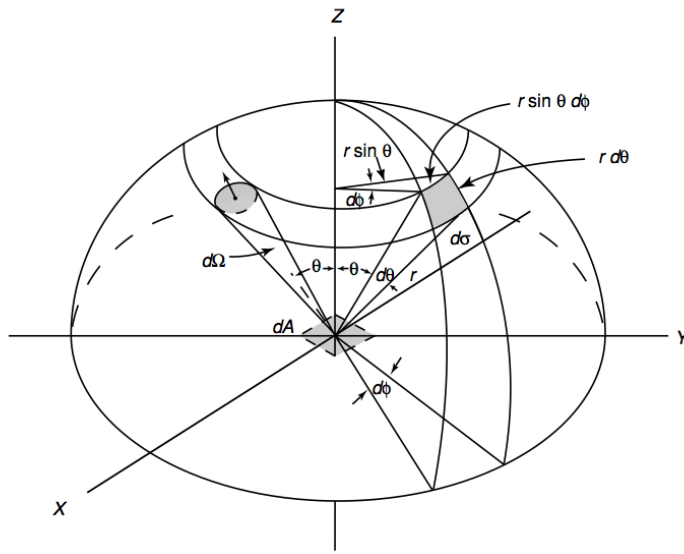
Figure 2.2: Geometry of radiative transfer in polar coordinates (Liou, 2002)

$$F = \int_0^\infty F_\lambda \qquad (2.7)$$

It is measured in W m^{-2}.

2.2 Solar radiation at the top of the atmosphere

The *solar constant S* is the total solar energy reaching the top of the atmosphere. It is defined as the energy per unit time which crosses a surface of unit area normal to the solar beam at the mean distance between the Sun and the Earth.

The Sun emits an irradiance F of 6.2×10^7 Wm^{-2}. If there is no medium between the Sun and the Earth, according to the principle of conservation of energy, the energy emitted from the Sun must remain constant at some distance away, thus also in correspondence of the atmosphere of the Earth:

$$F\,4\,\pi\,a_S^2 = S\,4\,\pi\,r^2 \qquad (2.8)$$

where a_S is the radius of the Sun, and r is the mean Earth-Sun distance. Thus

the solar constant can be expressed as:

$$S = F \left(\frac{a_S}{r} \right)^2 \tag{2.9}$$

In the '70 the solar constant was obtained from total solar irradiance measurements performed by radiometers aboard many satellites, such as Nimbus 7 Earth Radiation Budget (ERB), Solar Maximum Mission Active Cavity Radiometer Irradiance Monitor (SMM ACRIM) 1 and 2, Earth Radiation Budget Experiment (ERBE) aboard the NASA satellites Earth Radiation Budget Satellite (ERBS), NOAA 9 e NOAA 10. From a number of measurements the generally accepted value of 1366 ± 3 Wm^{-2} has been suggested.

Since the irradiance emitted from the Sun can be considered isotropic, according to Equation 2.6 the solar intensity is given by $I = F/\pi$, thus:

$$S = I \pi \left(\frac{a_S}{r} \right)^2 = I \Omega \tag{2.10}$$

where Ω is the solid angle from which the Earth sees the Sun. If a_E is the radius of the Earth, the solar energy intercepted by the Earth is $S\pi a_E^2$. If it is uniformly distributed on the surface of the Earth, the solar energy received per unit area per unit time at the top of the atmosphere is:

$$Q = S \left(\frac{\pi a_E^2}{4 \pi a_E^2} \right) = S/4 \approx 342 \, W m^{-2} \tag{2.11}$$

The solar spectrum is the distribution of radiation as a function of the wavelength. It consists of a continuous emission with thousands of dark absorption lines superposed. The lines are called the Frauenhofer lines, and the solar spectrum is sometimes called the Frauenhofer spectrum. These lines are produced primarily in the photosphere. The total energy emitted by the Sun is approximately equivalent to that of a blackbody at 5782 K. In addition, the visible (VIS) and infrared (IR)

solar radiation fits closely with the blackbody emission at this temperature. However, the ultraviolet (UV) region (< 0.4 μm) of solar radiation deviates greatly from the VIS and IR regions in terms of the equivalent blackbody temperature of the Sun, reaching a minimum of about 4700 K at about 0.14 μm. The energy emitted from the Sun is approximately distributed as follows: 50% in the IR, 40% in the VIS, and 10% in the UV.
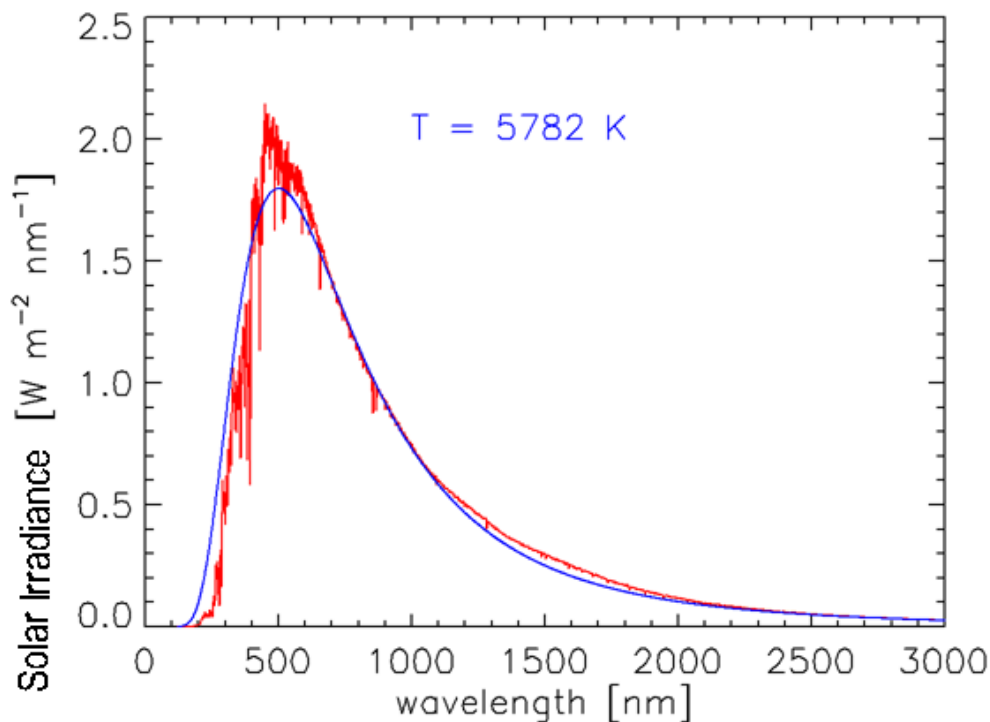
Figure 2.3: The 2000 American Society for Testing and Materials (ASTM) E-490 AM0 (air mass 0) Standard Extraterrestrial Spectrum superimposed to the blackbody emission curve at 5782 K

The solar constant is defined for a mean distance between the Earth and the Sun, d_m, that is 1.496×10^{11} m, but the actual distribution of solar radiation at the top of the atmosphere depends on the eccentricity of the elliptical orbit of the Earth around the Sun. The point of maximum distance (1.521×10^{11} m) is called *aphelion* and the Earth is in this position at the beginning of July. The point of minimum distance (1.471×10^{11} m) is called *perihelion*, and corresponds to the beginning of January.

The irradiance on an horizontal surface at the top of the atmosphere also depends on the sun zenith angle:

$$F_h = F\,cos\theta = S \left(\frac{d_m}{d}\right)^2 cos\theta \qquad (2.12)$$

where F is the irradiance on a plane normal to the solar beam, and d is the actual Earth-Sun distance.

2.3 Atmospheric absorption and scattering

Solar radiation entering the Earth's atmosphere is absorbed and scattered by atmospheric gases, aerosols, clouds, and the Earth's surface.

Atmospheric scattering changes the direction of propagation of radiation. It is generally elastic, which means that the scattered radiation has the same frequency as the incident one. However, a small fraction of photons undergoes inelastic scattering, in which the energy of radiation is also changed due to electronic transitions in the scattering molecules. This is the so called *Raman scattering*. Atmospheric scattering can be due to particles of different size, like gas molecules ($\sim 10^{-4}$ μm), aerosols (~ 1 μm), water droplets (~ 10 μm), and rain drops (~ 1 cm). The effect of particle size on scattering is represented by the so called *size parameter*, x. For a spherical particle of radius a, $x = 2\pi a/\lambda$. If $x << 1$ (particle small compared with the wavelength), the scattering is called *Rayleigh scattering*. An example is the scattering of visible light by atmospheric molecules. If $x \geq 1$ (particle has about the same size as the wavelength) the scattering is called *Lorenz-Mie scattering*. If $x >> 1$ (particle large compared with the wavelength) the scattering is called *Geometric scattering*, and it can be studied by using the geometrical optics of reflection, refraction and diffraction. For low densities of molecules and particles in the air, the scattering is independent, i.e. each particle scatters radiation as if the other particles did not exist. If density increases, like happens inside clouds,

each particle can scatter the radiation that has been already scattered by other particles. This process is called multiple scattering.

Absorption is the conversion of radiation in another form of energy, like heat. Absorption can be due to atmospheric molecules or aerosols. The UV radiation in the interval 0.2-0.3 μm is mainly absorbed by O_3 in the stratosphere. Radiation with λ shorter than 0.2 μm is absorbed by O_2, N_2, O and N. In the troposphere, solar radiation is absorbed in the VIS and IR, mainly by H_2O, CO_2, O_2 and O_3. Figure 2.4 shows the depletion of solar radiation in a cloud and aerosol free atmosphere. The top curve represents the solar spectrum at the top of the atmosphere, and the lower curve represents the solar spectrum at sea level. The difference between the two curves gives the combined effects of absorption and scattering of solar radiation by atmospheric gases. In the UV region the depletion of solar energy is dominated by ozone absorption, in the VIS by Rayleigh scattering, and in the near-IR region, which contains about 50% of solar energy, by water vapor absorption.

Scattering and absorption are often associated. Both processes remove energy from incident radiation, and this attenuation is called *extinction*. In general the amount of energy removed from the original beam of light by a particle is indicated with the *cross section*. The extinction cross section, σ, is the sum of the absorption and scattering cross sections. When the cross section is associated with a particle dimension, its units are expressed in terms of area (cm^2). When it is expressed relative to unit mass, the units are in area per mass (cm^2 g^{-1}), and it is called *mass extinction cross section*, k. When the cross section is multiplied by the particle number density (cm^{-3}), it is called *extinction coefficient*, β, and its units are expressed in terms of length (cm^{-1}).

The angular distribution of light intensity scattered at a given wavelength is called *phase function*, P. If Θ is the scattering angle, i.e. the angle between the incident and scattered waves, P is the ratio between the intensity scattered at the
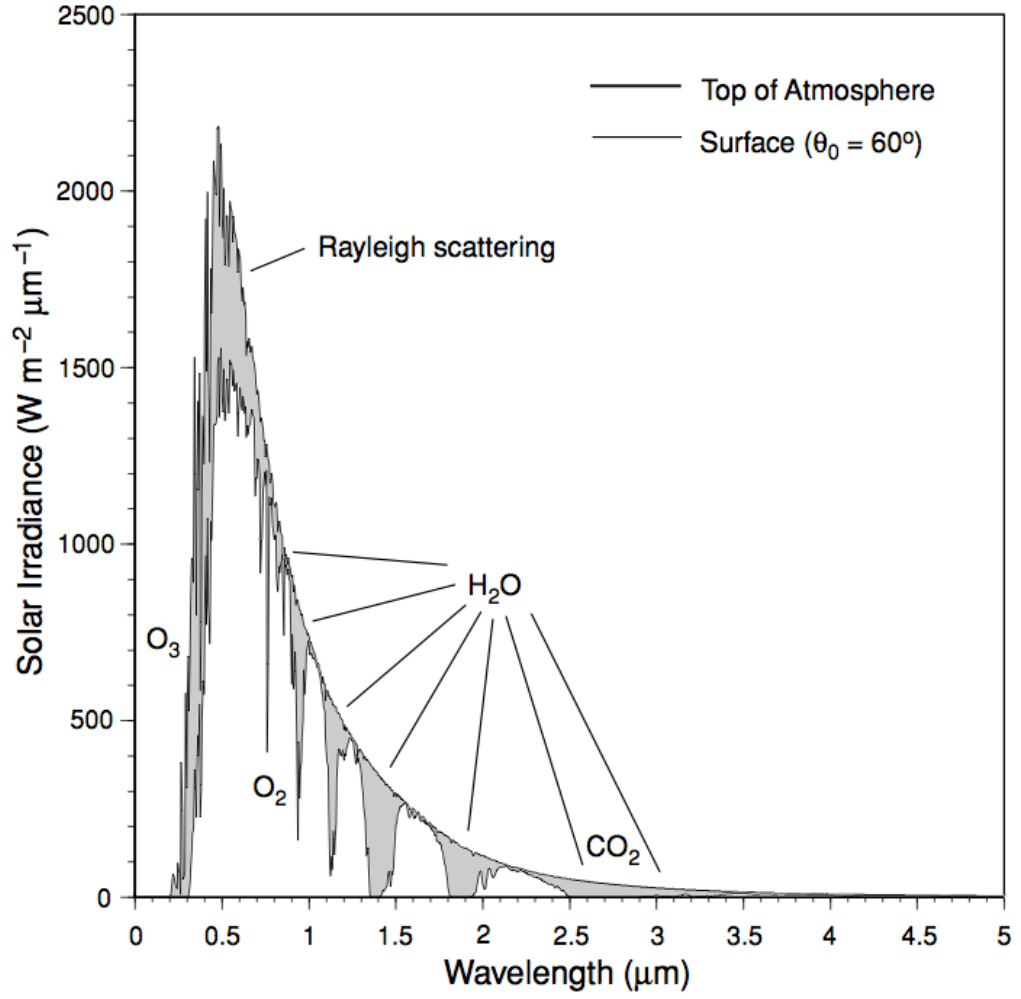
Figure 2.4: Solar irradiance spectrum at the top of the atmosphere and at the surface for a solar zenith angle of 60°, under clear-sky conditions (Liou, 2002).

angle Θ and the total scattered intensity. P is defined so that its integral over the unit sphere centered on the scattering particle is 4π:

$$\int_0^{2\pi} P(\Theta)\, sin\Theta\, d\Theta\, d\phi = 4\pi \qquad (2.13)$$

In terms of scattering cross section, the scattered intensity can be expressed as:

$$I(\Theta) = I_0\, \frac{\sigma_s}{r^2}\, \frac{P(\Theta)}{4\pi} \qquad (2.14)$$

where r is the radius of the spheric scatterer.

2.4 The effect of the Earth's geometry

Solar radiation interacts with the surface of the Earth at two levels:

1. extraterrestrial irradiance is influenced by the geometry of the Earth and its revolution and rotation;

2. irradiance at the Earth's surface is modified by the effects of terrain, including shadowing, elevation, slope and aspect.

The first group of effects depends on the position of the sun above the horizon, which can be calculated by astronomic formulas. Extraterrestrial irradiance falling on a horizontal plane (G_0) varies across the year because of the eccentricity of the Earth's orbit. Introducing a correction factor, (e), which accounts for the changing distance between the sun and the Earth along the ecliptic, G_0 can be expressed as:

$$G_0 = e \, S cos(\theta) \tag{2.15}$$

where:

$$e = 1 + 0.03344 \, cos(j - 0.048869) \tag{2.16}$$

The day angle j is expressed in radians:

$$j = 2 \, \pi \, DOY/365.25 \tag{2.17}$$

and DOY is the day of the year, which varies from 1 on January 1st to 365 (366) on December 31st (**?**).

The second group of effects can be accounted for by a model of the Earth's surface geometry (DEM, Digital Elevation Model) and the exact position of the sun. A complete definition of the angles describing the position of the sun with respect to an horizontal and an inclined surface can be found in Hofierka and Šúri (2002).

Here we briefly describe how the direct and diffuse components of irradiance are modified by the Earth's geometry. The direct component of solar irradiance at the Earth'surface is attenuated, in cloud-free conditions, by atmospheric aerosols and gases. This factors can be accounted for by introducing the Linke turbidity factor, T_L:

$$DIR_0 = S\,e\,exp(-0.8662\,T_L\,m\,\delta_R(m)) \qquad (2.18)$$

where m is the relative optical air mass and $\delta_R(m)$ is the Rayleigh optical thickness, both of which can be calculated according the formulation of Kasten (1996).

Direct irradiance on an horizontal surface, DIR_h, is calculated as:

$$DIR_h = DIR_0\,sin(h_0) \qquad (2.19)$$

where h_0 is the angle between the sun and the horizon (sun elevation).

Direct irradiance on an inclined surface with a solar incidence angle δ_{exp} is calculated as:

$$DIR_i = DIR_0\,sin(\delta_{exp}) \qquad (2.20)$$

Shadow casting and surrounding terrain effect can be described by calculating global irradiance as a combination of its direct and diffuse component as follows:

$$G = \sigma DIR_h + f_{sky}\,DIF_h\,[1 + \alpha\,(1 - f_{sky})] \qquad (2.21)$$

In Equation 5.7 σ is equal to 0 or 1 if the point at the Earth's surface is in shadow, i.e. the sun elevation angle is minor than the local horizon, or sunlit, respectively; f_{sky} is the sky view factor indicating the degree to which the sky is obscured by the surroundings for a given point (Dozier and Marks, 1987); α is the ground albedo, i.e. the ratio of the reflected over the incoming radiation, which is the topic of the next subsection.

2.4.1 Surface albedo

The ground albedo strongly depends on the nature of the surface, and on the spectral and angular distribution of the incoming radiation. The spectral albedo can be expressed as:

$$\alpha = \frac{F_\lambda^{ref}}{F_\lambda^{inc}} \tag{2.22}$$

where F_λ^{rel} is the reflected monochromatic irradiance and F_λ^{inc} is the incident one. Broadband albedo can be expressed as:

$$\alpha = \frac{F^{ref}}{F^{inc}} \tag{2.23}$$

where F^{rel} is the reflected radiative flux and F^{inc} is the incident one.

Reflected light is generated through two processes: Fresnel reflection and scattering. Fresnel reflection describes the process happening between two uniform surfaces with different indexes of refraction. In this case the angle of reflection is equal to the angle of incidence. Diffuse radiation, in contrast, is generated by surface elements whose dimensions are of the same order of magnitude as the wavelengths of incident light. The intensity of the scattered light is only function of the scattering angle, Θ. The distribution of the scattered light is specified in terms of a probability distribution function, which is called phase function and is indicated as $P(\Theta)$. $P(\Theta) sin\Theta d\Theta/2$ represents the fraction of scattered radiation which has been scattered through an angle Θ into an incremental ring of solid angle $d\Omega = 2\pi sin\Theta d\Theta$. The Henyey-Greenstein phase function is an useful formulation for describing the angular distribution of anisotropic scattering:

$$P(g, \Theta) = \frac{1 - g^2}{(1 + g^2 - 2\, g\, cos\Theta)^{3/2}} \tag{2.24}$$

It uses the asymmetry parameter, g, which is an intensity-weighted average of the cosine of the scattering angle (Seinfeld and Pandis, 2012):

$$g = \frac{1}{2} \int_0^\pi cos\Theta \, P(\Theta) \, sin\Theta \, d\Theta \qquad (2.25)$$

For $g = 0$ the scattering is isotropic, for $g < 0$ most of the radiation is scattered backward, and for $g > 0$ most of the radiation is scattered in the forward direction.

If after the first reflection absorption is not so strong, radiation can be scattered multiple times. The effects of single and multiple scattering are described by the empirical formulation of Rahman et al. (1993):

$$\rho(\theta', \theta, \phi) = \rho_0 \frac{cos^{k-1} \theta' \, cos^{k-1} \theta}{(cos\theta' + cos\theta)^{1-k}} \, P(g, \Omega) \, [1 + R(G, \Delta)] \qquad (2.26)$$

where:

$$G(\theta', \theta, \phi) = \sqrt{tan^2\theta' + tan^2\theta - 2tan\theta' \, tan\theta \, cos\phi} \qquad (2.27)$$

and

$$R(G, \Delta) = \frac{1 - \rho_0}{\Delta + G} \qquad (2.28)$$

ρ_0, k Δ and g are empirical coefficients specified in Rahman et al. (1993). θ is the view zenith angle, and θ' is the zenith angle of the incident light that has been scattered in the atmosphere. $\rho(\theta', \theta, \phi)$ is the so-called *bidirectional reflectance distribution function* (BRDF). It is used to generate maps of surface albedo from multi-spectral and multi-angular satellite observations of surface reflectance.

Chapter 3

Ground based measurement of solar irradiance in South Tyrol

3.1 Measurement of radiation components

Ground based measurements allow to monitor solar radiation at point locations accounting for all the geometrical, environmental and atmospheric effects which modify the energy reaching the Earth surface. Regional meteorological services often organize ground based instruments in networks for assessing the spatial distribution of irradiance at regional scale. The usefulness of these networks strongly depends on the spatial density which covers the region of interest, on the quality of the instruments, and on the accuracy of the maintenance procedures.

Direct solar radiation is measured by pyrheliometers, whose receiving surface is normal to the sun beam direction, and whose field of view is limited by an aperture. In order to detect only radiation from the sun and a narrow anulus of sky, WMO recommends that the opening angle is 5° and the slope angle is 1° (World Meteorological Organization, 2008) (Figure 3.1). To measure continuously, pyrheliometers are equipped with a sun tracker following the sun and allowing a rapid adjustment of the orientation of the instrument.
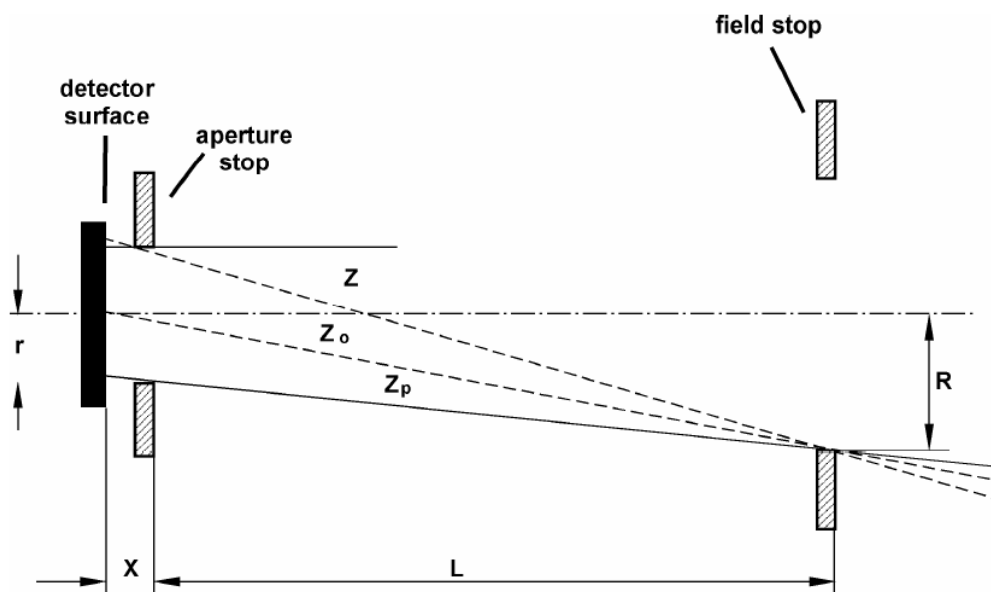
Figure 3.1: View-limiting geometry of a pyrheliometer (Kipp&Zonen, 2008). The opening angle is $2 \times arctan(R/L)$ and the slope angle is $arctan(R-r)/L$.

Global and diffuse radiation are measured by pyranometers (Figure 3.2). The instruments are placed on a plane surface and monitor solar irradiance from a solid angle of 2π sr, in spectral range from 300 to 3000 nm. When measuring the diffuse component, direct radiation is screened by a shading device. Either a static shadow ring or a sun tracker fitted with a small sphere can be used (Figure 3.3).

Pyranometers and pyrheliometers can use different kind of sensors. Pyranometers commonly use thermoelectric, photoelectric, pyroelectric or bimetallic elements as sensors (World Meteorological Organization, 2008). Absolute pyrheliometers, which can define the scale of total irradiance without utilizing reference sources or radiators, use cavities as receivers and electrically calibrated, differential heat-flux meters as sensors. All absolute radiometers measure radiation by comparison to an equivalent amount of electrical power (electrical substitution). The receiving cavity ensures high absorption over the spectral range of interest. Upon absorption of the incident radiation, the cavity experiences a temperature rise. A thermal conductor couples the cavity to an heat sink at a reference temperature.
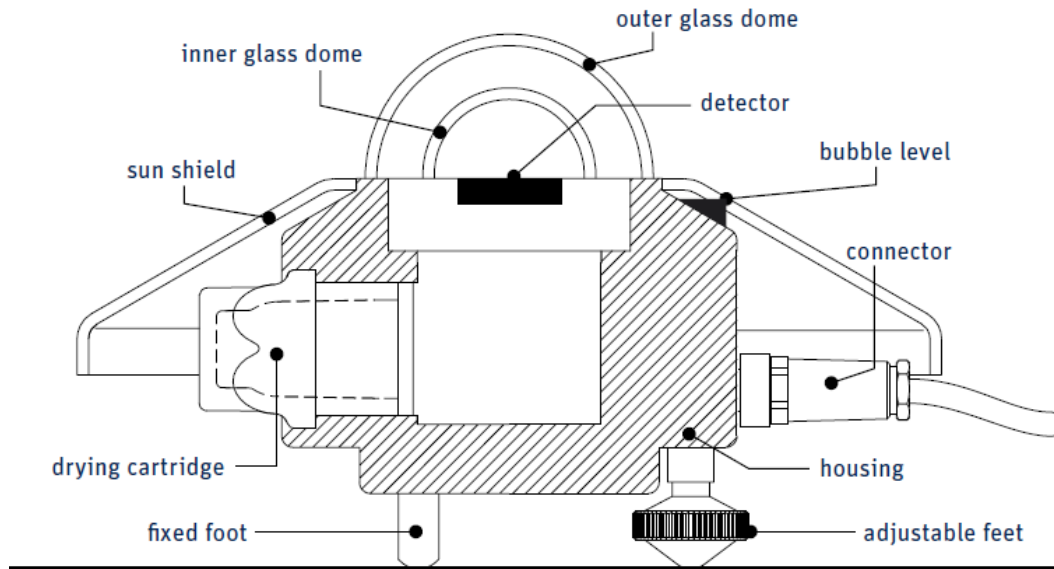
Figure 3.2: Details of a pyranometer (Kipp&Zonen, 2013).

When the light beam is intercepted, an electronic circuit maintains a constant heat flux from the cavity to the heat sink by adjusting the input power, which can be accurately measured.

Most of the radiation sensors used in meteorological stations make use of a detector which is based on a passive thermal remote sensing element, called thermopile. The thermopile warms up responding to the total power absorbed by a black coating, which consists of a non-spectrally selective paint. The coating has many microcavities that trap more than 97% of the incident radiation. The detector, which is made up of a large number of thermocouple junction pairs connected electrically in series, exploits the thermoelectric effect. As the active thermocouple junction (*hot* junction) absorbs thermal radiation, its temperature increases. The temperature of the other junction (*cold* junction) is kept constant. The differential temperature between the hot and the cold junction produces an electromotive force directly proportional to the temperature difference. Irradiance can be calculated dividing the output signal by the sensitivity of the instrument:

$$E \downarrow = \frac{U}{S} \tag{3.1}$$
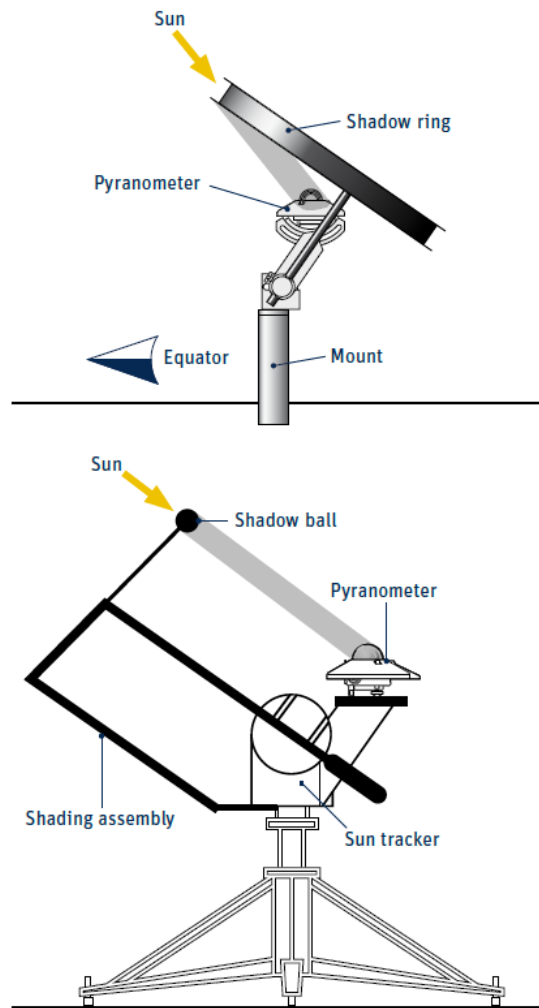
Figure 3.3: Shading devices for intercepting beam irradiance and measuring diffuse irradiance with a pyranometer (Kipp&Zonen, 2013).

where $E\downarrow$ is the irradiance [Wm^{-2}], U is the output of the radiometer [μV] and S is the sensitivity [μVW^{-1}m^2]. The sensitivity of a radiometer, also called calibration factor, depends on the physical properties of the thermopile, which is unique. Therefore each radiometer has unique calibration factor.

The assessment of the quality of radiation measurement is based on the following physical properties of the instrument: sensitivity, stability, response time, cosine response, azimuth response, linearity, temperature response, thermal offset, zero irradiance signal and spectral response (World Meteorological Organization, 2008).

Resolution

The radiometer resolution is the smallest change in radiation which the instrument can detect. It depends on the physical properties of the detector.

Stability

The non-stability is the percentage change in sensitivity over one year. It is due to deterioration of the black coating by UV radiation.

Cosine and azimuth response

The cosine and azimuth response indicate the dependence of the directional response of the instrument on solar elevation and azimuth. Ideally, the response of the detector should be proportional to the cosine of the zenith angle of the solar beam, and constant with azimuth angle.

Linearity

The non-linearity of a radiometer is the percentage deviation in the sensitivity over an irradiance range from 0 to $1000\,\mathrm{Wm^{-2}}$ compared to the sensitivity calibration irradiance of $500\,\mathrm{Wm^{-2}}$. The non-linearity effect is due to convective and radiative heat losses at the black absorber surface which make the conditional thermal equilibrium of the radiometer non-linear.

Temperature response

The temperature dependence is the percent deviation with respect to the calibrated sensitivity at $+20\,°\mathrm{C}$. Some instruments have temperature compensation circuits which maintain a constant response over a large range of temperatures.

Thermal offset

The thermal offset is due to heat currents inside the instrument caused by the variation of the instrument temperature according to ambient temperature. It is quantified as the response in $\mathrm{Wm^{-2}}$ to a $5\,\mathrm{Kh^{-1}}$ change in ambient temperature.

Zero irradiance signal

The zero irradiance signal originates from a temperature difference between the internal components of the instrument. The outer dome is generally colder than the body of the inner absorber. This temperature gradient produces a loss of energy from the absorber, which causes a negative output signal.

Spectral response

The spectral sensitivity is the percentage deviation of the product of spectral absorptance and spectral transmittance from the corresponding mean within the range 300 to 3000 nm.

All radiometric instruments, except the absolute ones, must be calibrated. There are World, Regional and National Radiation Centers which are responsible for the calibration. The World Radiation Centre (WRC) at Davos (CH) is also responsible for maintaining the World Standard Group (WSG), a group of at least four absolute pyrheliometers having different design and long-term stability, which is used to establish the World Radiometric Reference (WRR). The WRR represents the physical units of total irradiance within 99% uncertainty of the measured value. Every five years the regional standards are compared with the WSG, and their calibration factors are adjusted to the WRR. For the calibration of a pyrheliometer, the response of the instrument is compared with the one of an absolute pyrheliometer using the sun as the source. For being used as standard for calibration, absolute instruments must be compared with the WSG and their calibration factors must be adjusted to the WRR. Secondary standards can also be used to calibrate field instruments, but with more uncertainty. Pyranometers are calibrated determining one or more calibration factors and their dependence on environmental conditions, i.e. irradiance, spectral and angular distribution of irradiance, temperature, instrument inclination, net long-wave irradiance for correcting the thermal offset. Different methods of calibration can be used, all of

which require that either the zero irradiance signals of all instruments are known, or pairs of identical pyranometers are used in the same configuration. Details on existing calibration methods can be found in World Meteorological Organization (2008).

3.2   The ground network of pyranometers in South Tyrol

The network of pyranometers installed in the province of Bolzano and managed by the Meteorological Office of the Province is constituted by more than eighty instruments measuring global irradiance. Unfortunately none of them was ever calibrated since the installation, thus the quality of the data is expected to be very low and almost useless for a quantitative assessment. Only few instruments can be used, which were installed during 2009 and collect data without macroscopic measurement error. Figure 3.4 shows the map of these stations, and table 7.1 indicates the name and altitude of the stations included in the map.

Due to the sparse distribution of the measurement stations, the possibility to use this network for an assessment of the spatial distribution of the available solar energy in the province is very limited. The topography of the region, in fact, strongly affects irradiance causing an accentuated small scale spatial variability. Consequently, it is not possible to perform an analysis of the spatial correlation between the stations, which would be necessary for applying geostatistical interpolation techniques, like kriging. Literature shows, in fact, that the spatial autocorrelation of solar radiation in mountainous terrain does not exceed 1 km (Dubayah, 1992a, 1994; Dubayah and van Katwijk, 1992; Dubayah and Paul, 1995; Oliphant et al., 2003), while the distances between available measurement stations are much longer (Figure 3.5).

Figure 3.6 shows the monthly averages and the standard deviation of global solar irradiance at the stations of interest. A maximum between 250 and 300

Wm^{-2} is typically reached in summer, and a minimum between 20 and 60 Wm^{-2} in winter, as expected at this latitude. Most of the signals evidence a local minimum in summer, in general in June. This behavior is associated to the secondary peak of convective precipitations which is typically observed in the Alps, and which was particularly intense in summer 2011.

ID	NAME	ALTITUDE
1	Auer	250
2	Deutschnofen	1470
3	Eyrs - Laas	874
4	Laimburg	224
5	Marienberg	1310
6	Meran Gratsch	330
7	Naturns	541
8	Pfelders	1618
9	Pfinnalm Gsies	2152
10	Plose	2472
11	Sarnthein	970
12	Schlanders	698
13	St. Magdalena in Gsies	1398
14	St. Valentin auf der Haide	1499
15	Stausee Zoggl St. Walburg	1142
16	Sulden	1907
17	Taufers	1235
18	Toblach	1219

Table 3.1: Name and altitude of the ground measurement stations which are mapped in Figure 3.4.
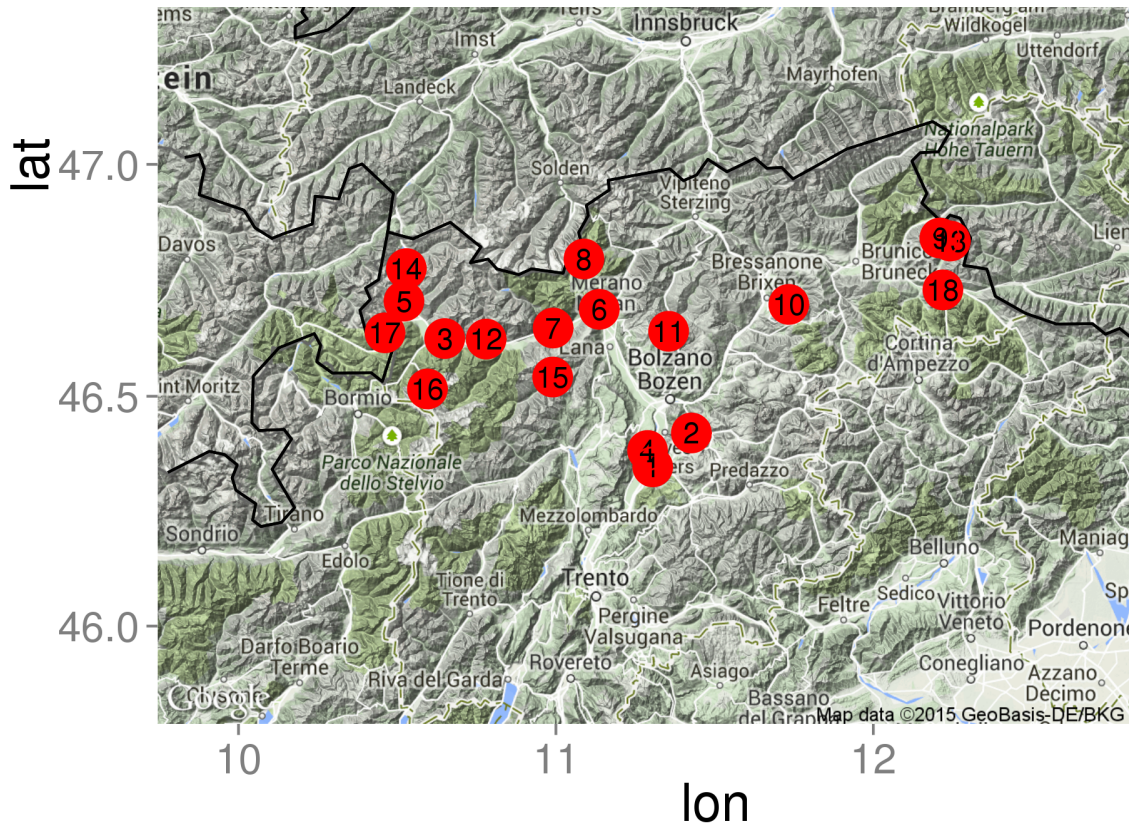
Figure 3.4: Pyranometers of the province of Bolzano which were installed after 2009.
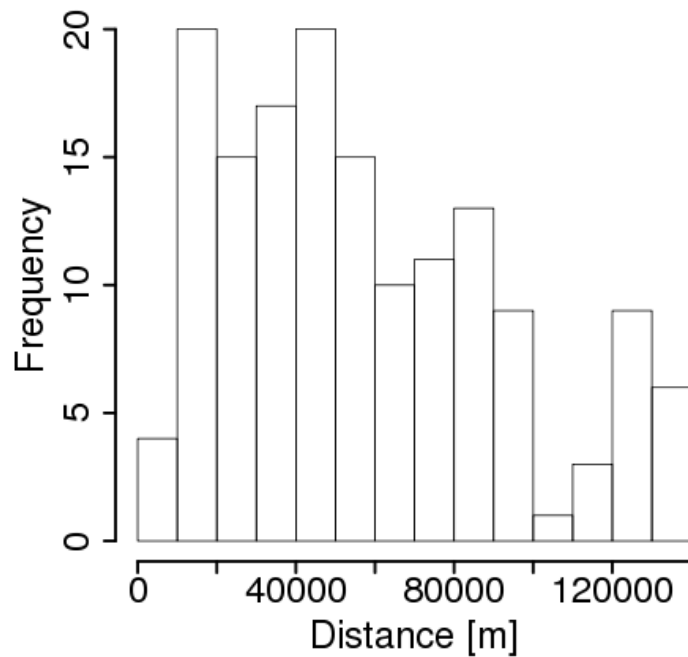
Figure 3.5: Histogram of the distance between measurement stations in South Tyrol.
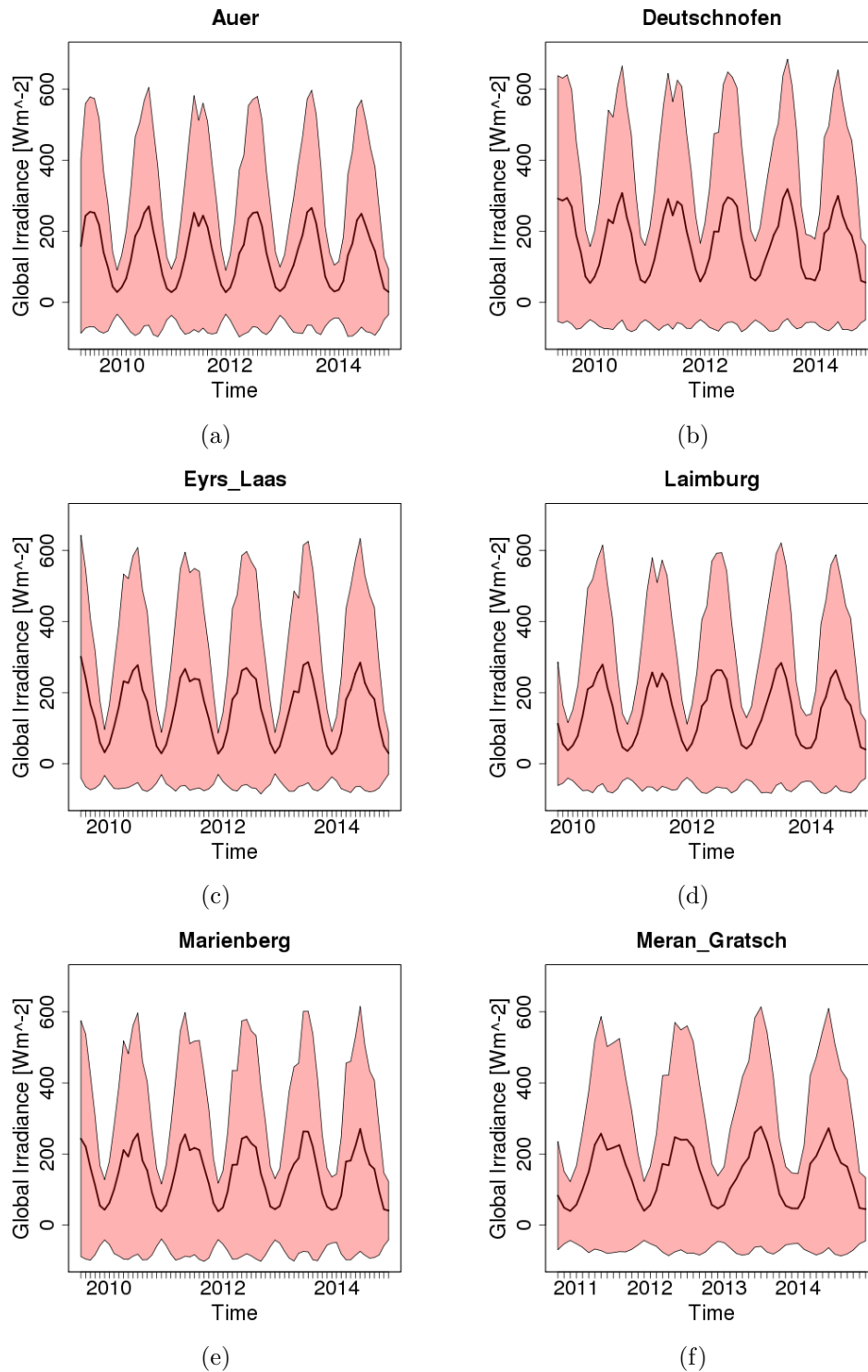
Figure 3.6: Monthly averages of global solar irradiance in South Tyrol at stations installed after 2009. The shaded area represents the standard deviation of the original 10 minute data.
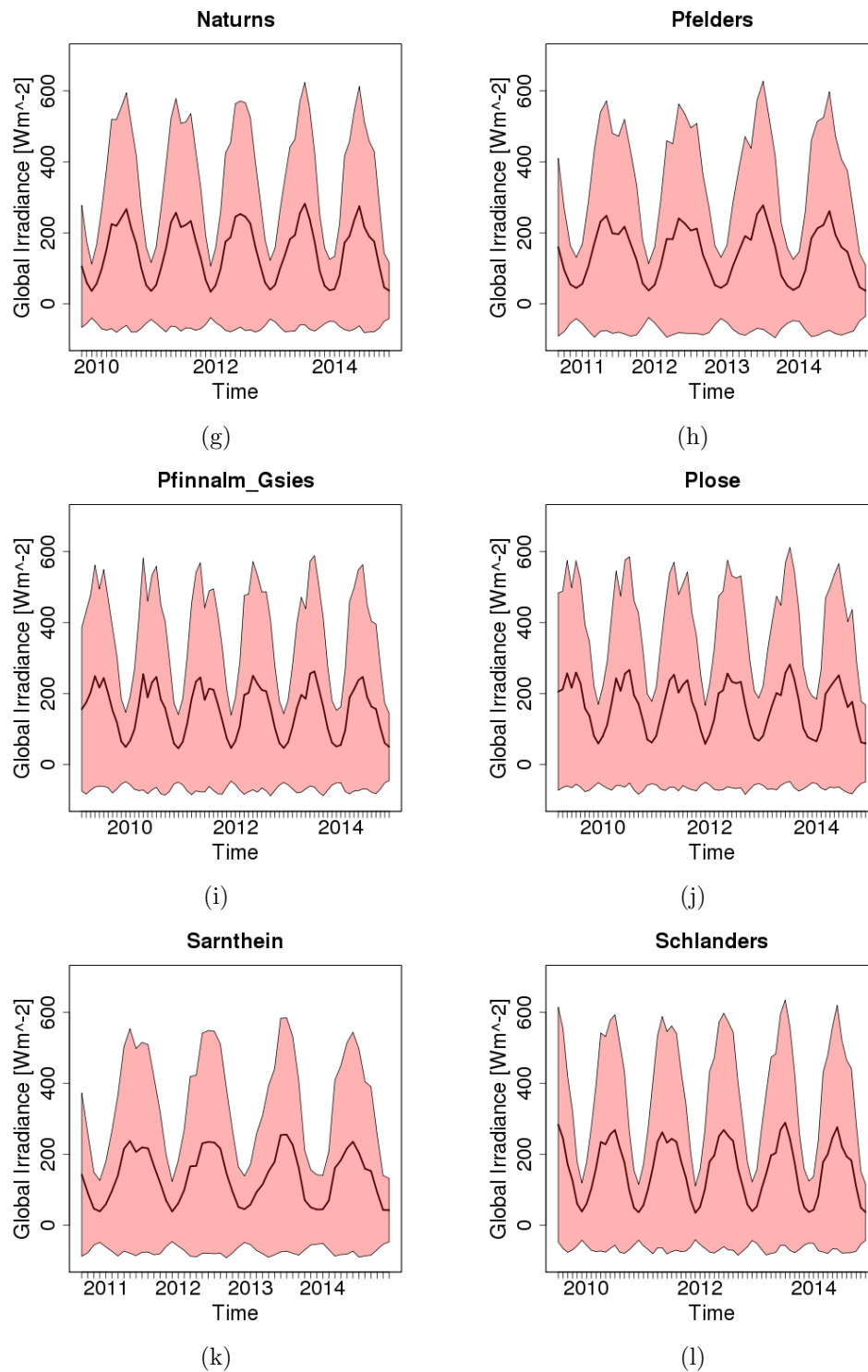
Figure 3.6: Monthly averages of global solar irradiance in South Tyrol at stations installed after 2009. The shaded area represents the standard deviation of the original 10 minute data.
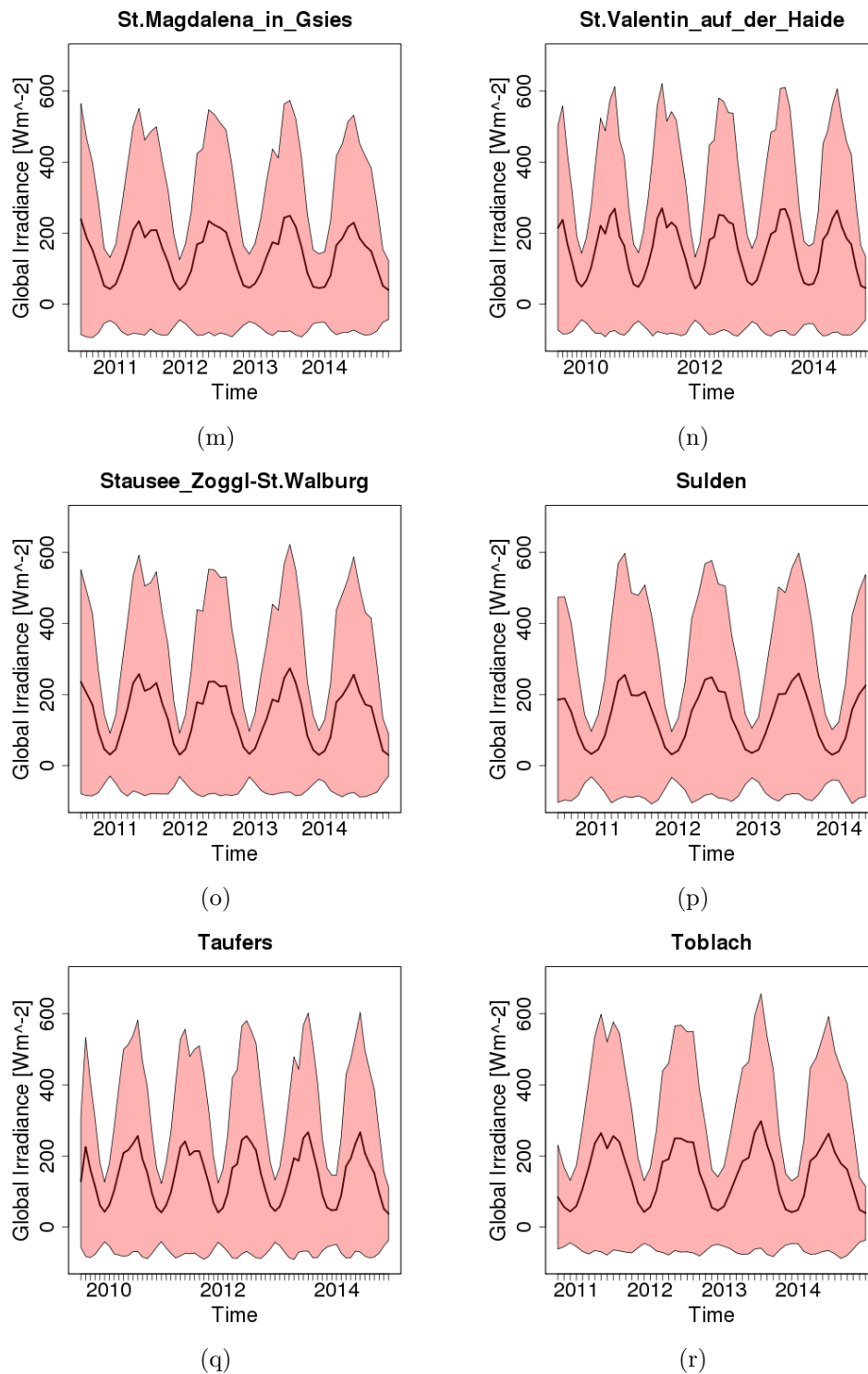
Figure 3.6: Monthly averages of global solar irradiance in South Tyrol at stations installed after 2009. The shaded area represents the standard deviation of the original 10 minute data.

Chapter 4

Estimation of diffuse radiation with decomposition models and artificial neural networks

4.1 Introduction

In this chapter we compare different kinds of decomposition models which estimate the fraction of diffuse radiation from measurements of global irradiance and other predictor parameters. These models can be used to obtain irradiance direct and diffuse components in regions, such as South Tyrol, whose networks of radiometers only measure global irradiance.

This analysis includes the following models:

1. The polynomial model of Reindl, modified by Helbig et al. (2009);

2. The Boland-Ridley-Laurent logistic model developed by Ridley et al. (2010);

3. A logistic model derived from data collected at three stations in the Alps;

4. A model based on artificial neural networks, developed here from alpine stations data.

The first one was chosen among other decomposition models because literature shows that it gives good results in the Eastern Alps (Helbig et al., 2010). The second and the third were selected because they allow to develop a generic logistic function, instead of a piecewise functions, they are easier to implement compared to other methods which exploit more predictors (Skartveit et al., 1998), and they also give better results in the area of interest (Lanini, 2010; Ridley et al., 2010). Finally, the fourth method has never been exploited for estimating irradiance components in the Alps.

4.2   Input data

This analysis is based on hourly averages of data collected at three measurement stations, located in the eastern Alps, where global irradiance and its components are measured. These stations include:

- The BSRN (Baseline Surface Radiation Network) station of Payerne (CH);

- The WRC (World Radiation Centre) station of Davos (CH);

- The EURAC station of Bolzano (IT).

Part of the data was excluded from the analysis, according to the following criteria:

1. Low solar elevation angle, ϕ, defined as follows:

$$\phi < 5° \tag{4.1}$$

   This condition is due to the cosine response of pyranometers.

2. Data which did not satisfy the following quality checks (Jacovides et al., 2006):

$$F < 5\,Wm^{-2} \tag{4.2}$$

$$\frac{F}{G_0} > 1.2 \tag{4.3}$$

$$\frac{F_{dif}}{F} > 1.1 \tag{4.4}$$

$$\frac{F_{dif}}{G_0} > 0.8 \tag{4.5}$$

where F is global irradiance, F_{dif} is diffuse irradiance, and G_0 is extraterrestrial irradiance on a horizontal plane.

Two parameters which are used in the decomposition models which are investigated here are the diffuse fraction, defined as follows:

$$k_d = \frac{F_{dif}}{F} \tag{4.6}$$

and the clearness index, defined as:

$$k_t = \frac{F}{G_0} \tag{4.7}$$

According to the suggestions of Reindl et al. (1990), two additional conditions were imposed:

$$
\begin{aligned}
k_d \geq 0.9 \qquad &for\ k_t < 0.2, \\
k_d \leq 0.8 \qquad &for\ k_t > 0.6.
\end{aligned}
\tag{4.8}
$$

4.3 The model of Reindl

Reindl et al. (1990) developed different decomposition models from data of five sites with at least one year of data for each site. They examined different predictor variables which can influence the fraction of diffuse irradiance, and found that k_t is the most important under cloudy and partially-cloudy sky conditions, while ϕ is the most relevant parameter under clear-sky conditions. Consequently, they developed three piecewise correlation models, all of which considered three intervals of clearness index, also including ambient temperature and relative humidity. Helbig (2009) combined two of these models, one of which only depends on k_t, and the other also depending on ϕ.

The correlation model is defined as follows:

$$
\begin{aligned}
for\ k_t \geq 0.78 \qquad & k_d = 0.147, \\
for\ 0 \leq k_t \leq 0.3 \qquad & k_d = 1.020 - 0.248\, k_t, \\
for\ 0.3 \leq k_t \leq 0.78 \qquad & k_d = 1.400 - 1.749\, k_t + 0.177\, sin(\pi/2 - \theta).
\end{aligned}
\tag{4.9}
$$

This piecewise correlation generates a discontinuous function, with fixed intervals of k_t.

4.3.1 Validation

The model of Reindl assumes that k_d is constant under clear-sky conditions, and that irradiance is totally diffuse under overcast conditions, and then linearly decreases with increasing k_t. This hypotheses are clearly too schematic and not exhaustive for the sites of interest, as evident from Figure 4.1. Under partially-cloudy conditions, the model assumes decreasing k_d with increasing k_t, depending on the sun elevation angle. Such a band pattern does not represent properly the spread of the data, and does not consider differences among geographic locations. This is due to the exploitation of only two predictors. At Bolzano and Payerne,

in fact, low values are overestimated and high values are underestimated, while at Davos there is a strong underestimation.

4.4 The model of Boland-Ridley-Laurent (BRL)

The BRL model, presented in Ridley et al. (2010), is a single function which includes more predictors than the Reindl model, but it does not require additional measurements. The added parameters, in fact, can be calculated from measurements of global irradiance and from astronomical calculations. Apparent solar time (AST) is included for representing eventual differences in the atmosphere between the morning and the afternoon. The daily clearness index, K_t, is used for describing eventual features typical of the single days:

$$K_t = \frac{\sum_{j=1}^{24} F_j}{\sum_{j=1}^{24} G_{0j}} \tag{4.10}$$

Finally, a variable called *persistence*, ψ, is included as a measure of the continuance of the global radiation level:

$$\psi = \begin{cases} \frac{k_{t-1}+k_{t+1}}{2} & sunrise < t < sunset \\ k_{t+1} & t = sunrise \\ k_{t-1} & t = sunset \end{cases}$$

The generic logistic model with five predictors has the following format:

$$k_d = \frac{1}{1 + e^{\beta_0 + \beta_1 k_t + \beta_2 AST + \beta_3 \phi + \beta_4 K_t + \beta_5 \psi}} \tag{4.11}$$

Ridley et al. (2010) estimated the parameters of the model from the data of seven locations worldwide by the minimum least squares method, giving the following expression for the BRL model:

$$k_d = \frac{1}{1 + e^{-5.38 + 6.63 k_t + 0.006 AST - 0.007 \phi + 1.75 K_t + 1.31 \psi}} \tag{4.12}$$
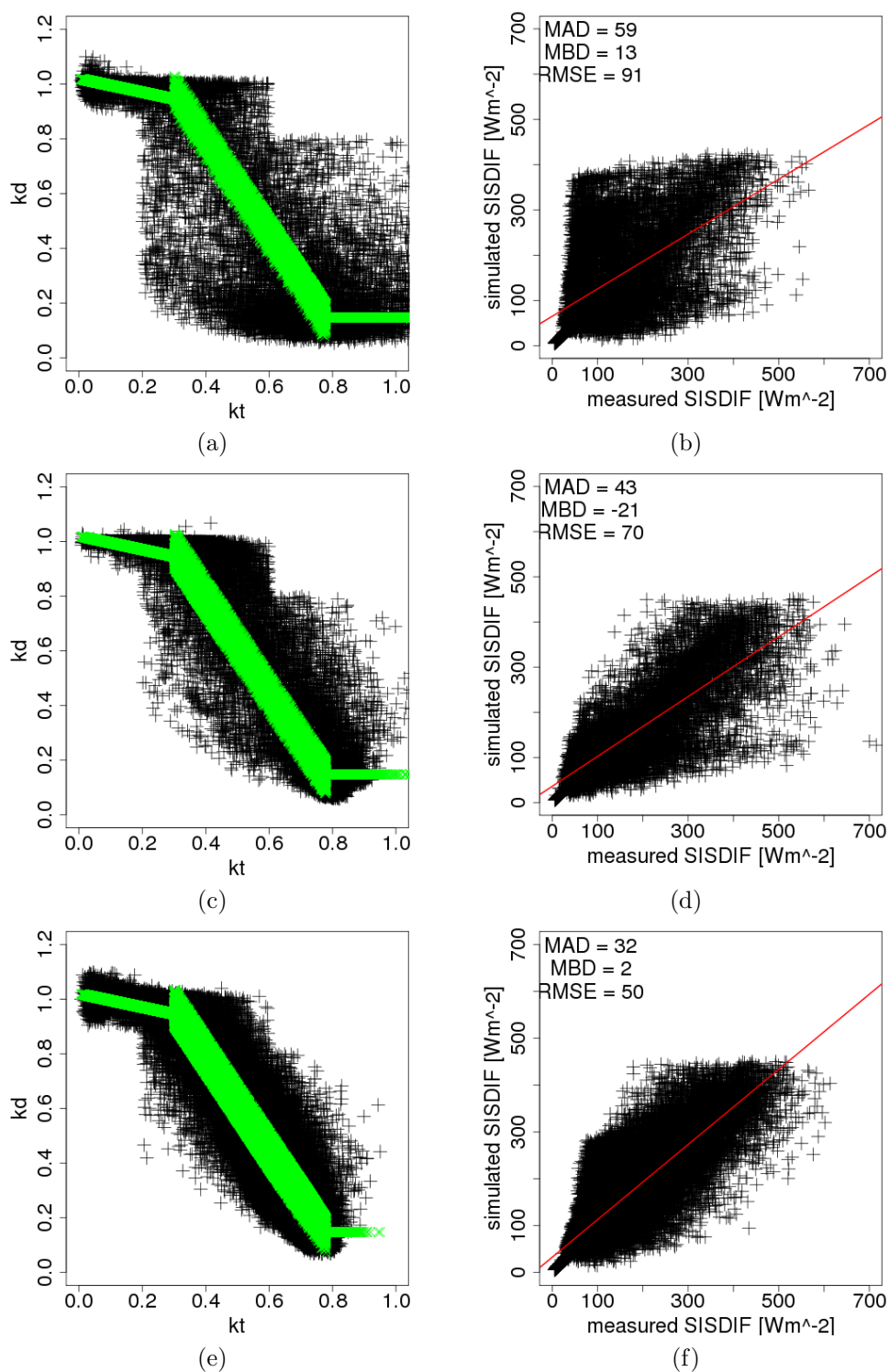
Figure 4.1: Performances of the model of Reindl-Helbig at Bolzano (a, b), Davos (c, d) and Payerne (e, f). The plots on the left hand side show k_d against k_t, while the plots on the right hand side show the scatterplot of modeled diffuse irradiance against measured diffuse irradiance and also include the statistical performances, in terms of MAB, MBD and RMSE, in Wm^{-2}.

4.4.1 Validation

Figure 4.2 shows k_d calculated by equation 4.12 against measured k_d. Even if this model seems to cover the spread of the data better than the model of Reindl, the error in the estimation of the hourly average of F_{dif} is major. This may be due to the fact that the locations used for deriving the model coefficients are too different from the alpine location of interest for this work. For this reason we decided to develop a new logistic model by using data from Bolzano, Davos and Payerne for estimating the parameters. This model is described in the next section.

4.5 The logistic model

We estimated the parameters β of Equation 4.11 by using hourly averages of global and diffuse irradiance measured at Bolzano from 2011 to 2014, at Davos from 2006 to 2010, and at Payerne from 2000 to 2010.

The logistic function can be expressed as:

$$Y(X, \ \beta) = \frac{e^{\beta \ mX}}{1 + e^{\beta \ mX}} \tag{4.13}$$

where Y represents the diffuse fraction, X the input parameters, and β the coefficients of the model.

The log-likelihood function was used as criterion to fit the logistic regression, and its negative was minimized by the Broyden-Fletcher-Goldfarb-Shanno (BFGS) itherative method, by using the BRL coefficients as initial set of parameters:

$$-\sum vY[\beta \ mX - log(1 + e^{\beta \ mX})] + (1 - vY)[-log(1 + e^{\beta \ mX})] \tag{4.14}$$

For the three sites of interest we obtained the coefficients indicated in Table 4.1
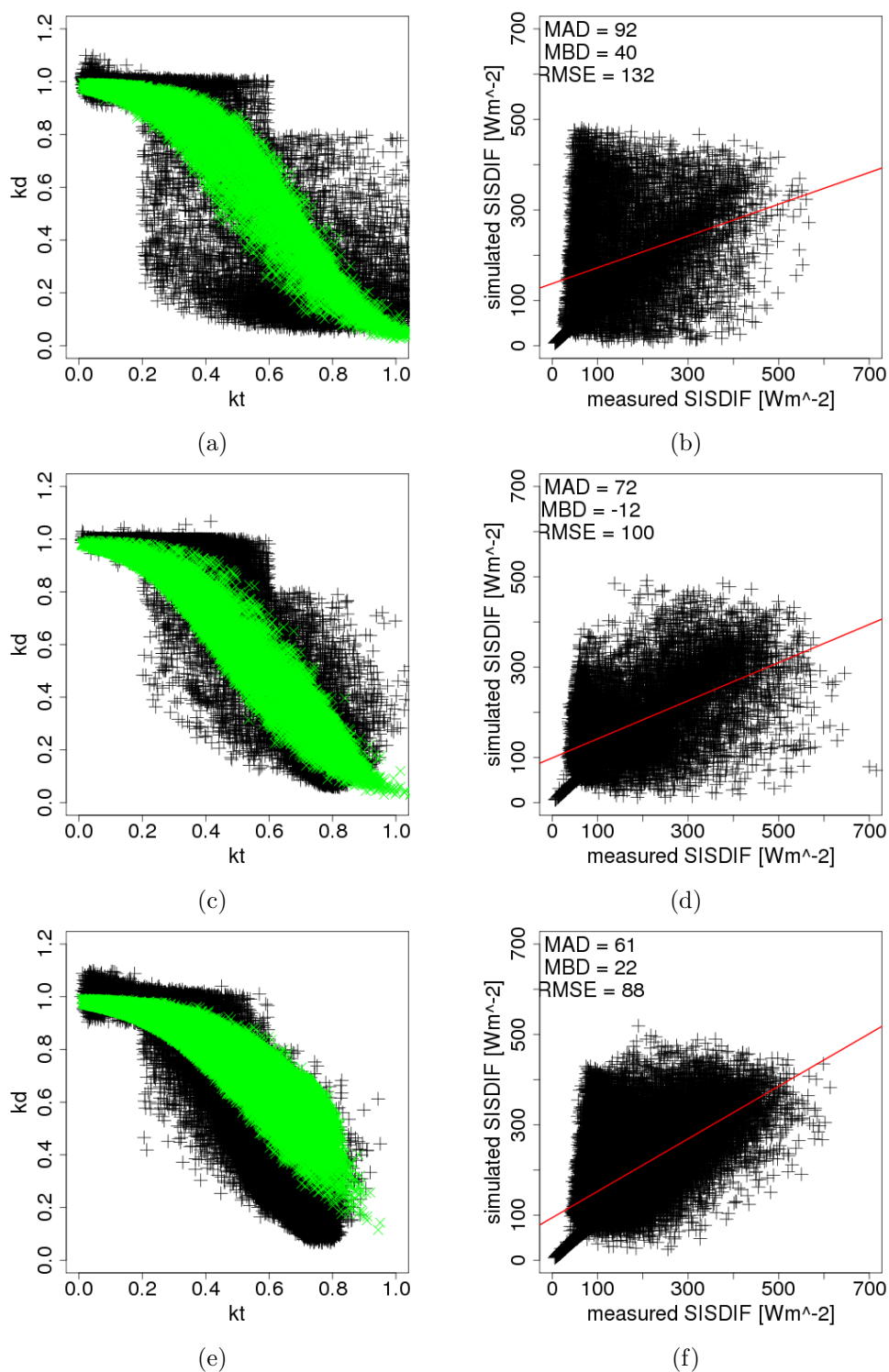
Figure 4.2: Performances of the model of Boland-Ridley-Laurent at Bolzano (a, b), Davos (c, d) and Payerne (e, f). The plots on the left hand side show k_d against k_t, while the plots on the right hand side show the scatterplot of modeled diffuse irradiance against measured diffuse irradiance and also include the statistical performances, in terms of MAB, MBD and RMSE, in Wm^{-2}.

Coefficients	Bolzano	Davos	Payerne
β_0	-1.1488	1.8027	3.1425
β_1	-6.9849	-5.9796	-6.5631
β_2	0.2571	0.0131	-0.0154
β_3	-0.0073	-0.0075	-0.0037
β_4	3.2585	3.3625	2.3691
β_5	1.1533	0.8778	-0.0864

Table 4.1: Parameter of the logistic function for Bolzano, Davos and Payerne.

4.5.1 Validation

The site-specific logistic models are able to estimate the fraction of diffuse irradiance with high accuracy, as indicated in Figure 4.3, with MAB of 29 Wm^{-2} at Bolzano, 41 Wm^{-2} at Davos, and 44 Wm^{-2} at Payerne, and a MBD of 0 Wm^{-2} at Bolzano, 2 Wm^{-2} at Davos and 22 Wm^{-2} at Payerne.

In order to derive a logistic model which is generally applicable at different locations in the Alps, we averaged the coefficients of Table 4.3 and obtained the following expression:

$$k_d = \frac{1}{1 + e^{1.2655 - 6.5092k_t + 0.0849AST - 0.0062\phi + 2.9967K_t + 0.6482\psi}} \qquad (4.15)$$

The application of this model gave the results shown in Figure 4.4, which are slightly better than the ones obtained with the site-specific coefficients, with MAB of 38 Wm^{-2} at Bolzano, 35 Wm^{-2} at Davos, and 26 Wm^{-2} at Payerne, and MBD of -4 Wm^{-2} at Bolzano, -16 Wm^{-2} at Davos, and 1 Wm^{-2} at Payerne.

4.6 Artificial Neural Networks (ANN)

In this section we develop a multiple-layer neural network algorithm to estimate hourly surface incoming diffuse radiation. Other authors have tested ANN for
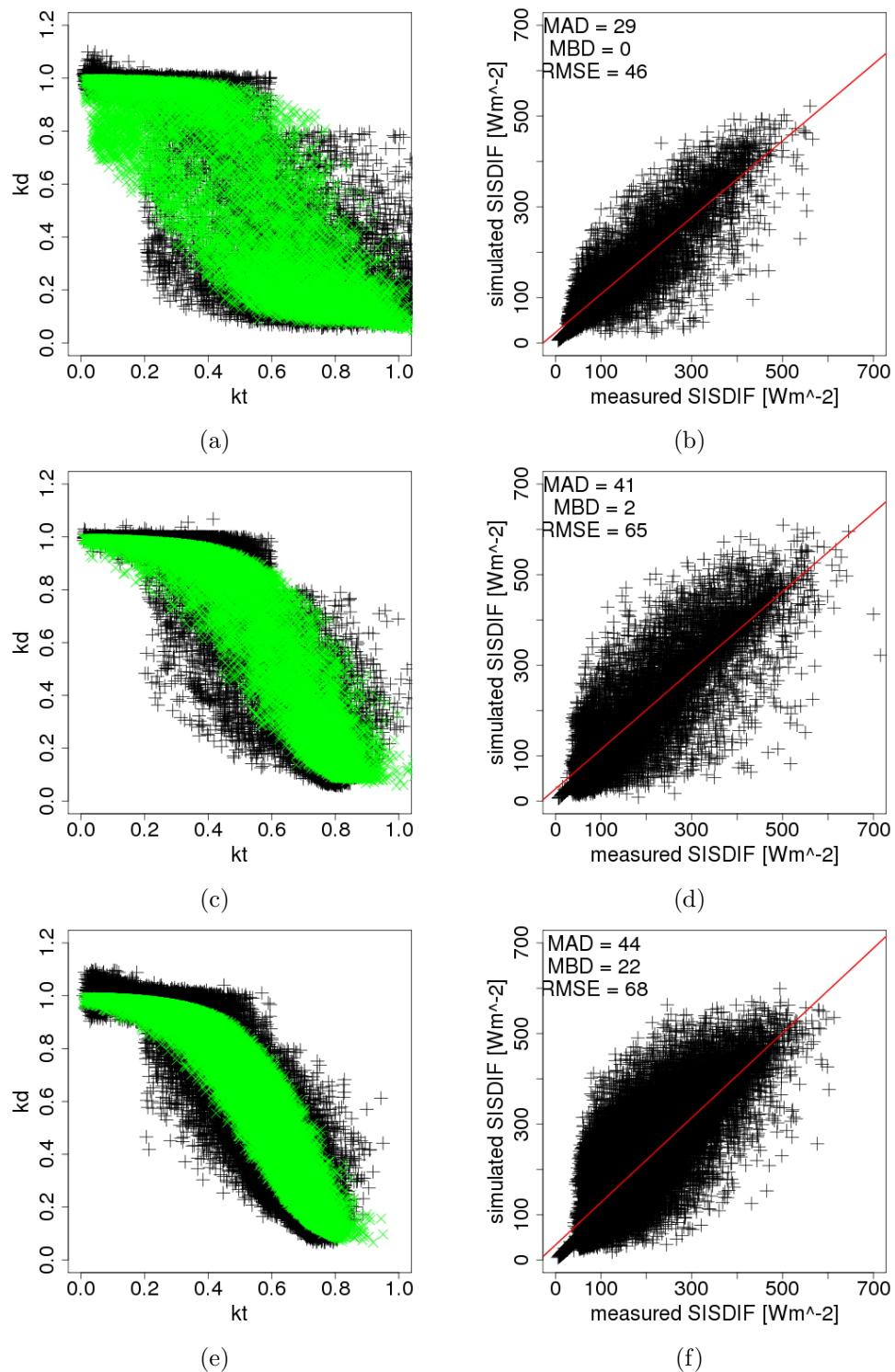
Figure 4.3: Performances of the logistic model with coefficients tuned for Bolzano (a, b), Davos (c, d) and Payerne (e, f). The plots on the left hand side show k_d against k_t, while the plots on the right hand side show the scatterplot of modeled diffuse irradiance against measured diffuse irradiance and also include the statistical performances, in terms of MAB, MBD and RMSE, in Wm^{-2}.
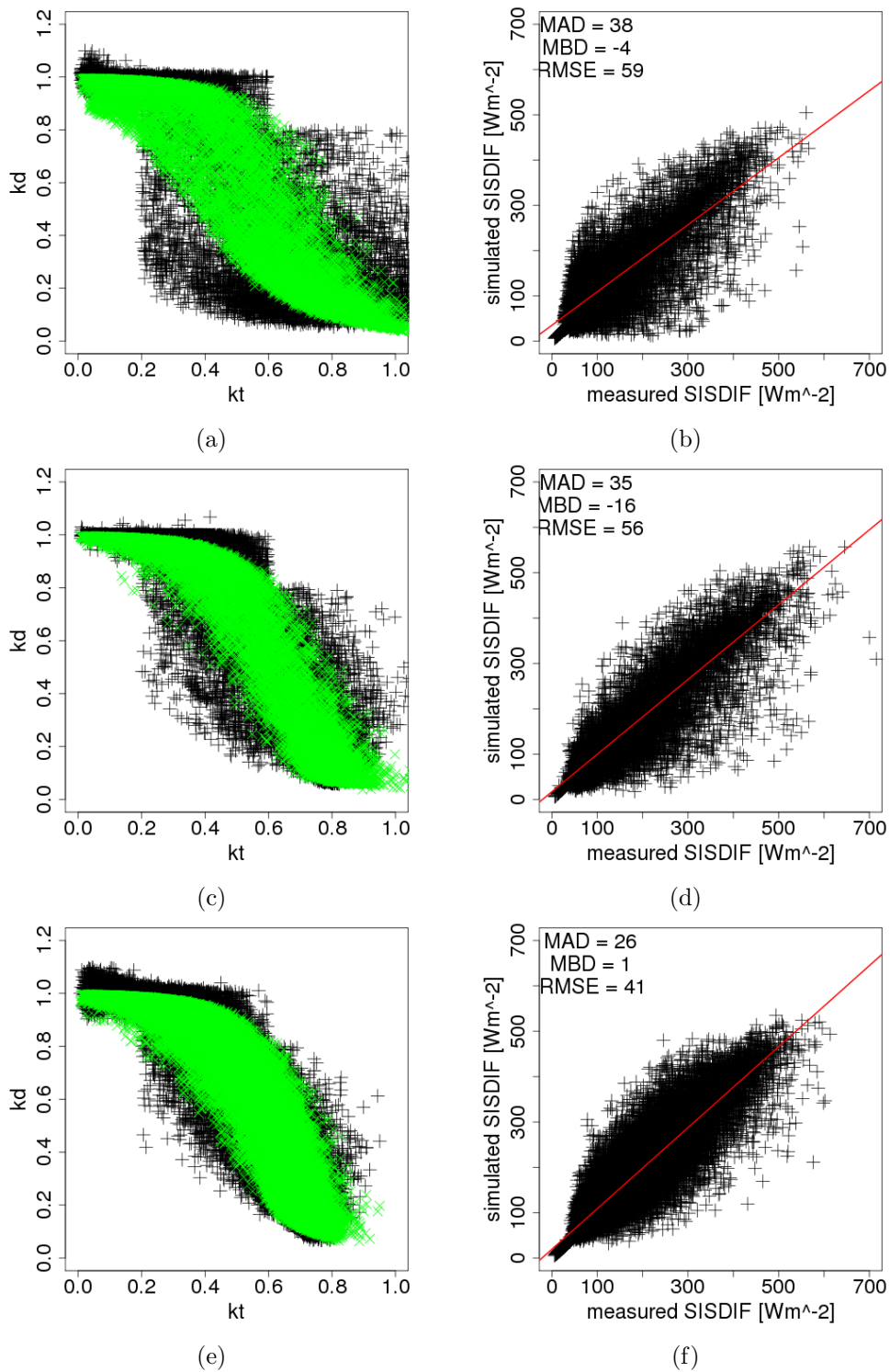
Figure 4.4: Performances of the logistic model with coefficients averaged over the ones tuned for Bolzano (a, b), Davos (c, d) and Payerne (e, f). The plots on the left hand side show k_d against k_t, while the plots on the right hand side show the scatterplot of modeled diffuse irradiance against measured diffuse irradiance and also include the statistical performances, in terms of MAB, MBD and RMSE, in Wm^{-2}.

estimating diffuse irradiance (Soares et al., 2004; Elminir et al., 2007; Kassem et al., 2009; Kaushika et al., 2014), but no attempt has been made specifically focused on the Alps. This class of algorithms is commonly referred to as *multilayer perceptron*, even if it is not composed of perceptrons, but of *sigmoid neurons*. Perceptrons, in fact, are neurons connected by weights, which take several inputs and produce a single output which is 0 if the weighted sum of the inputs is below threshold value, and 1 if it is above the threshold. Sigmoid neurons are similar to perceptrons, but their output is modified by an *activation function*, so that it is not just 0 or 1, but $f(wx + b)$, where b is called *bias*:

$$b = -threshold \tag{4.16}$$

This characteristic is crucial because it allows the network to *learn* changing the weights and the bias in order to improve the results.

Such a network of neurons connected by weights allows a nonlinear mapping between an an input and an output vector. The network of nodes generates an output signal, which is modified by a nonlinear activation function. The superposition of many simple nonlinear activation functions allows to approximate complex nonlinear functions. The activation function used here is called *sigmoid function*, and is defined by:

$$\sigma(z) = \frac{1}{1 + e^{-z}} \tag{4.17}$$

where:

$$z = \sum_j w_j x_j - b \tag{4.18}$$

where x_j are the inputs, w_j are the weights, and b is the bias.

The smoothness of the function σ is crucial, more than its mathematical expression, because it allows small changes in weights and bias to produce small changes in the output.

A *feed-forward* network was used in the work presented here, in which the output from one layer is used as input for the next layer, without loops. The *gradient descent with momentum* back-propagation algorithm was adopted for training the weights of the network.

4.6.1   Method

Two different experiment were performed. The first one only uses data from the station of Payerne, because it offers measurements of a wide set of meteorological parameters. The input features include: global irradiance (F), sun azimuth (α) and zenith (θ) angle, longwave irradiance (LW), aerosol optical thickness (AOT), atmospheric pressure (P), and relative humidity (RH). F, θ, α and AOT were chosen according to well-known physical relationship with the output variable, LW was included as it is closely related to cloud cover, which is a main driver of diffuse radiation, and finally meteorological parameters (T, P, RH) were considered as predictors of the sky conditions.

A feature selection based on the connection weights (Olden et al., 2004) has also been applied for verifying the importance of the predictors.

The second experiment also exploits data from Bolzano and Davos, and is based on different input features, i.e. the same ones used to develop the logistic model in the previous section.

Experiment 1

The following combinations of input variables have been considered:

Model	Input Parameters
1	F, α, θ, LW
2	F, α, θ, LW, AOD
3	F, α, θ, LW, AOD, P, RH
4	F, α, θ, T, P, RH

Table 4.2: Combinations of input parameters used for training the network.

For each combination of input variables, various network architectures were tested in order to find the optimal one, i.e. the one which produces the smallest error and the biggest correlation coefficient between estimated and measured diffuse irradiance.

Results were compared according to mean absolute bias (MAB) and mean bias deviation (MBD), calculated as in Castelli et al. (2014).

Model	Neurons in Hidden Layers	R	MAB [Wm^{-2}]	MBD [Wm^{-2}]
1	50 30	0.860	41	-6
1	40 30 20 10	0.842	45	-9
2	80 40 20	0.880	38	-8
2	100 40 20	0.875	40	-6
2	90 40 20	0.907	33	-7
3	90 40 20	0.870	38	-7
3	60 30 20	0.860	40	-10
4	90 40 20	0.810	50	-6

Table 4.3: Correlation coefficient, MAB and MBD for the network structures which gave the best results.

The performances of all the developed models are summarized in Table 4.3, where the best results are included for each model. MAB ranges between 33 and

50 Wm^{-2}, and MBD ranges between -6 and -10 Wm^{-2}. The worst model, in terms of MAB and MBD, is the number 4, which does not include longwave radiation nor AOD.

The observed results are of the same order of magnitude as the ones of the decomposition methods tested in previous sections. However the models developed here have been tested only on a validation dataset extracted from ground-based data which were used for training the network. More validation is required at different sites for testing the exploitation of these models at alpine locations where diffuse irradiance is not measured. The main limitation is the scarcity of high quality data in the region of interest, and the small number of parameters measured by common meteorological stations. One option which will be tested in future is using satellite-based and reanalysis data instead of measured data.

In the following section, another ANN model is developed, exploiting input features which are generally easy to obtain.

Experiment 2

The input variables which are considered in this experiment are: k_t, AST, ϕ, K_t and ψ, as for the logistic model. All the data available at the stations of Bolzano, Davos and Payerne have been aggregated for training the network.

Table 4.4 summarizes the results obtained with different network architectures.

Neurons in Hidden Layers	R	MAB	MBD
90 40 20	0.882 (0.951)	32 (0.077)	-17 (-0.044)
120 60 20	0.880 (0.952)	32 (0.076)	-19 (-0.048)
80 60 40 20	0.878 (0.950)	34 (0.081)	-23 (-0.056)
60 50 40 30	0.826 (0.911)	37 (0.096)	-10 (-0.035)
80 40	0.872 (0.953)	34 (0.080)	-25 (-0.054)

Table 4.4: Correlation coefficient, MAB and MBD, in terms of diffuse irradiance, for the network structures which gave the best results. The results in terms of diffuse fraction are indicated in brackets.

4.7 Validation of logistic and ANN models

The logistic function and the ANN model, developed from the data of Bolzano, Davos and Payerne, have been validated at the station of Weissfluhjoch (CH), at 2540 m.a.s.l.. This procedure allowed to check if these models are enough general to be exploited at different locations in the Alps. Results are summarized in Table 4.5, where MAB and MBD of ANN are the averages with standard deviation of the values obtained for the network architectures included in Table (4.4).

Results are comparable for the two models, but ANN performs slightly better. Both models estimate diffuse irradiance with acceptable accuracy at the considered location, even if its altitude is much different than the one of the stations used for tuning the functions.

Model	MAB [Wm^{-2}]	MBD [Wm^{-2}]
logistic	51	-17
ANN	43 ± 1	-10 ± 3

Table 4.5: Validation of the logistic function and of the ANN model at Weissfluhjoch.

4.8 Conclusions

In this chapter first we tested two existent decomposition models (the Reindl-Helbig and the BRL) at three alpine stations. Since these models did not give satisfactory results, we developed a site-specific logistic function and an ANN model specifically for the sites of interest.

Results show that the logistic function with coefficients derived from alpine stations data is the best solution for estimating irradiance components where global radiation is measured. ANN give similar results, with errors close to the ones of the logistic model, but the absence of an objective criterion for choosing the
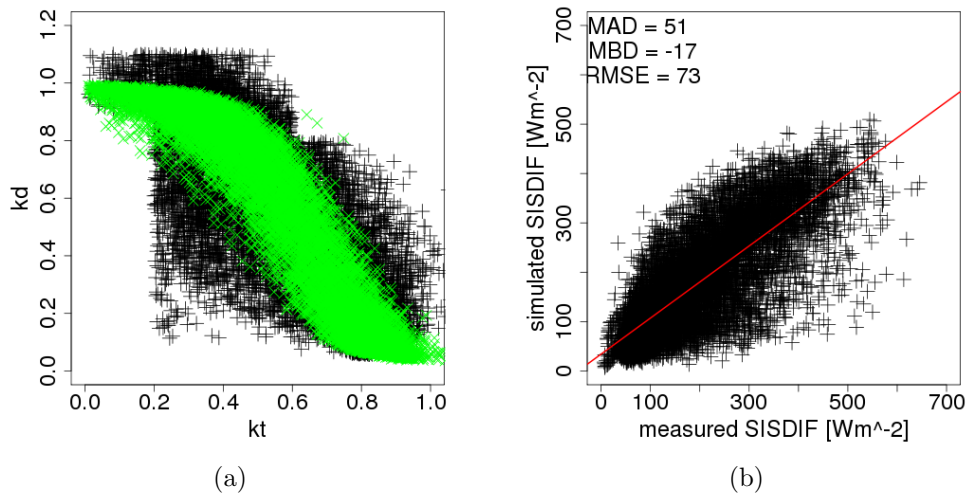
Figure 4.5: Performances of the logistic model, with coefficients derived from Bolzano, Davos and Payerne, at Weissfluhjoch. The plot on the left hand side shows k_d against k_t, while the plot on the right hand side shows the scatterplot of modeled diffuse irradiance against measured diffuse irradiance and also include the statistical performances, in terms of MAB, MBD and RMSE, in Wm^{-2}.

best architecture, and the required training time do not encourage their usage for decomposing irradiance. Nevertheless ANN based models can reach high accuracy and generality, as evidenced by their validation at the high altitude alpine site of Weissfluhjoch, and in the future it would be worth devoting more time for refining the models implemented here.

Chapter 5

Atmospheric radiative transfer

5.1 The equation of radiative transfer

In Chapter 2 we described qualitatively the processes of solar radiation absorption and scattering taking place in the atmosphere. Here we can formalize them by introducing the equation of radiative transfer (Liou, 2002). When traversing a medium of thickness ds, the intensity of a beam of radiation I_λ undergoes weakening due to extinction and strengthening due to emission from the traversed material and multiple scattering from the other directions. The difference between the intensity of the emerging and incoming radiation can be expressed as:

$$dI_\lambda = -k_\lambda \rho I_\lambda ds + j_\lambda \rho ds \tag{5.1}$$

where ρ is the density of the medium, k_λ is the mass extinction cross section for radiation of wavelength λ, and j_λ is a source function coefficient. If we define a source function $J_\lambda = j_\lambda / k_\lambda$, Equation 5.1 becomes:

$$\frac{dI_\lambda}{k_\lambda \rho ds} = -I_\lambda + J_\lambda \tag{5.2}$$

which is the general equation of radiative transfer.

In the wavelength region between 0.2 and 5 μm, emissions from the Earth and the atmosphere can be neglected. Supposing that multiple scattering can also be neglected, Equation 5.2 becomes:

$$\frac{dI_\lambda}{k_\lambda \rho ds} = -I_\lambda \tag{5.3}$$

For a finite thickness s_1 of the medium traversed by radiation, Equation 5.3 can be integrated, giving the emerging intensity:

$$I_\lambda(s_1) = I_\lambda(0)exp\left(-\int_0^{s_1} k_\lambda \rho ds\right) \tag{5.4}$$

If the medium is homogeneous, k_λ is constant with s, and from Equation 5.4 we obtain the Beer-Bouguer-Lambert law, which describes the decrease in intensity of a beam of radiation traversing an homogeneous absorbing and scattering medium:

$$I_\lambda(s_1) = I_\lambda(0)e^{-k_\lambda \int_0^{s_1} \rho ds} \tag{5.5}$$

For many applications concerning radiative transfer in the Earth's atmosphere, the atmosphere is considered plane-parallel, i.e. atmospheric properties vary only in the vertical direction. In this case it is convenient to substitute the general linear distance s with the distance along the vertical direction, z, thus equation 5.2 becomes:

$$cos\theta \frac{dI_\lambda(z; \theta, \phi)}{k_\lambda \rho dz} = -I_\lambda(z; \theta, \phi) + J_\lambda(z; \theta, \phi) \tag{5.6}$$

where θ and ϕ are the zenith and azimuth angles, as defined in Figure 2.2.

Let τ be the normal optical thickness:

$$\tau_\lambda = \int_z^\infty k_\lambda \rho dz' \tag{5.7}$$

measured downward. Introducing it in Equation 5.4 we get:

$$\mu \frac{dI_\lambda(\tau; \mu, \phi)}{d\tau} = I_\lambda(\tau; \mu, \phi) - J_\lambda(\tau; \mu, \phi) \tag{5.8}$$

where $\mu = cos\theta$. This is the equation of radiative transfer in the approximation of plane-parallel atmosphere. By integrating it along τ, we can get the intensity of the upward and downward radiation at level τ. In particular, the downward ($\mu < 0$) radiation at surface, where $\tau = \tau*$, is:

$$I_\lambda(\tau_\lambda^*; -\mu, \phi) = I_\lambda(0; -\mu, \phi)e^{-\tau_\lambda^*/\mu} + \int_0^{\tau_\lambda^*} J_\lambda(\tau_\lambda; -\mu, \phi)e^{-(\tau_\lambda^* - \tau_\lambda)/\mu}\frac{d\tau_\lambda}{\mu} \tag{5.9}$$

and the upward radiation ($\mu > 0$) at the top of the atmosphere, where $\tau = 0$, is:

$$I_\lambda(0; \mu, \phi) = I_\lambda(\tau_\lambda^*; \mu, \phi)e^{-\tau_\lambda^*/\mu} + \int_0^{\tau_\lambda^*} J_\lambda(\tau_\lambda; \mu, \phi)e^{-\tau_\lambda/\mu}\frac{d\tau_\lambda}{\mu} \tag{5.10}$$

The source term J in Equation 5.8 can be decomposed in three contributions, J_1, J_2 and J_3, which represent respectively the following processes:

1. emission;

2. single scattering of the unscattered solar flux;

3. multiple scattering.

The component due to emission can be expressed by the Plank's law:

$$J_1 = B(T) \tag{5.11}$$

where B is the monochromatic radiance emitted by a black body at temperature T, expressed by:

$$B_\lambda(T) = \frac{2hc}{\lambda^5[e^{(ch/K\lambda T)} - 1]} \tag{5.12}$$

where $h = 6.626 \times 10^{-34}$ J is the Plank constant and $K = 1.3806 \times 10^{-23}$ J deg^{-1} is the Boltzmann constant.

The term of single scattering of the direct solar beam from the direction $(-\mu_0, \phi)$ to the direction (μ, ϕ) is expressed, based on the Beer-Bouguer-Lambert law and on the definition of the phase function, as:

$$J_2 = Fe^{-\tau/\mu_0} \frac{P(\mu, \phi; -\mu_0, \phi_0)}{4\pi} \tag{5.13}$$

where F is the incoming irradiance at the top of the atmosphere.

The multiple scattering contribution from directions (μ', ϕ') to (μ, ϕ) is expressed as:

$$J_3 = \int_0^{2\pi} \int_{-1}^{1} I(\tau; \mu', \phi') \frac{P(\mu, \phi; \mu', \phi')}{4\pi} d\mu' d\phi' \tag{5.14}$$

Weighting all the contributions with the scattering and absorption coefficient, the source term can be expressed as:

$$J(\tau; \mu\phi) = \beta_{sca} Fe^{-\tau/\mu_0} \frac{P(\mu, \phi; -\mu_0, \phi_0)}{4\pi}$$
$$+ \beta_{sca} \int_0^{2\pi} \int_{-1}^{1} I(\tau; \mu', \phi') \frac{P(\mu, \phi; \mu', \phi')}{4\pi} d\mu' d\phi' + \beta_{abs} B[T(\tau)] \tag{5.15}$$

We can define the *single scattering albedo* ω as the ratio of the scattering coefficient to the extinction coefficient:

$$\omega = \frac{\beta_{sca}}{\beta_{ext}} \tag{5.16}$$

or, in terms of the absorption coefficient:

$$1 - \omega = \frac{\beta_{abs}}{\beta_{ext}} \tag{5.17}$$

Introducing the definition of ω in Equation 5.15, equation 5.8 becomes:

$$\mu \frac{dI_\lambda(\tau; \mu, \phi)}{d\tau} = I_\lambda(\tau; \mu, \phi) - \frac{\omega}{4\pi} F e^{-\tau/\mu_0} P(\mu, \phi; -\mu_0, \phi_0)$$
$$+ \frac{\omega}{4\pi} \int_0^{2\pi} \int_{-1}^1 I(\tau; \mu', \phi') P(\mu, \phi; \mu', \phi') d\mu' d\phi' + (1 - \omega) B[T(\tau)] \quad (5.18)$$

5.2   The radiative transfer model libRadtran

An analytic solution of the equation of radiative transfer can be calculated only for few special cases. In all the other situations radiative transfer models are used to solve numerically the equation for given atmospheric and surface properties. In this work we use the software libRadtran (Mayer and Kylling, 2005) which is a collection of programs for modeling solar and thermal radiation in the Earth's atmosphere. Its core is the radiative transfer model *uvspec* which includes three parts:

1. an atmospheric module for converting atmospheric information, such as trace gases and aerosol profiles, precipitable water, ozone column amount, surface pressure, temperature profile, into optical properties;

2. the radiative transfer equation solver, which exploits the discrete-ordinate method for calculating radiances, irradiances and actinic fluxes for given optical properties;

3. a post-processing unit which elaborates model output according to the user's needs.

uvspec includes different solvers for the equation of radiative transfer, giving the user the possibility to use the most suitable one for any specific application. Some of these solvers work in the plane-parallel approximation, some other in the pseudo-spherical. The latter treats direct solar radiation in spherical geometry and

multiple scattering in the plane-parallel approximation, thus giving better results for low sun elevations.

Four different ways may be chosen for defining the spectral resolution:

1. spectrally resolved calculation are applicable in the ultraviolet part of the visible spectrum, where gas absorption generally occurs in broad bands. Extraterrestrial irradiance, highly variable with wavelength, is considered at high resolution and interpolated to the moderate resolution which is used to calculate atmospheric transmission (0.5 nm below 350 nm and 1 nm above 350 nm). Finally the two spectra are multiplied;

2. line-by-line calculation is the most accurate and time-consuming modality. It can be used to handle the narrow lines of molecular absorption spectra in the infrared region;

3. the correlated-k method is based on grouping gaseous absorption coefficients (k). Since these coefficients assume the same value many times over a spectral interval, the calculations are performed only once for a given value of k thus reducing the computing time. The wavelength grid is based on the band parameterization and the output is integrated over each band;

4. pseudo-spectral method has been incorporated from the radiative transfer model SBDART (Ricchiazzi et al., 1998). It allows radiation calculation at any wavelength, but the gas absorption is provided at a a limited resolution.

The atmosphere is described and incorporated into libRadtran through its main constituents: water, aerosol, ice clouds, Rayleigh scattering and absorption by molecules. The model is very flexible because it allows the user to specify as much information as available and using standard values for the unknown atmospheric properties. The user can provide profiles of micro-physical or optical properties. In addition it is also possible to specify columnar properties which are used to scale standard profiles.

Surface reflectance can be set to a constant value, or a wavelength dependent albedo function can be specified.

libRadtran includes different solar spectra among which the user can choose the most suitable one in terms of accuracy and resolution.

5.3 Applications: modeling the radiative forcing of measured aerosol profiles

The next chapter, which is derived from Ferrero et al. (2014), of which the PhD candidate is co-author, reports an example of use of radiative transfer modeling for evaluating the radiative forcing and heating rate of measured vertical aerosol profiles. These profiles were collected at three sites in Italy and included the following measurements:

- Black carbon (BC) mass concentration and absorption coefficient profiles;

- Aerosol number-size distribution profiles;

- $PM_{2.5}$ samples for performing the analysis of aerosol chemical composition;

- Meteorological parameters (pressure, temperature and relative humidity) profiles.

Aerosol extinction coefficient, single scattering albedo and phase function were calculated by a Mie code along vertical profiles. These data were used to generate input files for libRadtran, one for each atmospheric layer, including the optical properties at different wavelengths.

All the details about measurements and modeling are included in the following chapter.

Chapter 6

Radiative forcing and heating rate of measured vertical profiles of black carbon aerosol

6.1   Abstract

A systematic study of black carbon (BC) vertical profiles measured at high-resolution over three Italian basin valleys (Terni Valley, Po Valley and Passiria Valley) is presented. BC vertical profiles are scarcely available in literature[1]. The campaign lasted 45 days and resulted in 120 measured vertical profiles. Besides the BC mass concentration, measurements along the vertical profiles also included aerosol size distributions in the optical particle counter range, chemical analysis of filter samples and a full set of meteorological parameters. Using the collected experimental data, we performed calculations of aerosol optical properties along the vertical profiles. The results, validated with AERONET data, were used as inputs to a radiative transfer model (libRadtran). The latter allowed an estimation of vertical profiles of the aerosol direct radiative effect, the atmospheric absorption and the heating rate in the lower troposphere. The present measurements revealed

---

[1]This chapter is based on Ferrero et al. (2014)

some common behaviors over the studied basin valleys. Specifically, at the mixing height, marked concentration drops of both BC (range: from -48.4 $\pm$ 5.3 to -69.1 $\pm$ 5.5 %) and aerosols (range: from -23.9 $\pm$ 4.3 to -46.5 $\pm$ 7.3 %) were found. The measured percentage decrease of BC was higher than that of aerosols: therefore, the BC aerosol fraction decreased upwards. Correspondingly, both the absorption and scattering coefficients decreased strongly across the mixing layer (range: from -47.6 $\pm$ 2.5 to -71.3 $\pm$ 3.0 % and from -23.5 $\pm$ 0.8 to -61.2 $\pm$ 3.1 %, respectively) resulting in a single-scattering albedo increase along height (range: from +4.9 $\pm$ 2.2 to +7.4 $\pm$ 1.0 %). This behavior influenced the vertical distribution of the aerosol direct radiative effect and of the heating rate. In this respect, the highest atmospheric absorption of radiation was predicted below the mixing height (2-3 times larger than above it) resulting in a heating rate characterized by a vertical negative gradient (range: from -2.6 $\pm$ 0.2 to -8.3 $\pm$ 1.2 K day-1 km^{-1}). In conclusion, the present results suggest that the BC below the mixing height has the potential to promote a negative feedback on the atmospheric stability over basin valleys, weakening the ground-based thermal inversions and increasing the dispersal conditions.

6.2   Introduction

Atmospheric aerosols can influence the Earth's climate through direct effects (sunlight absorption and scattering), indirect effects (i.e. modifying the lifetime of the clouds) and semi-direct effects (i.e. affecting the atmospheric thermal structure) (Ramanathan and Feng, 2009; Koren et al., 2008; Stocker et al., 2013; Koren et al., 2004; Kaufman et al., 2002). The instantaneous direct radiative effect (DRE) due to the aerosol load amount to $\sim$ -10 to 20 Wm^{-2} at the Top of Atmosphere (TOA) and can reach $\sim$ -50 W m-2 at the surface (Perrone and Bergamo, 2011). Among the various aerosol constituents, black carbon (BC) is the second most important anthropogenic climate-forcing agent (Ramanathan and Carmichael, 2008; Bond

et al., 2013). The averaged BC-DRE at the TOA ranges between $+0.08$ Wm^{-2} and $+1.4$ Wm^{-2} (Samset et al., 2013; Ramanathan and Carmichael, 2008; Stocker et al., 2013; Jacobson, 2001) with a best estimate of $+0.71$ Wm^{-2} (Bond et al., 2013). Moreover, the sign and magnitude of the BC radiative forcing are also highly uncertain and therefore BC may affect the climate by both warming the atmosphere (in average $+2.6$ Wm^{-2} and in some cases up to $+75$ Wm^{-2}) or cooling ("masking") the surface (in average -1.7 Wm^{-2} and in some cases down to -60 Wm^{-2}) (Chakrabarty et al., 2012; Ramanathan and Carmichael, 2008). The wide range of BC-DRE values, reported in literature, is due to different reasons: the complexity of aerosol chemistry (i.e. mixing state) (Ramana et al., 2010), the surface albedo (Seinfeld and Pandis, 2012) and, most important, the spatial heterogeneity of BC concentration (horizontal and vertical) due to its relatively short lifetime (weeks) when compared with CO2 (Samset et al., 2013; Cape et al., 2012). In particular, recent modeling studies (Samset et al., 2013; Zarzycki and Bond, 2010) evidenced a clear correlation of DRE with the BC abundance along the vertical profile. The resulting overall degree of uncertainty attributable to the assumptions about the vertical distribution of BC was estimated to be in the range 20-50%. Indeed, the vertical heterogeneity of BC, and therefore of its DRE, may influence the thermal structure of the atmosphere. In particular, heating rates may vary as a function of height in a range from 0.5 to 2 K day^{-1} (Chakrabarty et al., 2012; Ramana et al., 2010; Tripathi et al., 2007); as a result different kinds of feedbacks can take place, such as those on clouds dynamics (Bond et al., 2013), on regional circulation systems (i.e. monsoons) and on the planetary boundary layer (PBL) dynamics (Ramanathan and Feng, 2009; Ramanathan and Carmichael, 2008). Interestingly, most of the BC sources and emissions are at ground while most of the uncertainty on the BC-DRE comes from the region above 5km. It is clear that the BC evolution in the first hundred meters above the planet surface, especially across the mixing layer, is going to strongly affect the BC concentration in the upward

atmospheric layers. In this respect, measurements in the planetary boundary layer are important and can be conducted by tethered balloons and unmanned aerial vehicles (Ferrero et al., 2012; Corrigan et al., 2008; Maletto et al., 2003). Since it is likely that different regions will have a different sensitivity to all of these processes (Bond et al., 2013) and also that modeling of and observational constraints on the BC vertical distribution are particularly poor, there is the need to measure the BC vertical distribution on a regional scale: from areas characterized by anthropogenic emissions and atmospheric stability conditions to areas characterized by long-range transport phenomena (Samset et al., 2013; Corrigan et al., 2008; Ramana et al., 2007). Recently, some measurements have been reported in the Asian region (Safai et al., 2012; Babu et al., 2011; Ramana et al., 2010; Tripathi et al., 2007) and over the ocean (Schwarz et al., 2010, 2013). To date, the only measured vertical profiles of BC and absorption coefficient in Italy are reported for a short campaign by Ferrero et al. (2011a). Anyway, BC vertical profiles are still scarce if compared with ground-level data, especially over Europe, where the experimental campaigns have been limited in time and/or in space (McMeeking et al., 2010; Schwarz et al., 2006). The complex morphological structure of the Italian landscape represents an interesting and significant case study for black carbon and aerosols monitoring. The Italian territory is characterized by a multitude of basin valleys surrounded by hills, where urban and industrial centers are usually settled. These valleys represent areas where low wind speeds and conditions of atmospheric stability are common, thus promoting the formation of strong vertical aerosol (and BC) gradients in the lower troposphere (Moroni et al., 2012, 2013; Ferrero et al., 2011a; Carbone et al., 2010; Rodríguez et al., 2007). In the present paper, we report a comparative study of BC and aerosol vertical profiles measured over three different Italian basin valleys (Po Valley, in Northern Italy; Terni Valley in the Central Apennines; and Passiria-Val Venosta Valleys in the Alps). An extensive field campaign allowed collecting data for 120 vertical profiles

in less than 45 days, providing an important piece of information on BC vertical profiles. Starting from the experimental data, DRE and heating rates profiles were calculated. Finally, a modeling of possible feedbacks induced by BC gradients in the lower troposphere has been performed. In the next sections we briefly describe the sampling sites (section 2.1) and the vertical profile measurements (section 2.2). BC and aerosol chemistry determination are illustrated in sections 2.2.1 and 2.2.2. The OPC size-distribution correction and the optical properties calculation using the Mie theory are described in section 2.3 and the radiative transfer in section 2.4. Results and discussion follow in section 3 with the conclusions in the final section 4.

6.3 Experimental

6.3.1 Sampling sites

Balloon soundings were carried out during winter 2010 over three basin Valleys in the following sites (Figure 6.1):

1. Terni (TR, 42°33'58"N, 12°38'56"E, 122 m ASL), located in the Terni Valley in Central Italy. The Terni Valley ($\sim$50 km^2) is surrounded by mountains on three sides (NNE, SE and SW) and hosts the medium-sized town of Terni, with the largest stainless-steel production site in Europe and various other industries. In wintertime, wind speed is low and the aerosol dispersion is limited with height. A full description of the site concerning the aerosol properties (chemistry, sources and vertical profiles) is reported in Moroni et al. (2012), Moroni et al. (2013) and Ferrero et al. (2012). Within the present work, vertical aerosol and BC profiles were measured over Terni from Jan 27th to Feb 4th for a total of 40 profiles.

2. Milan (MI, 45°31'19"N, 9°12'46"E, 136 m ASL), located in the Po Valley ($\sim$46000 km^2, Northern Italy) in the midst of an extensive conurbation that

is the most industrialized and heavily populated area in the Po Valley. In the Po Valley stagnant conditions often occur causing a marked seasonal variation of PM concentrations within the mixing layer. Balloon soundings were conducted at the Torre Sarca sampling site within the Milano-Bicocca University Campus (north of Milano, active from 2005 for aerosol characterization both at ground-level and along vertical profiles). A full description of the site and the related aerosol properties (vertical profiles, chemistry, sources, and toxicity) are reported in Ferrero et al. (2010), in Perrone et al. (2013) and in Sangiorgi et al. (2011). Within the framework of the 2010 winter campaign, vertical aerosol and BC profiles were measured over Milan from Feb 12th to Feb 25th for a total of 36 profiles.

3. Merano (ME, 46°38'52"N, 11°10'13"E, 272 m ASL), located at the intersection of two main alpine Valleys: Val Venosta (E-W orientation) and Val Passiria (N-S orientation), allowing the air masses to be transported both from Continental Europe (North) and from the Po Valley (South). The sampling site was located in a rural area close to the background station for air quality monitoring of the local authorities ("Merano 2 station", APPA). A full description of the site and pollution in the surrounding valleys are reported in Emili et al. (2010). Within the 2010 winter campaign, vertical aerosol and BC profiles were measured over Merano from March 3th to March 13th for a total of 40 profiles.

6.3.2 Vertical profile measurements

BC and aerosol profile measurements were carried out over TR, MI and ME by means of a helium-filled tethered balloon (diameter 4.5 m, volume 47.8 m^3, payload 40 kg, Figure 6.1b) equipped with an instrumental package consisting of: 1) a micro-Aethalometer microAeth®AE51 (Magee Scientific) to measure the BC concentrations and the absorption coefficient at 880 nm; 2) an optical particle counter
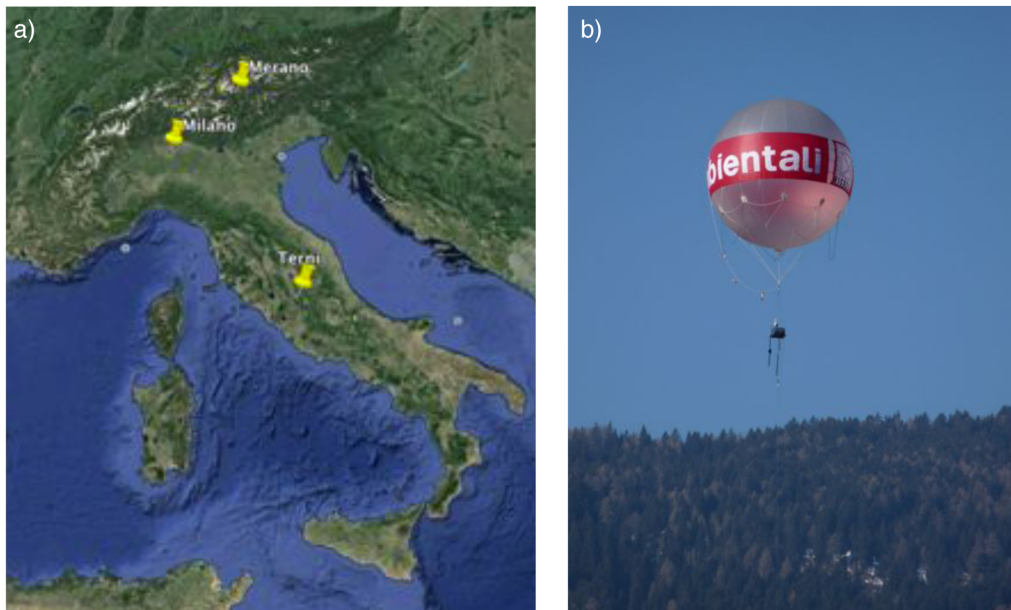
Figure 6.1: (a) Location of the three sampling sites: Terni in central Italy (Terni Valley), Milan in northern Italy (Po Valley) and Merano in the Alpine region (between Passiria and Val Venosta valleys); (b) the tethered balloon flying over Merano with the instrumentation package.

(OPC, 1.107 "Environcheck" Grimm, 31 class-sizes ranging from 0.25 μm to 32 μm) for the particle number size distribution determination; 3) a portable cascade impactor (Sioutas with Leland Legacy pump, SKC) to collect $PM_{2.5}$ samples at different heights (section 2.2.2); 4) a meteorological station (LSI-Lastem: pressure, temperature and relative humidity). An electric winch controlled the balloon ascent/descent rate which was set at 30.0 ± 0.1 m/min; a measurement time resolution of 6 sec was chosen for each instrument, giving 3.0 meters of measurement vertical resolution. The maximum height reached during each flight depended on atmospheric conditions and the location; for the majority of profiles, the maximum height was between 600 and 800 m AGL. Vertical aerosol profiles allowed the determination of the mixing height (MH) by means of a gradient method, as aerosols act as tracer of atmospheric plumes integrating the effects of turbulent forces (thermal and mechanical) along height; the gradient method's ability to infer the MH has yet been assessed in previous works (Ferrero et al., 2011a,b,

2010) and it will be used to calculate averaged aerosol and BC profiles for each site (section 3.2)

Aethalometer data: Black Carbon and the related absorption coefficient

BC and absorption coefficient profiles have been determined using the microAeth®-AE51 (250 g, 117×66×38 mm^3). The AE51 measures the light attenuation (ATN) at 880 nm induced by BC through a PTFE-coated borosilicate glass fiber filter (Fiberfilm^{TM} Filters, Pall Corporation) continuously loaded by aerosols during sampling. ATN is calculated as:

$$ATN = 100 \times \ln\left(\frac{I_0}{I}\right) \tag{6.1}$$

where I_0 and I are the light intensities transmitted throughout a reference blank spot and the aerosol-laden 3 mm diameter sample spot of the filter.

The attenuation coefficient of the filtered aerosol particles, b_{ATN}, can be derived from ATN as follows (Weingartner et al., 2003):

$$b_{ATN} = \frac{A}{100Q}\frac{\Delta ATN}{\Delta t} \tag{6.2}$$

where ΔATN indicates the ATN variation during the time period Δt, A is the sample spot area (7.1×10^{-6} m^2) and Q is the volumetric flow rate (2.5×10^{-6} m^3 sec^{-1}). The aerosol absorption coefficient, b_{abs} , is calculated as follows:

$$b_{abs} = \frac{b_{ATN}}{C \times R(ATN)} \tag{6.3}$$

where C and $R(ATN)$ are the multiple scattering optical enhancement and the aerosol loading factors, respectively. Briefly, the constant optical enhancement factor C compensates for the enhanced optical path through the filter caused by multiple scattering induced by the filter fibers themselves (Schmid et al., 2006; Arnott et al., 2005; Weingartner et al., 2003). For the AE51 microAeth®is 2.05 ±

0.03 (at $\lambda = 880$ nm) (Ferrero et al., 2011a). Conversely, $R(ATN)$ compensates for the nonlinearity - the loading effect due to an increase in the aerosol absorption over time, which in turn results in a reduction in the optical path; it is needed only when ATN becomes higher than 20 (Schmid et al., 2006; Arnott et al., 2005; Weingartner et al., 2003). In this study, the experimental design allows to neglect the use of $R(ATN)$: all BC vertical profiles were conducted by changing the filter ticket between profiles, thus resulting in ATN always lower than 20 as recommended by Weingartner et al. (2003). It is necessary to underline that, to rightly estimate DRE profiles, multiple-wavelengths optical properties are needed (section 2.4); thus the babs derived from the micro-Aeth®AE51 at 880 nm was used in this study during the validation of the optical properties calculation (section 2.3 and 3.2.1) to verify their correct shaping in order to avoid the presence of compensatory effects along profiles. Finally, to determine the BC ambient concentration the apparent mass attenuation cross-section ($\sigma ATN = 12.5$ m^2 g^{-1}) is needed; it is defined for the BC collected on the PTFE-coated borosilicate glass fiber filter (considering the optical components of the instrument) and is provided by the manufacturer. The BC concentrations are determined as follows:

$$BC = \frac{b_{ATN}}{\sigma_{ATN}} \tag{6.4}$$

Aerosol chemistry determination

The knowledge of aerosol chemical composition along height is fundamental to calculate the aerosol refractive index along vertical profiles (section 2.3.1), which is the basis for the correction of the OPC size-distribution (section 2.3.2), for the determination of aerosol optical properties and DRE calculations (sections 2.3, 2.4, 3.2 and 3.3). BC concentrations were measured with a micro-Aethalometer, as reported in the previous section (2.2.1). Moreover, at ME site only, a 7-λ Aethalometer (AE31, Magee Scientific) was also present at ground level, and recorded ground BC concentrations continuously during the campaign. In or-

der to complete the aerosol chemistry along profiles, $PM_{2.5}$ samples were collected during balloon flights at two different heights: ground-level (below the mixing height: BMH), and above the mixing height (AMH: $\sim$600 m AGL, depending on the local atmospheric conditions). $PM_{2.5}$ at ground level was sampled using the TECORA ECHO-PM gravimetric system ($PM_{2.5}$ sampling head, flow 2.3 m^3 h^{-1}; STERLITECH Polycarbonate filters, $\oslash$=47 mm), while at higher altitudes it was sampled using a balloon-borne portable cascade impactor (Sioutas type with Leland Legacy pump, SKC; 9 L min^{-1}; STERLITECH Polycarbonate filters, $\oslash$=37 mm). $PM_{2.5}$ samples were analyzed to determine the water-soluble ionic fraction (Perrone et al., 2012). Water-soluble ions were extracted by ultrapure water (Milli-Q) in an ultrasonic bath (20 minutes; SOLTEC SONICA®). Cations (Na^+, NH^{4+}, K^+, Mg^{2+} and Ca^{2+}) have been determined by a Dionex ICS-90 (Ion Pac CS12A-5 μm column, using methanesulfonic acid as eluent in an isocratic concentration of 0.4 M at 0.5 mL min^{-1}). Anions (Cl^-, NO^{3-}, SO_4^{2-}), together with mono and dicarboxylic acids (formiate, acetate, propionate, oxalate, malonate, succinate, glutarate), were analyzed by a Dionex ICS-2000 (Ion Pac AS11A-5 μm column using KOH at 1.2 mL min^{-1} with a gradient elution between 1.0 mM and 28 mM). The organic matter (OM) fraction was estimated from PM data (section 2.2.1) both BMH and AMH considering the OM fraction derived from wintertime averaged data contained in previous works (Perrone et al., 2012; Ferrero et al., 2011a). Moreover, for the purpose of the refractive index estimation the OM was divided into: the water-soluble OM (WSOM) and the water-insoluble OM (WINSOM). They were calculated using a WSOM/TC (TC = total carbon) coefficient of 0.33 for BMH data and of 0.61 for AMH data during wintertime as derived from data reported in Carbone et al. (2010). Finally, since the determination of aerosol DRE requires the knowledge of the aerosol properties along the whole atmospheric column, the intrinsic limit due to the maximum height of flight allowed for balloons (800 m AGL) was overcome using a standard continental-average profile of aerosol

chemistry, as defined by the OPAC model (Hess et al., 1998), for aerosol over 1 km. Accordingly, three broad-range altitude layers were considered: BMH (from ground to MH), AMH (from MH to ~1 km), Free Troposphere (FT: 1-11 km). The reliability of all the aforementioned assumptions will be discussed in section 3.2.1 through a careful validation of the results with AERONET (columnar validation) and Aethalometer data (validation along the profile).

6.3.3 Aerosol Optical Properties

Aerosol optical properties were calculated along vertical profiles using a Mie code (Bohren and Huffman, 1983) to subsequently evaluate the aerosol DRE (sections 2.4 and 3.4) that requires the extinction coefficient b_{ext} (the sum of scattering and absorption coefficients), the single scattering albedo (SSA) and the aerosol phase function (P) as input parameters. For this purpose the scattering and absorption coefficients (b_{sca} and b_{abs}) were calculated from the integration of the corresponding scattering and absorption efficiencies (Q_{sca} and Q_{abs}) over the whole number-size distribution (Seinfeld and Pandis, 2012):

$$b_{sca/abs} = \int_0^{D_p^{max}} \frac{\pi D_p^2}{4} Q_{sca/abs}(m, x) n(D_p) dD_p \qquad (6.5)$$

where m and n are the aerosol complex refractive index and the size parameter, respectively, while $n(D_p)$ represents the number-size distribution as a function of aerosol diameter (D_p).

From the knowledge of b_{sca} and b_{abs} profiles, the SSA along height was calculated:

$$SSA = \frac{b_{sca}}{b_{sca} + b_{abs}} \qquad (6.6)$$

Finally, the aerosol phase function P is defined as the normalization of the Mie scattering function over the whole 4π spherical angle. For an aerosol characterized

by a complex refractive index m and a size parameter x, $P(\theta, x, m)$ is defined as follows (Crosbie and Davidson, 1985):

$$P(\theta, x, m) = \frac{i(\theta, x, m)}{\frac{1}{2} \int_0^\pi i(\theta, x, m) sin\theta d\theta} \tag{6.7}$$

where $i(\theta)$ is the Mie scattering function which, for unpolarized light, is the average between the perpendicular and parallel components: $i_1(\theta)$ and $i_2(\theta)$ respectively.

The aerosol optical properties were calculated over five wavelengths (270, 441, 675, 880 and 3200 nm) in order to cover the solar spectrum (section 2.4); moreover, three of them (441, 675 and 880 nm) represent the main bands used in the AERONET network allowing the validation of the methodology presented here (section 3.2).

It has to be noticed that the calculation of aerosol optical properties (equations 6.5-6.7) requires an accurate knowledge of the aerosol refractive index, the aerosol size-distribution, the aerosol shape and the aerosol mixing state.

As these basic aerosol properties (chemistry, size, shape, mixing state) can seriously affect the optical properties calculation, in the following sections we discuss: 1) the assumptions used in the calculations and their applicability (shape and mixing state; section 2.3.1), 2) the methodology followed to calculate the aerosol refractive index (section 2.3.2) and 3) the aerosol size distribution treatment starting from OPC data (section 2.3.3). In this respect, particular attention has been given to the choice of the method for calculating the refractive index and to the introduction of appropriate corrections to the aerosol number size distributions measured by the OPC.

Assumptions

The experimental package used for measuring vertical aerosol profiles allowed determining the aerosol chemistry and the aerosol size distribution, while no information about aerosol shape and mixing state was available. Consequently, aerosol

particles were assumed as internally mixed and spherical. These two assumptions are logically connected and based on previous observations conducted over the investigated sites.

The first assumption (internal mixing) is related to the observation that optical properties were calculated along vertical profiles (within and above the mixing layer) and not in proximity of a combustion source (i.e. close to a traffic line) thus giving the time for particles to age and promote an internal mixing. As a matter of fact, the aging along vertical profiles is reported in literature (McMeeking et al., 2011; Cahill et al., 2012; Morgan et al., 2010; Ferrero et al., 2012; Moroni et al., 2013) and it is also described in section 3.1.2. This behavior is also supported by several observations conducted in the past along vertical profiles (more than 300 profiles between 2005 and 2008) over the investigated sites (MI and TR) reported in Ferrero et al. (2012) and in Moroni et al. (2013). During these experiments it was evidenced (through size distribution analysis, chemical speciation and SEM-EDS analysis) an increase of the mean size of aerosol with height that, along with the observed increase in secondary aerosol components (i.e. ammonium nitrate), sphericity, and correlation among fine aerosol particles, indicated the influence of recurrent aging dynamics; moreover, SEM data evidenced the internal mixing state of most of the collected particles. These results support the use of the internal mixing scenario and, at the same time, the assumption of sphericity as reasonable for the context of this application.

Aerosol refractive index

The complex refractive index ($m = n + ik$) of aerosol was calculated considering a hybrid internal/external mixing scenario. The coarse ($D_p > 1\mu m$) and fine ($Dp \leq 1\mu m$) particles were considered externally mixed, each one characterized by its proper value of m (Ferrero et al., 2011a). Coarse particles ($D_p > 1\mu m$) were assumed to be composed of dust, while m for fine particles was calculated from the measured $PM_{2.5}$ chemical composition (sections 2.2.2 and 3.1) using the

Bruggeman mixing rule (or effective medium approximation: EMA) (Stier et al., 2007; Aspnes, 1982; Heller, 1965; Bruggeman, 1935). This approximation does not consider a simple coated sphere assumption. On the contary, it is part of a more general mixing rule formulation resumed in Aspnes (1982) as follows:

$$\frac{\epsilon_{eff} - \epsilon_h}{\epsilon_{eff} + 2\,\epsilon_h} = \sum_{i=1}^{n} f_i \frac{\epsilon_i - \epsilon_h}{\epsilon_i + 2\,\epsilon_h} \tag{6.8}$$

where ϵ_{eff} is the complex effective dielectric constant of the mixture ($m_{eff} \approx \sqrt{\epsilon_{eff}}$) and ϵ_i and f_i are the complex dielectric constant and the volume fraction, respectively, of the ith component; finally, ϵ_h represents the dielectric function of the host medium.

Depending on the choice of host medium, Equation 6.8 can originate three different mixing rules: (1) Maxwell-Garnett (MG) if the host medium is one of the components ($\epsilon_i = \epsilon_h$) (Stier et al., 2007; Aspnes, 1982; Bohren and Huffman, 1983; Heller, 1965) and in this case it is possible to refer to the Maxwell-Garnett as coated sphere assumption; (2) Lorentz-Lorenz (LL) if the host medium is the vacuum ($\epsilon_h = 1$) (Liu and Daum, 2008; Aspnes, 1982; Heller, 1965) and (3) Bruggeman (BR or EMA) if no choice of host medium is made, and inclusions are considered embedded in the effective medium itself ($\epsilon_h = \epsilon_{eff}$) (Stier et al., 2007; Aspnes, 1982; Heller, 1965; Bruggeman, 1935) Stier et al. (2007) and Aspnes (1982) point out that the EMA overcomes the dilemma of the choice of host medium among the various aerosol components. From this point of view, the EMA considers all the possible positions of each aerosol component (BC, dust, water-soluble materials, etc.) with respect to the others. Thus, it allows simulating the real complexity of aerosols and it is suitable for use in calculating the aerosol m_{eff}. For this reason, the EMA does not consider a simple coated sphere assumption and implies that the left part of the aforementioned equation vanishes giving the Equation 6.9 reported here below:

$$\sum_{i=1}^{n} f_i \frac{\epsilon_i - \epsilon_h}{\epsilon_i + 2\,\epsilon_h} = 0 \qquad (6.9)$$

As the EMA simulates the real complexity of aerosols (considering all possible positions of each component in an aerosol particle), it avoids the risk of overestimating the imaginary part (k) of m, thus reducing the uncertainties, as instead happens using both the linear volume-average and the linear mass-average mixing rules in the presence of highly absorbing inclusions (i.e., BC) in a non-absorbing medium (i.e., NH_4NO_3 and $(NH_4)_2SO_4$) (Stier et al., 2007; Lesins et al., 2002; Chylek and Wong, 1995).

Thus, vertical profiles of aerosol refractive index were calculated from the aerosol chemical composition along height using the EMA; in this respect the missing mass was assigned equally to both water and dust (Ferrero et al., 2011a) since it has been shown that a certain amount of water is bound to particles (Subramanian et al., 2007; Hueglin et al., 2005; Rees et al., 2004), and also that this amount is comparable to dust in winter (Hueglin et al., 2005; Rees et al., 2004). Densities (ρ) of pure compounds were used to estimate the volume fraction of each aerosol component (Fierz-Schmidhauser et al., 2010; Pesava et al., 2001; Chazette and Liousse, 2001; Heller, 1965).

A detailed description of refractive indexes and densities of pure aerosol components used in the calculation, and yet successfully applied along vertical profiles, is reported in Ferrero et al. (2011a). The density and refractive index values were carefully chosen from the literature (especially for BC) considering only state-of-the-art values; here we summarize these choices. Refractive indexes as a function of λ for water-soluble components, water-insoluble components and dust were that reported by Hess et al. (1998),while the chosen value for the BC refractive index was that suggested in Bond et al. (2013) 1.85+i0.71. However, the latter value is referred to 550 nm only and thus, the wavelength dependence of BC refractive index reported in Ackerman and Toon (1981), and yet successfully used in Ferrero

et al. (2011a), was applied to the Bond and Bergstrom (2006) value in order to calculate the aerosol optical properties over the whole solar spectrum. The density (ρ) values were 1.75, 1.45, 1.45 and 2.6 g cm^{-3} for ionic components WSOM, WINSOM and dust, respectively. These values lie at the midpoint of published data reported in Ferrero et al. (2011a), and references therein.

Since the aforementioned choices, especially for what concern the BC density and refractive index would affect the aerosol refractive index calculation, a sensitivity test was conducted varying the density and refractive index of pure BC in input to the EMA. In particular, results obtained using the density (1.8 g cm^{-3}) and the refractive index (1.85+0.71i) suggested in Bond et al. (2013)were compared to (1) those obtained with the density (1.0 g cm^{-3}) and the refractive index (1.75+0.44i) used in the OPAC software Hess et al. (1998)and (2) those obtained with the density (2.0 g cm^{-3}) and the refractive index (2+1i) reported in Roessler (1984).These two references are of high importance as they report the lowest density (never observed) and one of the highest imaginary part reported in literature, respectively. Results are discussed in section 3.2.1.

Finally, the aerosol refractive index was determined point by point along vertical profiles, considering the hygroscopic growth of the aerosol:

$$D_{wet} = D_{dry} \left(\frac{1 - RH}{1 - DRH} \right)^{-\epsilon} \tag{6.10}$$

where RH is the ambient relative humidity, D_{dry} is the aerosol diameter at the deliquescence relative humidity (DRH) and D_{wet} is the aerosol diameter at ambient RH; ϵ is the coefficient controlling the aerosol's hygroscopic growth. Since the ground-level chemical composition of dry aerosol measured at TR, MI and ME (Sect. 3.1.2) was similar to that reported in Randriamiarisoa et al. (2006) and Raut and Chazette (2008), we set ϵ accordingly to 0.26.

DRH was estimated using the aerosol's chemical composition for each site along all the profiles as input to the thermodynamic aerosol inorganic model (E-AIM Model-II) (Clegg et al., 1998) (http://www.aim.env.uea.ac.uk/aim/aim.php).

This is a state-of-the-art aerosol thermodynamic model for the H^+-NH_4^+-SO_4^{2-}-NO_3^- -carboxylic acids-H_2O composition of the aerosol (Zhang et al., 2000). This model had been already used to accurately predict aerosol DRH (Ferrero et al., 2013; Hueglin et al., 2005; Pathak et al., 2004). DRH values are discussed in Sect. 3.1.2. From hygroscopic growth, the EMA was applied point by point along height to calculate the final aerosol refractive index every 3.0 m for each profile.

As the aforementioned choices (EMA, m and ρ for pure components, hygroscopic growth) can seriously affect the optical properties calculation, the calculated refractive index and the aerosol optical properties were validated in detail, as presented in Sect. 3.2.

Aerosol size distribution

The determination of aerosol optical properties requires an accurate knowledge of the aerosol size distribution. In this study, the aerosol size distribution was measured using the OPC Grimm 1.107 (λ=655 nm) that classifies the aerosol particles in terms of optical equivalent diameter which is, as defined by Howell et al. (2006), "the diameter of a sphere of known refractive index (that of polystyrene latex spheres of calibration) that scatters light as efficiently as the real particle in question". This effect originates the "undersizing" problem, which occurs due to the OPC calibration with polystyrene latex spheres (PLS; m = 1.58 at 655 nm; Ma et al. (2003)) whose refractive index has usually a larger real part compared to ambient aerosol (Sect. 3.2.1) (Guyon et al., 2003; Liu and Daum, 2008; Schumann, 1990). Moreover, the OPC has a PLS equivalent size range between 0.25 and 32 μm, which originates a "truncation effect". Thus, both the "undersizing" and the "truncation effect" need to be compensated to calculate the aerosol optical properties. The "undersizing" was solved correcting the OPC size channels to account for the ambient aerosol refractive index m; the OPC response function (S: the partial light scattering cross section of the particle related to the specific

optical design of the OPC) was computed at 655 nm as follows (Kulkarni et al., 2011; Heyder and Gebhart, 1979)

$$S(\theta_0, \Delta\Omega, x, m) = \frac{\lambda^2}{4\pi^2} \int \int_{\Delta\Omega} i(\theta, \Phi, x, m) sin\theta \, d\theta \, d\Phi \qquad (6.11)$$

where θ_0 represents the mean scattering angle of the optical arrangement, $\Delta\Omega$ the receiver aperture, x the dimensionless size parameter, m the refractive index and $i(, \Phi, x, m)$ the Mie scattering function composed by the perpendicular and parallel components: $i_1(\theta, x, m)$ and $i_2(\theta, x, m)$, respectively. The optical arrangement of the OPC 1.107 consists of (1) a wide angle parabolic mirror (121°; from 29.5 to 150.5°; $\theta_0 = 90°$) that focuses scattered light on the photodetector located on the opposite side and (2) 18° of direct collected scattered light on the photodetector (from 81 to 99°; $\theta_0 = 90°$) (Heim et al., 2008). The response function was calculated both for PLS (SPLS) and for ambient aerosol (SAMB) along each vertical profile, within and above the mixing layer. The refractive indexes of ambient aerosol used in SAMB calculations were calculated as reported in Sect. 2.3.1: (1) m for fine particles calculated applying the EMA (Sect. 2.3.1) and (2) m of dust for coarse particles. Table 6.1 of Ferrero et al. (2014) shows the columnar means of the new size corrected channels for TR, MI and ME: results agreed with literature studies (Ferrero et al., 2011a; Liu and Daum, 2008; Schumann, 1990).

| OPC Channel | Instrument size | | Ambient size (μm) | |
	PLS (μm)	Terni	Milano	Merano
1	0.25	0.27	0.27	0.26
2	0.28	0.30	0.30	0.30
3	0.30	0.32	0.33	0.32
4	0.35	0.38	0.39	0.38
5	0.40	0.46	0.47	0.45
6	0.45	0.52	0.53	0.52
7	0.50	0.56	0.58	0.56
8	0.58	0.75	0.79	0.75
9	0.65	0.80	0.91	0.81
10	0.70	0.90	0.94	0.90
11	0.80	1.00	1.06	1.00
12	1.00	1.35	1.35	1.33
13	1.30	1.78	1.78	1.78
14	1.60	2.14	2.14	2.14
15	2.00	2.40	2.40	2.40
16	2.50	2.82	2.82	2.82
17	3.00	3.67	3.67	3.67
18	3.50	4.62	4.62	4.62
19	4.00	5.01	5.01	5.01
20	5.00	5.89	5.89	5.89
21	6.50	9.55	9.55	9.55
22	7.50	10.72	10.72	10.72
23	8.50	12.16	12.16	12.16
24	10.00	16.03	16.03	16.03
25	12.50	22.65	22.65	22.65
26	15.00	29.85	29.85	29.85
27	17.50	37.15	37.15	37.15
28	>20.00	>44.67	>44.67	>44.67

Table 6.1: Originl size channels of OPC Grimm 1.107 calibrated with PLS (left side) and corrected (right side, columnar average) for the ambient refractive index determined over TR, MI and ME.

The second effect (truncation effect) made the accumulation mode only partially measured (lowest equivalent PLS size of OPC: 0.25 μm) while, the coarse mode was completely defined. No measurements were available for Aitken mode particles (D_p <0.1 μm). Even if a negligible error ($\sim$2-4 %) comes from not considering the Aitken mode in the optical properties calculation (Bond and Bergstrom, 2006; Guyon et al., 2003; Liu and Daum, 2008; Randriamiarisoa et al., 2006), the truncation effect in the accumulation mode cannot be neglected and has to be solved.

For this purpose, a log-normal interpolation of the aerosol number-size distribution was conducted for each OPC data measured along vertical profiles to complete the aerosol size distribution function $n(D_p)$. This procedure has to be conducted only after the correction of the OPC size channels (Eq. 10) and had been already successfully applied in Ferrero et al. (2011a), Deshler et al. (2003), and Angelini et al. (2009).

As the aerosol optical properties are closely dependent on the reliability of the aerosol number-size distribution, the main parameters describing the aerosol size distribution (geometric mean diameter and geometric standard deviation), together with the aerosol optical properties, were validated with care, as explained in Sect. 3.2. Sensitivity tests related to the size-distribution correction and interpolation are reported and discussed in Ferrero et al. (2011a) and were not repeated here.

6.3.4   Radiative transfer and heating rate calculations

Aerosol scattering and absorption of solar radiation modify the intensity and spectral distribution of surface incoming solar radiation. Thus, aerosol DRE can be estimated by means of radiative transfer model (RTM) simulations. In this work the RTM libRadtran (Mayer et al., 2005) was used for this purpose, adopting as radiative transfer equation solver the discrete ordinate code disort (Stamnes et al.,

1988) with 18 streams. The correlated-k approach of Kato (Kato et al., 1999) was used to compute the atmospheric spectral transmittance taking into account the absorption coefficients of different gases.

RTM simulations were performed in cloud-free conditions (as the vertical profile measurements) at the three measurement sites (TR, MI and ME) at 15 min intervals for each day of the measurement campaign, from 11:00 to 13:45 UTC. The average was computed in order to obtain an estimate of the maximum radiative forcing of aerosol, which is generally observed around noon.

Three main inputs were used in the RTM simulations, namely, (1) aerosol optical properties along vertical profiles, (2) atmospheric profiles of gases and meteorological parameters and (3) surface albedo.

The vertical profiles of aerosol optical properties (b_{ext}, SSA, $P(\theta)$) that were used as input for the RTM were the ones calculated over TR, MI and ME, as reported in the previous section (Sect. 2.3).

The vertical profiles of aerosol optical properties (b_{ext}, SSA, $P(\theta)$) that were used as input for the RTM were the ones calculated over TR, MI and ME, as reported in the previous section (Sect. 2.3).

Atmospheric profiles of pressure, temperature, air density, ozone, oxygen, water vapor, CO_2 and NO_2 concentrations were defined by using the standard atmospheric data as defined by Anderson et al. (1986), for Midlatitude Winter. The vertical resolution of these profiles was 1 km from 0 to 25 km a.m.s.l., 2.5 km from 25 to 50 km a.m.s.l. and 5 km from 50 to 120 kma.m.s.l.

Finally, surface albedo values used for the simulation derive from retrievals from the moderate resolution imaging spectroradiometer (MODIS) V005 climate modeling grid (CMG) Albedo Product (MCD43C3). For each site, the average value at the nearest pixel during the measurement campaign was adopted.

The instantaneous aerosol DRE (Wm^{-2}) was quantified as the change in the net radiative flux between the atmospheric conditions with and without the aerosols in the atmosphere as follows:

$$DRE_z = F_{aer,z} - F_{w/o-aer,z}, \tag{6.12}$$

where F is the radiative flux, and the subscripts aer, z and $w/o-aer, z$ refers to the atmospheric conditions with and without aerosol at the height z, respectively.

Since the atmospheric aerosol is characterized by a significant absorptive capacity (Sect. 3.3), the difference between the DRE at the top and the bottom of each atmospheric layer represents the instantaneous radiative power density absorbed by the aerosol within that atmospheric layer (ΔDRE_{ATM}; Wm^{-2}) as follows (Chakrabarty et al., 2012; Kedia et al., 2010):

$$\Delta DRE_{ATM} = DRE_{z+\Delta z} - DRE_z, \tag{6.13}$$

where Δz is the differential thickness within each atmospheric layer (each measuring point along vertical profiles; Sect. 2.1).

ΔDRE_{ATM} is expressed in Wm^{-2} which is the common metric used in literature to quantify the integrated radiative power density absorbed by the aerosol in the atmospheric layer; this situation occurs as usually the aerosol absorption in the atmosphere is evaluated over altitude thick layer of the atmosphere and/or over the whole atmospheric column (Heald et al., 2014; Bond et al., 2013; Das and Jayaraman, 2011; Kedia et al., 2010).

However, in order to study the absorptive DRE ($ADRE$) of the aerosol in the atmosphere along continuous high resolution vertical profiles, the aforementioned metric could be misleading, as absolute values of ΔDRE_{ATM} depend on the thickness of the layer Δz across which the DRE difference is computed. To compare measurements taken at different sites with a different vertical resolution, the ADRE was computed simply normalizing ΔDRE_{ATM} by the thickness Δz:

$$ADRE = \frac{\Delta DRE_{ATM}}{\Delta z}. \tag{6.14}$$

In this way, the $ADRE$ represents the radiative power absorbed by the aerosol for unit volume of the atmosphere ($\mathrm{Wm^{-3}}$) and allows describing continuous vertical profiles of atmospheric absorption induced by aerosol even comparing data taken at different sites. Another illustration of the $ADRE$ meaning is that it is the vertical derivative of the DRE ($dDRE/dz$) as follows from Eq. (14).

Moreover, the $ADRE$ can be directly related to the atmospheric heating rate (HR; see below). In fact, on the basis of the energy conservation principle, the absorbed radiant power must heat the atmospheric layer; the instantaneous HR is conventionally given by (Chakrabarty et al., 2012; Kedia et al., 2010):

$$HR = \frac{\delta T}{\delta t} = -\frac{g}{C_p} \frac{\Delta DRE_{ATM}}{\Delta P}, \qquad (6.15)$$

where $\delta T/\delta t$ represents the instantaneous HR ($\mathrm{K\ day^{-1}}$) of each atmospheric layer, g is the acceleration due to gravity, C_p ($1005\ \mathrm{J\ kg^{-1}\ K^{-1}}$) is the isobaric specific heat of dry air, ΔP is the pressure difference between the top and the bottom of each atmospheric layer. From Eq. (15), considering the relationship between atmospheric pressure and height through the hydrostatic equation ($dp = -\rho\, g\, dz$), it is possible to relate the HR linearly to the $ADRE$ in each atmospheric layer:

$$HR = \frac{\delta T}{\delta t} = -\frac{1}{\rho C_p} \frac{\Delta DRE_{ATM}}{\Delta z} = \frac{1}{\rho C_p}\, ADRE. \qquad (6.16)$$

The $ADRE$ and HR behavior along vertical profiles is discussed in Sect. 3.4.

6.4   Results and discussion

We measured the BC and aerosol vertical profiles to determine their direct radiative effect. The obtained results are discussed here in order to highlight first the BC vertical distribution in relation to the MH (Sect. 3.1). Then, vertical profiles of aerosol optical properties are validated in Sect. 3.2 and discussed in Sect. 3.3.

Finally, the aerosol DRE along height is presented together with considerations on possible feedbacks on lower troposphere (Sect. 3.4). All averaged data are reported here as mean $\pm$ mean standard deviation.

6.4.1 Vertical profile measurements

Black Carbon and aerosol profiles

The main features of BC and aerosol vertical distribution during the campaign can be highlighted considering, as a case study, the vertical profiles measured on 28 January 2010 (13:45-14:26 UTC) over TR; they are reported in Fig. 6.2 together with the corresponding potential temperature (T) and RH profiles.

Figure 6.2 highlights that the BC and the total particle number concentrations were constrained close to ground, within the first 170 m a.g.l., where a strong negative gradient of both of them was present. At the same height an evident decrease of RH (-3.5 %) and a small increase in T (+0.7 K) were observed, allowing to set the MH at 170 m.

Thus, considering changes across the MH, the BC concentration decreased going from BMH to AMH characteristics by -60.4 $\pm$ 2.3% (from 5.63 $\pm$ 0.16 to 2.23 $\pm$ 0.05 μgm^{-3} for BC) and the aerosol concentration by -35.4 $\pm$ 0.2% (from 869 $\pm$ 2 to 562$\pm$2 cm^{-3} for aerosol). Consequently, the vertical profiles reported in this case study (Fig. 6.2) indicate that (1) BC and aerosol concentrations were shaped in the same way by atmospheric turbulence and constrained within the MH; (2) BC experienced a higher concentration drop at the MH than the aerosol number concentration did.

In order to better investigate these features, all the vertical profiles measured over the investigated basin valleys (TR, MI and ME) were statistically averaged for each site.

As reported in previous works (Ferrero et al., 2011a, 2012),a way to average vertical profile data by taking the daily evolution of the MH into account, is to
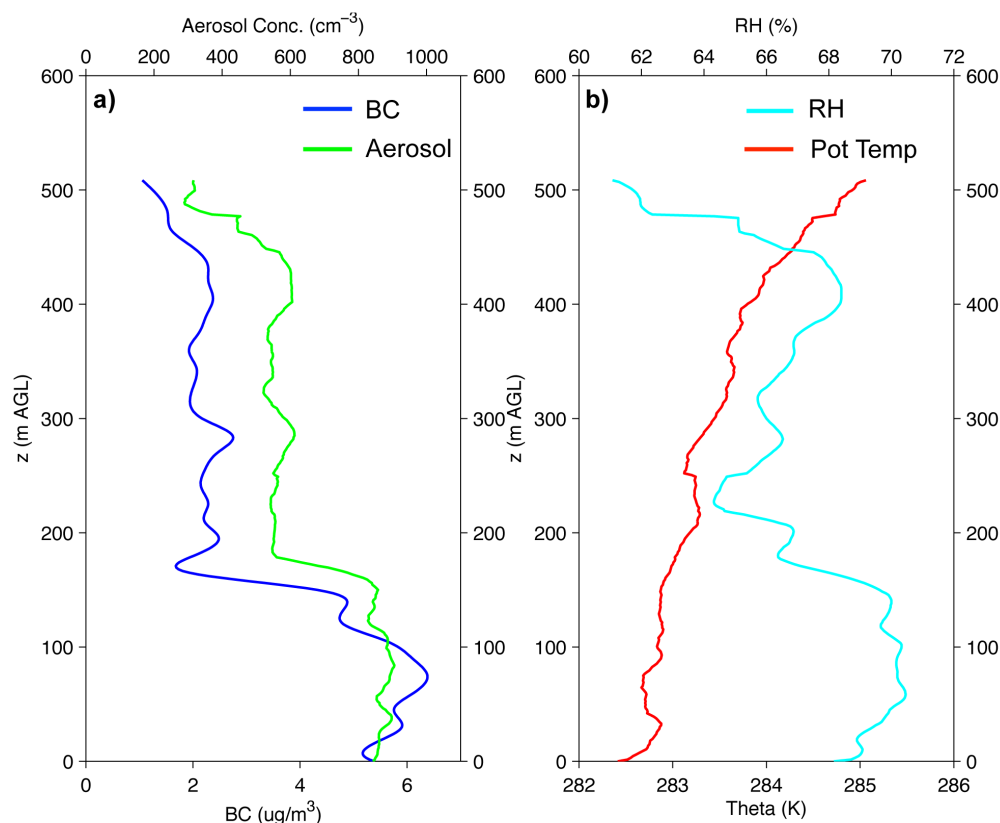
Figure 6.2: Vertical profiles measured over TR on 28 January 2010 (13:45-14:26 UTC): (a) BC (blue line) and aerosol (green line, OPC total particle-number concentration); (b) potential temperature (red line) and relative humidity (light blue line).

consider the relative position of each measured data point in respect to the MH. Thus, vertical profiles were first normalized, introducing a standardized height H_s) calculated as follows:

$$H_s = \frac{z - MH}{MH},\tag{6.17}$$

where z is the height above ground. H_s assumes a value of 0 at the MH, and values of -1 and 1 at ground-level and at twice the MH, respectively.

The MH was determined applying the gradient method (Sect. 2.2) to each profile of aerosol concentration (p-MH), T (T-MH) and RH (RH-MH). Figure 6.3 shows an excellent correlation ($R^2 > 0.9$) with linear best fits close to the ideal ones; this result illustrates the reliability and physical interconsistence of the MH

determination from different parameters. Therefore, for the purpose of this work and for using of Eq. (17), we are going to refer to the MH as that derived from the aerosol concentration gradient (p-MH), hereinafter indicated simply as MH.
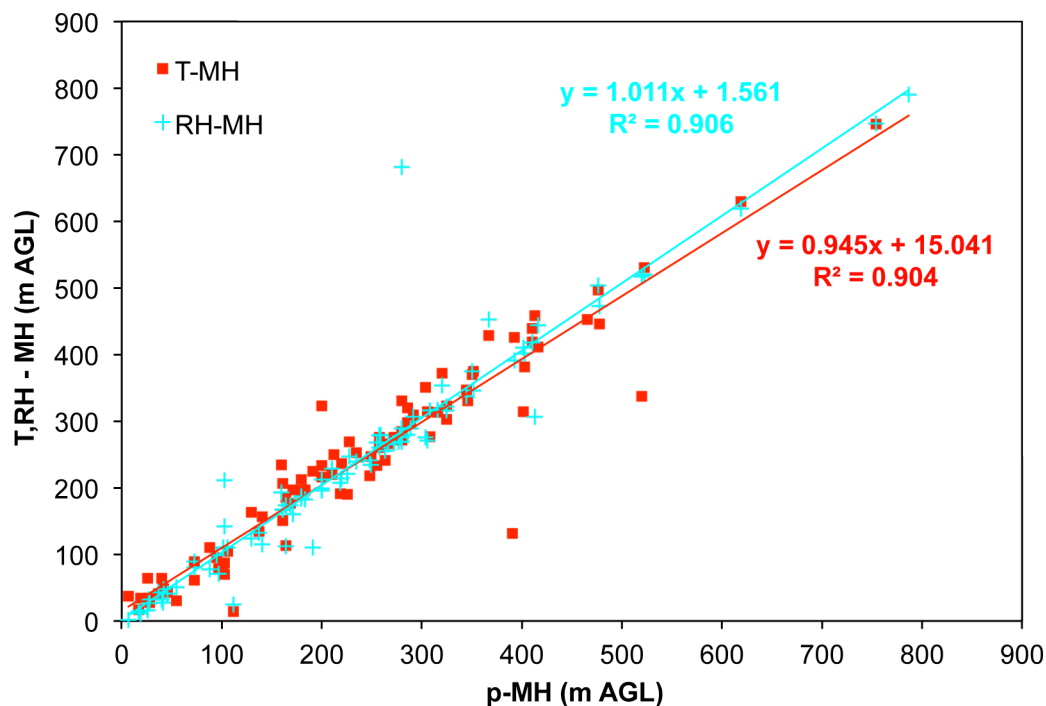
Figure 6.3: Linear correlation between the mixing height derived from each vertical profile of aerosol concentration (p-MH) temperature (T-MH) and relative humidity (RH-MH).

The average MH measured in the three sites was 142 ± 22m (TR), 272 ± 50m (MI) and 173 ± 42m (ME). These values reflected a common meteorological situation for the Italian basin valleys, characterized by conditions of high atmospheric stability. Reported MH values are also in agreement with those previously reported for TR and MI in Ferrero et al. (2012).

Next the standardized vertical profiles were averaged. Figure 6.4 shows the resulting statistical mean profiles calculated over TR, MI and ME, for both BC and aerosol number concentration; some common behaviors can be observed among the three sites:

1. At the MH (Hs = 0) a marked concentration drop of both BC and total aerosol concentration was observed. Crossing the mixing height, BC concen-
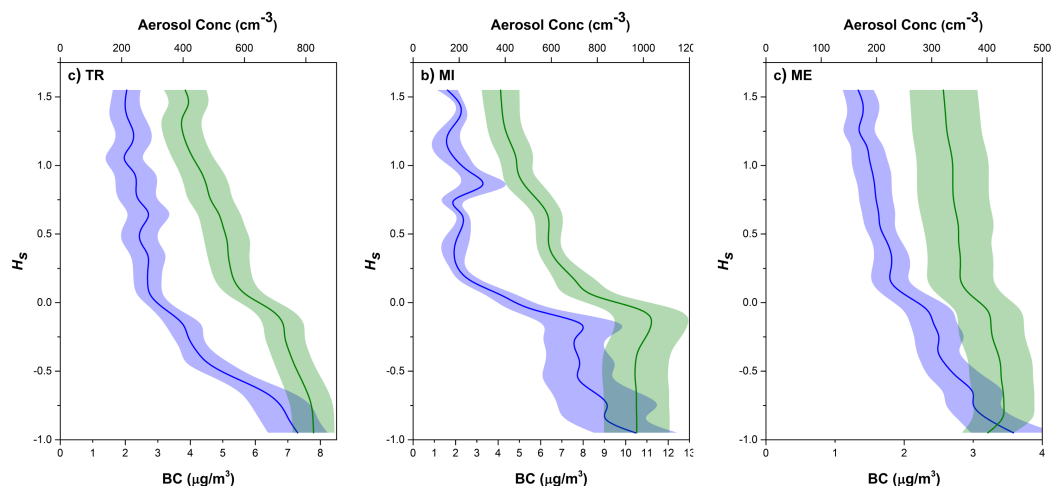
Figure 6.4: The statistical mean profiles of both BC and aerosol number concentrations along standardized height H_s over TR (a), MI (b) and ME (c).

trations decreased over TR by -69.1 $\pm$ 5.5% (from 5.63 $\pm$ 0.55 to 1.67 $\pm$ 0.36 μg m^{-3}), over MI by -66.2 $\pm$ 7.8% (from 7.57 $\pm$ 1.28 to 2.03 $\pm$ 0.34 μg m^{-3}) and over ME by -48.4 $\pm$ 5.3% (from 2.75 $\pm$ 0.38 to 1.35 $\pm$ 0.17 μg m^{-3}). Aerosol concentrations (from BMH to AMH) behave similarly, decreasing over TR by -46.5 $\pm$ 7.3% (from 792 $\pm$ 58 to 434 $\pm$ 71 cm^{-3}), over MI by -39.0 $\pm$ 7.3% (from 913 $\pm$ 120 to 506 $\pm$ 50 cm^{-3}) and over ME by -23.9 $\pm$ 4.3% (from 427 $\pm$ 45 to 326 $\pm$ 43 cm^{-3}), respectively. Thus, the experimental results evidenced the crucial role played by the MH in shaping both the BC and aerosol profiles over basin-valleys. As a result, elevated BC and aerosol loadings were present close to the ground. Another common behavior appeared: the partial decrease of BC across the MH was always higher than the decrease measured for the aerosol number concentration; consequently, the relative abundance of BC in the aerosol decreased along height over the three sites. In fact, considering not only the number concentration, but also the PM$_{2.5}$ mass concentration profiles (estimated by the OPC) and the volume concentration profiles for particles below 2.5 μm (V2.5, calculated from OPC size distribution), the BC content in PM$_{2.5}$ (V2.5) decreased along height by -43.2 $\pm$ 7.3% (-41.8 $\pm$ 7.5 %), -47.5 $\pm$ 7.9% (-45.8 $\pm$ 8.3 %) and -33.2 $\pm$ 4.9%

(-33.0 ± 5.4 %) over TR, MI and ME, respectively, resulting in a vertical change of the BC aerosol fraction (see also Sect. 3.1.2). This is a general behavior measured over basin valleys under atmospheric stagnant conditions and it is in agreement with BC measurements previously conducted just over MI (Ferrero et al., 2011a). The importance of this behavior is discussed in Sects. 3.2 and 3.3 as the BC fraction changes affect the aerosol optical properties (i.e., SSA) and its DRE along height.

2. Within the mixing layer itself, higher BC concentrations were found close to the ground in all the three sites (Fig. 6.4). In particular this ground-level layer affected the first 50-100 m of atmosphere with a BC concentration increase of +34.2% (TR), +17.3% (MI) and +16.1% (ME) compared to the average BC concentration measured BMH. This increase of BC concentration near ground level is related to the proximity to emission sources (traffic, heating, industry) (Trompetter et al., 2013) and was observed for BC only and not for the particle-number distribution. This further strengthens the aforementioned observation of the vertical changes in the BC aerosol fraction.

3. BC concentrations measured AMH were found quite similar over the three sites: 1.67 ± 0.36 μg m^{-3} for TR, 2.03 ± 0.34 μg m^{-3} for MI and 1.35 ± 0.17 μg m^{-3} for ME (Fig. 6.4), indicating the presence of a relatively constant background BC concentration value not directly short-term influenced by the source dynamics at ground.

As reported in literature (Samset et al., 2013; Zarzycki and Bond, 2010), a worldwide lack of knowledge about BC vertical distribution is generally present. Thus, the aforementioned results were used in Sects. 3.3 and 3.4 to assess the related vertical behavior of both aerosol optical properties and aerosol DRE over basin valleys.

Aerosol chemistry along height and DRH

The optical properties calculation along vertical profiles (Sects. 2.3 and 3.2) requires the knowledge of the whole aerosol chemical composition along height. Thus, in addition to BC (Sect. 3.2.1), the other chemical components (ions, OM; Sect. 2.2.2) in PM$_{2.5}$ are discussed here. Figure 6.5 shows the aerosol chemical composition over TR, MI and ME both BMH and AMH.
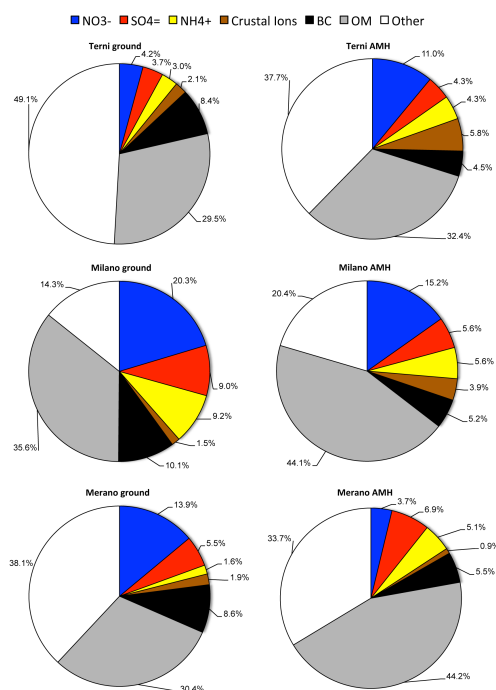
Figure 6.5: Aerosol chemical composition determined BMH and AMH for TR, MI and ME. Data shown are the respective aerosol mass fractions of each individual aerosol species.

As highlighted in the previous section (Sect. 3.2.1), Fig. 6.5 evidences the decrease of BC fraction from BMH (8.4 $\pm$ 1.0% over TR, 10.1 $\pm$ 2.3% over MI and 8.6 $\pm$ 1.5% over ME) to AMH (4.5 $\pm$ 1.2% over TR, 5.3 $\pm$ 1.0% over MI and 5.5 $\pm$ 1.4% over ME).

Conversely, the OM fraction increased with height (from BMH to AMH): from 29.5 $\pm$ 3.6 to 32.4 $\pm$ 8.4% over TR, from 35.6 $\pm$ 8.2 to 44.1 $\pm$ 7.4% over MI and from 30.4 $\pm$ 5.3 to 44.2 $\pm$ 7.3% over ME.

This difference in the vertical behavior of BC and OM is related first to the presence of primary sources of BC within the mixing layer (Trompetter et al., 2013), but also to the possibility of greater secondary aerosol formation AMH.

This is in agreement with results previously reported over the Po Valley (Ferrero et al., 2011a; Perrone et al., 2010) and also over Europe by many authors (Morgan et al., 2009; Hueglin et al., 2005), who all found a lower vertical gradient for organic species.

Ionic species exhibited different behavior over the three sites. Over TR the whole ionic fraction increased $\sim$2 times going from BMH to AMH. The mass fraction of NO_3^- , SO_4^{2-} and NH_4^+ increased from 4.2 $\pm$ 1.8, 3.7 $\pm$ 2.6 and 3.0 $\pm$ 1.5% (BMH) to 11.0 $\pm$ 3.6, 4.2 $\pm$ 1.1 and 4.3 $\pm$ 1.4% (AMH), respectively. This is in agreement with recent studies (Moroni et al., 2013; Ferrero et al., 2012) which point out the presence of an aerosol aging AMH due to both condensation and coagulation.

Over MI the opposite occurred and the ionic fraction globally decreased from 40.0 $\pm$ 9.5% (BMH) to 30.2 $\pm$ 7.2% (AMH). This is also in agreement with previous vertical profiles conducted over MI (Ferrero et al., 2010, 2012) which instead underlined a higher role of the OM (see above) in the aerosol aging AMH over the Po Valley.

Over ME the ionic fraction decreased with height (from 23.0 $\pm$ 9.0% BMH to 16.7 $\pm$ 2.2% AMH) as in MI. However, while in MI and TR NO_3^- remained the most abundant species AMH, over ME SO_4^{2-} dominated. This was due to the alternating influence of both continental aerosol (enriched in SO_4^{2-}) and Po Valley aerosol, that were transported from both north and south, respectively, along the direction of the ME main valley (Sect. 2.1).

All these aspects are crucial in determining the aerosol optical properties because, as reported in Ramana et al. (2010), the ratio of BC to scattering species (i.e., SO_4^{2-}) influences the solar-absorption efficiency. Moreover, the same scattering species (i.e., SO_4^{2-} and NO_3^-) also influence the DRH at which aerosol water

uptake starts, corresponding to a phase change for the aerosol water-soluble compounds which dissociate going from solid to liquid (Martin, 2000; Seinfeld and Pandis, 2012; Potukuchi and Wexler, 1995). Therefore, DRH is of crucial importance to assess the final aerosol optical properties (Di Nicolantonio et al., 2009; Randriamiarisoa et al., 2006).

In this respect, the E-AIM Model II (Sect. 2.3.1) was applied to the H^+-NH_4^+-SO_4^{2-}-NO_3^--carboxylic acids-H_2O composition of the aerosol to accurately predict the aerosol DRH for each site both BMH and AMH. BMH values for TR, MI and ME were close each other: 64.5, 67.0 and 65 %, respectively. They were in agreement with values measured at ground level in MI by means of an aerosol chamber (Ferrero et al., 2014). Values of DRH AMH were 55% (TR), 62% (MI) and 67% (ME). The lowest and the highest values were found over TR and ME due to an increase in the nitrate and sulfate fractions, respectively. As already pointed out by Potukuchi and Wexler (1995), an increase in the nitrate (sulfate) fraction leads to lower (higher) DRH.

All the results presented in this section were used to calculate the aerosol optical properties along vertical profiles (Sect. 3.2) following the methodology reported in Sect. 2.3.

6.4.2 Validation of aerosol optical properties

The vertical profiles of aerosol optical properties were calculated as reported in Sect. 2.3. In this section, the accuracy of the calculated optical properties is discussed (Sects. 3.2.1 and 3.2.2) before investigating their vertical behavior over the three sampling sites (Sect. 3.3). This discussion is necessary because the reliability of the radiative forcing simulations depends on the robustness of the aerosol optical properties calculation.

Thus, the obtained aerosol optical properties underwent three validation procedures: (1) a columnar comparison of a set of parameters (i.e., refractive index, SSA, AOD, etc.) independently obtained by the Aerosol Robotic Network

(AERONET) at 441, 657 and 880 nm (Sect. 3.2.1); (2) a detailed comparison along vertical profiles between the absorption coefficient measured by the micro-Aeth®AE51 at 880 nm and the one which was calculated over TR, MI and ME at the same wavelength (Sect. 3.2.2) and (3) a comparison at ground-level of the absorption coefficient and the Ångström exponent independently obtained using the 7-λ Aethalometer AE31 (Sect. 3.2.2). This triple validation guarantees the quality of both the columnar-averaged optical parameters and their correct shaping along vertical profiles considering different "validation levels" along vertical profiles: the columnar average, the single data points along vertical profiles and the ground-level values. This procedure was necessary to avoid the presence of compensatory effects along profiles and to perform a right estimation of the radiation absorbed in each atmospheric layer (Sect. 3.4).

In this respect, the comparison with AERONET allowed assuring the reliability of the columnar data and had the advantage to be performed on several wavelengths. The comparison with the micro-Aeth®AE51 data allowed to validate the correct shaping of the optical properties along vertical profiles but it was limited to one wavelength (880 nm). The comparison with the 7-λ Aethalometer AE31 allows validating one point of the profiles (ground level) but on several wavelengths.

Finally, in addition to the validation procedure applied here, the methodology followed to calculate the aerosol optical properties was already validated and published in Ferrero et al. (2011a).

Columnar validation (comparison with AERONET)

The quality of the calculated aerosol optical properties was first evaluated along the atmospheric column through a comparison of a set of parameters (i.e., refractive index, SSA, AOD, etc.) independently obtained by the AERONET at 441, 657 and 880 nm (the only overlapping wavelengths between this study and AERONET). Considering the location of TR, MI and ME, only three AERONET stations were

available for this comparison: the Ispra site (45.80° N, 8.63° E; 235 m a.s.l.; 57 km from MI site), the Davos site (46.81° N, 9.84° E; 1596 m a.s.l.; 102 km and 157 km from ME and MI sites) and the Bolzano site (46.46° N, 11.33° E; 262 m a.s.l.; 25 km from ME). Unfortunately, the data in Bolzano (during winter 2010) were strongly affected by local dust deposited on the photometer lens (personal communication by the AERONET Bolzano principal investigator, 2012), thus, only the AERONET sites of Ispra and Davos were considered. Their data were compared with those calculated for MI, which was the nearest site. The Ispra site was used for comparison concerning the entire atmospheric column while the Davos site (1596 m a.s.l.) for the FT, because of its location at high altitude.

MI data were calculated on statistical mean profiles (Sect. 3.1.1) and we accordingly used the AERONET averaged values from 12 to 25 February as a reference in order to assess the accuracy of our optical estimations. It is necessary to underline that, despite the averaging period is the same, the instantaneous values measured by balloon sounding and by AERONET could not have been coincident and this temporal difference may cause small differences during the comparison.

We start the comparison considering the whole atmospheric column; results are summarized in Table 6.2.

The average columnar refractive indexes calculated in this study were $1.501(\pm 0.003)+i0.032(\pm 0.003)$ at 441 nm, $1.500(\pm 0.004)+i0.030(\pm 0.003)$ at 675 nm and $1.494(\pm 0.004)+i0.030(\pm 0.003)$ at 880 nm. They were in agreement with the AERONET Ispra estimations: $1.415(\pm 0.047)+i0.032(\pm 0.009)$ at 441 nm, $1.418(\pm 0.046)+i0.029(\pm 0.006)$ at 675 nm and $1.425(\pm 0.044)+i0.030(\pm 0.007)$ at 870 nm. A slight overestimation of the real part $(+5.6 \pm 0.4 \%)$ was present, while the imaginary part was identical to the measured one.

Instead, results from the sensitivity test (see Sect. 2.3.2) conducted using the density (1.0 g cm^{-3}) and the refractive index ($1.75+0.44i$) of the OPAC software (Hess et al., 1998) and the density (2.0 g cm^{-3}) and the refractive index ($2+1i$) reported in Roessler (1984) highlighted a substantial equivalence of the three sets

of input parameters in determining the real part of the aerosol refractive index, while the imaginary part experienced an average increase of $+23.5 \pm 3.1\%$ and $+22.2 \pm 4.6\%$ (all wavelengths), with respect to AERONET data. This effect was due to the exceedingly low density of the OPAC data (never measured) and to the too high (one of the highest in literature) imaginary part of pure BC reported Roessler (1984).

Parameter	Atmospheric Column					
	AERONET-Ispra(235m)			PROFILES-Milano(136m)		
	441nm	675nm	870nm	441nm	675nm	880nm
n	1.415	1.418	1.425	1.500	1.500	1.494
	(±0.047)	(±0.046)	(±0.044)	(±0.003)	(±0.004)	(±0.004)
k	0.032	0.029	0.030	0.032	0.030	0.030
	(±0.009)	(±0.006)	(±0.007)	(±0.003)	(±0.003)	(±0.003)
SSA	0.812	0.778	0.740	0.857	0.846	0.812
	(±0.028)	(±0.028)	(±0.034)	(±0.013)	(±0.011)	(±0.012)
AOD	0.232	0.124	0.083	0.274	0.152 ($\pm$	0.092 ($\pm$
	(±0.091)	(±0.052)	(±0.035)	(±0.046)	0.034)	0.023)
AOD_{Abs}	0.050	0.032	0.025	0.047 ($\pm$	0.028 ($\pm$	0.020 ($\pm$
	(±0.023)	(±0.015)	(±0.012)	0.010)	0.006)	0.005)
$D_g(\mu m)$	0.206	0.206	0.206	0.204	0.204	0.204
	(±0.016)	(±0.016)	(±0.016)	(±0.010)	(±0.010)	(±0.010)
σ_g	1.552	1.552	1.552	1.560	1.560	1.560
	(±0.045)	(±0.045)	(±0.045)	(±0.060)	(±0.060)	(±0.060)

Table 6.2: Comparison of the columnar optical and size distribution properties of the aerosol derived over MI from vertical profile measurements and over AERONET-Ispra site ($\sim$57 km from MI). n and k are the real and imaginary part of the complex refractive index. SSA is the Single Scattering Albedo. AOD and AOD_{Abs} are the Aerosol Optical Depth and the Absorption Aerosol Optical Depth, respectively. D_g and σ_g are the geometric mean diameter and the geometric standard deviation, respectively.

The comparison with AERONET validate the use of BC density and refractive index reported in Bond and Bergstrom (2006) in input to the EMA together with the methodology used for the aerosol refractive index calculation (EMA, m and ρ for pure components, hygroscopic growth) (Sect. 2.3.1). The validation of the refractive index m is crucial as it is at the basis of the optical calculation both during the OPC size-distribution correction and during the Mie calculation (in which the corrected size distribution is itself an important input parameter).

Thus, as a second control, the corrected and interpolated aerosol size distribution was compared with that retrieved by AERONET Ispra: the calculated accumulation mode geometric mean diameter (D_g: 0.204±0.010 Î¼m) and the geometric standard deviation (σ_g: 1.560 ± 0.060) agreed very well with AERONET Ispra (D_g: 0.206 ± 0.016 μm, σ_g: 1.552 ± 0.045; Table 6.2) allowing, together with the aforementioned validation of m, to accurately estimate the profiles of optical properties using the Mie theory.

The third step was to consider the calculated optical properties along vertical profiles. The calculated SSA (0.857 ± 0.013 at 441 nm, 0.846 ± 0.011 at 675 nm and 0.812 ± 0.012 at 880 nm) was found to be +8.0 ± 1.2% higher than the one derived from AERONET Ispra (0.812 ± 0.028 at 441 nm, 0.778 ± 0.028 at 675 nm and 0.740 ± 0.034 at 870 nm), similarly for the aerosol optical depth (AOD; Table 6.2). The absorption optical depth (AOD_{Abs}; Table 6.2) was instead very close to the AERONET Ispra values. The values of SSA, AOD and AOD_{Abs} are consistent with the slight overestimation of the real part of the refractive index.

Parameter	Atmospheric Column					
	AERONET-Ispra(235m)			PROFILES-Milano(136m)		
	441nm	675nm	870nm	441nm	675nm	880nm
n	1.449	1.468	1.482	1.511	1.510	1.501
	($\pm$0.009)	($\pm$0.010)	($\pm$0.010)	($\pm$0.006)	($\pm$0.006)	($\pm$0.006)
k	0.010	0.010	0.011	0.011	0.011	0.011
	($\pm$0.004)	($\pm$0.005)	($\pm$0.005)	($\pm$0.001)	($\pm$0.001)	($\pm$0.001)
SSA	0.950	0.947	0.941	0.955	0.932	0.897
	($\pm$0.018)	($\pm$0.020)	($\pm$0.023)	($\pm$0.002)	($\pm$0.003)	($\pm$0.004)
AOD	0.036	0.022	0.015	0.039	0.014	0.006
	($\pm$0.004)	($\pm$0.002)	($\pm$0.001)	($\pm$0.002)	($\pm$0.001)	($\pm$0.001)
AOD_{Abs}	0.002	0.001	0.001	0.002	0.001	0.001
	($\pm 5\times 10^{-4}$)	($\pm 4\times 10^{-4}$)	($\pm 3\times 10^{-4}$)	($\pm 6\times 10^{-5}$)	($\pm 4\times 10^{-5}$)	($\pm 3\times 10^{-5}$)
$D_g(\mu m)$	0.269	0.269	0.269	0.299	0.299	0.299
	($\pm$0.011)	($\pm$0.011)	($\pm$0.011)	($\pm$0.001)	($\pm$0.001)	($\pm$0.001)
σ_g	1.637	1.637	1.637	1.111	1.111	1.111
	($\pm$0.024)	($\pm$0.024)	($\pm$0.024)	($\pm$0.001)	($\pm$0.001)	($\pm$0.001)

Table 6.3: Comparison of the Free Troposphere optical and size distribution properties of the aerosol derived from OPAC continental average data and over AERONET-Davos site. n and k are the real and imaginary part of the complex refractive index. SSA is the Single Scattering Albedo. AOD and AOD_{Abs} are the Aerosol Optical Depth and the Absorption Aerosol Optical Depth, respectively. D_g and σ_g are the geometric mean diameter and the geometric standard deviation, respectively.

From the wavelength dependence of AOD and AOD_{Abs} the corresponding columnar Ångström exponents were calculated: 1.56 and 1.24; they were close to the AERONET Ispra estimation: 1.49 $\pm$ 0.12 and 1.02 $\pm$ 0.07. As a further step, the phase function $P(\theta)$ was also validated (as it is required for the aerosol DRE calculation; Sect. 2.4) by comparing it with that estimated by AERONET Ispra. Figure 6.6a shows this comparison for $\lambda = 675$ nm; furthermore, a high cor-

relation was found at all the wavelengths ($R^2 = 0.988$). Finally, the FT properties were also investigated comparing data above 1 km (derived as reported in Sect. 2.2.2), with AERONET Davos data. Table 6.3 resumes the results of this comparison underlying that the FT properties were in agreement with the AERONET Davos measurements, especially for what concern the AODAbs; the small differences encountered for other parameters (i.e., a slight overestimation of n: $+2.8 \pm 0.9$ %) were considered negligible. In conclusion, after this comparison, the MI data were considered reliable as they were in good agreement with the columnar AERONET Ispra and Davos data. This result is very important as it validated the procedure used for the optical properties calculation (Sect. 2.3) allowing its application also along the vertical profiles measured over TR and ME as well.

Profile validation (comparison with Aethalometer data)

In the previous section, a good agreement between the calculated optical properties and the properties measured by the AERONET network was evidenced.

However, in order to calculate the aerosol DRE at high spatial resolution along vertical profiles (Sect. 2.4) not only a right estimation of the columnar-averaged parameters, but also a correct shaping of them along vertical profiles is needed in order to avoid the presence of compensatory effects along the profiles.

For this purpose, the babs measured by the micro- Aeth®AE51 at 880 nm was compared along vertical profiles with that calculated over TR, MI and ME for the same wavelength (Fig. 6.6b); results showed an excellent agreement ($b_{abs-Mie} = 1.001 \times b_{abs-AE51}$- 0.157, $R^2 = 0.996$, RMSE=0.87Mm^{-1}) validating the Mie calculation of the b_{abs} vertical profiles.

Moreover, measurements performed close to the ground by the micro-Aeth®AE51 at 880 nm in ME were compared with that carried out at ground with the 7-λ Aethalometer AE31 (Sect. 2.2). Only AE31 data that were timely coincident with balloon profiles were considered. The averaged BC and b_{abs} measured by the AE51 were 2.75 ± 0.38 μg m^{-3} and 16.8 ± 2.3Mm^{-1} in keeping with the AE31 data:
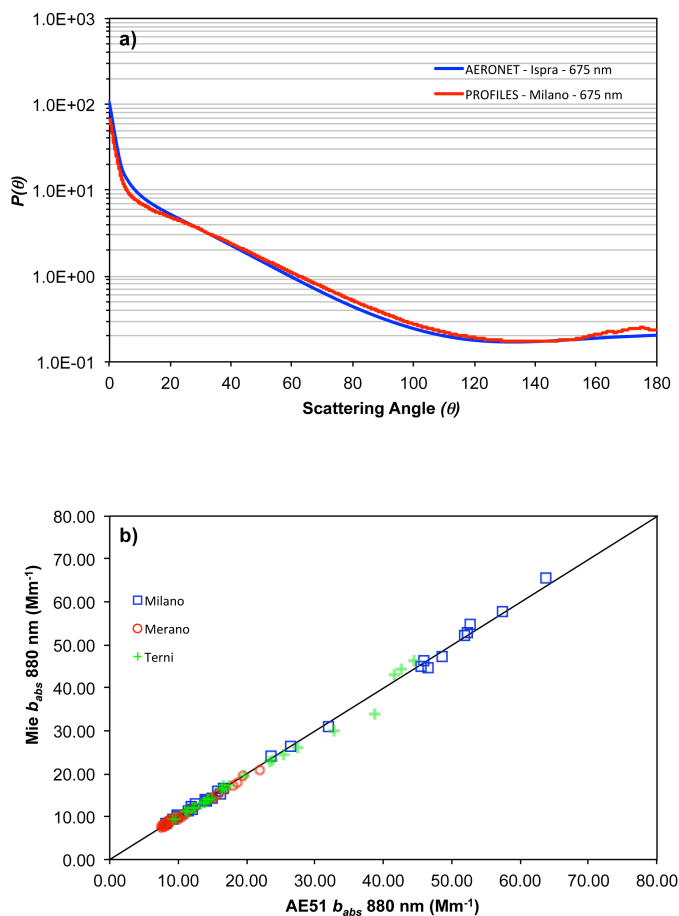
Figure 6.6: (a) Aerosol phase function (P(θ)) along the atmospheric column over MI and the one obtained at AERONET Ispra; (b) linear correlation between the b_{abs} determined from Mie calculations and the one measured by the micro-Aeth®AE51 along vertical profiles for TR, MI and ME (the 1 : 1 black line is also plotted).

2.74 ± 0.10 μg m^{-3} and 18.7 ± 0.7Mm^{-1}, respectively. Moreover, the 7-λ AE31 Aethalometer allowed the comparison of the ground-level absorption Ångström exponent (1.43 ± 0.03) with that obtained by Mie calculation: 1.36 ± 0.01.

These results conclude the validation procedure allowing discussing the behavior of both the aerosol optical properties (Sect. 3.3) and of the DRE profiles (Sect. 3.4) over the three sites.

6.4.3 Vertical profiles of aerosol optical properties

The vertical behavior of aerosol optical properties was similar for all the investigated wavelengths; thus, in this section, we report and discuss results at 675 nm,

which represent the central wavelength with respect to the wavelength range used for the DRE calculation (Sect. 2.4). In this respect, Fig. 6.7 shows the vertical profiles of the aerosol optical properties (at 675 nm) over TR, MI and ME; from this figure, it is possible to observe first the analogy with Fig. 6.4, where vertical profiles of BC and aerosol concentration are reported. Thus, the observed behavior of optical properties is here discussed addressing the vertical changes of the aerosol physicochemical properties reported in Sect. 3.1.
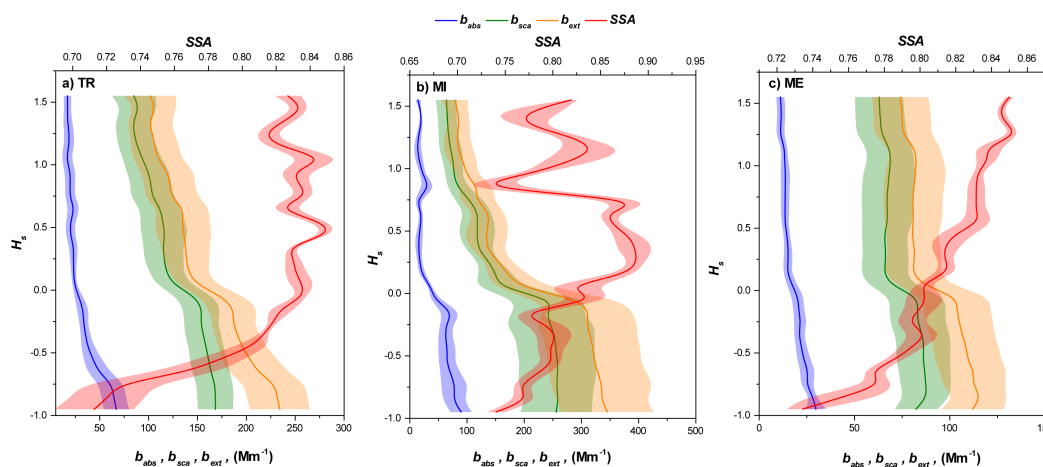
Figure 6.7: Vertical profiles of aerosol optical properties (b_{abs}, b_{sca}, b_{ext} and SSA) at 675 nm over (a) TR, (b) MI and (c) ME.

The most evident behavior of aerosol optical properties is related to the observed changes across the MH (Hs = 0), where b_{sca} and b_{abs} decreased strongly going from BMH to AMH. On average b_{sca} and b_{abs} decreased (from BMH to AMH) over TR by -43.1 ± 3.0% (from 157.6 ± 2.3 to 89.7 ± 4.5Mm^{-1} for b_{sca}) and by -58.8 ± 4.5% (from 45.3 ± 4.6 to 18.7 ± 0.7Mm^{-1} for b_{abs}). Over MI their decrease was of -61.2 ± 3.1% (from 253.3 ± 2.0 to 98.2 ± 7.7Mm^{-1} for b_{sca}) and of -71.3 ± 3.0%(from 69.0 v 4.0 to 19.8 ± 1.7Mm^{-1} for b_{abs}) while over ME the decrease was of -23.5 ± 0.8% (from 85.1 ± 0.7 to 65.1 ± 0.4Mm^{-1} for b_{sca}) and of -47.6 ± 2.5% (from 23.8 ± 1.0 to 12.4 ± 0.2 Mm^{-1} for b_{abs}). Thus, in the lower troposphere the MH becomes also crucial not only to understand the aerosol pollution, but also to shape the vertical behavior of the aerosol optical properties

(Sect. 3.1.1 and Fig. 6.4). In this respect, the most important result that can be observed from the previous findings is the higher (percentage) decrease of b_{abs} across the MH than that of b_{sca}. As a consequence, the SSA increased along height (from BMH to AMH) over the three sites by $+5.7 \pm 2.0\%$ over TR (from 0.781 $\pm$ 0.014 to 0.825 $\pm$ 0.004), $+4.9 \pm 2.2\%$ over MI (from 0.787 $\pm$ 0.010 to 0.826 $\pm$ 0.014) and by $+7.4 \pm 1.0\%$ over ME (from 0.783 $\pm$ 0.007 to 0.840 $\pm$ 0.002). The SSA increase with height, across the MH, is of a great importance as, first, it appears as a general behavior over the three investigated sites and, second, this behavior affects the aerosol DRE and the heating rate as it will be discussed in Sect. 3.4. This result is in agreement with the decrease of the aerosol BC content over the three sites, as highlighted in Sect. 3.1.1, Figs. 6.4 and 6.5, where it was evidenced that AMH the BC aerosol fraction decreased and a corresponding increase in scattering species (i.e., ionic compounds) was present.

Figure 6.7 also highlighted that, BMH, the highest values of b_{sca} and b_{abs} were observed in MI, followed by TR and then by ME, thus reflecting the pollution level over the three sites as described in Sect. 3.1.1. Moreover, the highest values of b_{abs} were found close to the ground (within the first 50-100 m), as happened for BC (compare Fig. 6.4), resulting in an average increase of $+44.9\%$ over TR, of $+19.8\%$ over MI and of $+21.9\%$ over ME, compared to the average b_{abs} values found BMH. On the contrary, a similar behavior of b_{sca} was not observed. Consequently, the SSA reached its minimum value close to ground decreasing (compared to the average found BMH) of -8.2% over TR, of -3.8% over MI and of -4.7% over ME. This behavior increased again the heating-rate effect of aerosol in proximity of the ground (Sect. 3.4). The influence of the aerosol physicochemical properties on the optical ones was also highlighted by the coefficients of variation of BC, aerosol concentration, b_{abs}, b_{sca} and b_{ext} (resumed in Table S1 in the Supplement to Ferrero et al. (2014)) that showed a good agreement among themselves for both BMH and AMH data. Finally, as the DRE calculations (Sect. 2.4) require the FT aerosol

optical properties as input data (the FT validation has been already discussed in Sect. 3.2.1; Table 6.3), we report here their values. b_{sca} and b_{abs} were 1.9 ± 0.9 and $0.2 \pm 0.1 \mathrm{Mm}^{-1}$, respectively; the FT SSA was 0.932 ± 0.003, higher than the values AMH. This observation, expected due to the decreasing BC content with height, highlighted again that the most absorptive aerosol was located in the lower atmospheric layers, BMH and close to the ground.

6.4.4 DRE and heating rate profiles

As illustrated in the previous section, the aerosol optical properties drastically changed along height over the three sites. They were used as input to calculate the vertical profiles of the instantaneous aerosol DRE over TR, MI and ME at noon (Sect. 2.4).

The vertical profiles of aerosol DRE are reported in Fig. S1 in the Supplement to Ferrero et al. (2014). They showed the high level of the dimming effect induced by the aerosol at the surface: the highest DRE was observed over MI (-69.3 $\pm$ 8.8 Wm^{-2}) followed by TR (-54.4 $\pm$ 7.7 Wm^{-2}) and by ME (-40.7 $\pm$ 3.7 Wm^{-2}). Results were in keeping with the aerosol and BC concentrations, and with the optical properties reported in Figs. 6.4 and in 6.7, respectively. At the top of atmosphere, the DRE was similar among the three sites: -5.6 $\pm$ 0.7 Wm^{-2} (MI), -6.3 $\pm$ 0.3 Wm^{-2} (TR) and -6.1 $\pm$ 0.6 Wm^{-2} (ME). The aforementioned data were in keeping with values reported in literature (Perrone and Bergamo, 2011; Saha et al., 2008; Chakrabarty et al., 2012). These data indicated a net columnar cooling effect of the aerosol on the Earth-atmospheric system. However, the difference between the DRE at the top and the bottom of the atmosphere indicated that a significant amount of energy was absorbed into the atmosphere thus heating it.

In order to quantify this phenomenon, the difference between the DRE at the top and the bottom of each atmospheric layer (ΔDRE_{ATM}) was first calculated using Eq. (13) (Sect. 2.4) for each site and broad-range altitude layers: BMH

(from ground to MH), AMH (from MH to 1 km), FT ($>$ 1 km) (compare Sect. 2.2.2). Results are reported in Fig. 6.8a; they highlighted a generally high level of atmospheric absorption both BMH (ΔDRE_{ATM}: 11.9 $\pm$ 1.6, 28.1 $\pm$ 4.4 and 7.8 $\pm$ 0.9 Wm^{-2} over TR, MI and ME) and AMH (ΔDRE_{ATM}: 27.7 $\pm$ 6.1, 26.4 $\pm$ 4.5 and 18.2 $\pm$ 2.8 Wm^{-2} over TR, MI and ME) compared to the FT (ΔDRE_{ATM}: 8.5 $\pm$ 0.3, 9.2 $\pm$ 0.7 and 8.6 $\pm$ 0.6 Wm^{-2} over TR, MI and ME). As a result, the atmospheric absorption took place mainly within the first km of the atmosphere (BMH+AMH), with a percentage (compared to the whole atmosphere) of 82.4, 85.5 and 75.1% over TR, MI and ME, respectively; the high aerosol pollution level below and strictly above the MH (Sect. 3.1) was responsible of this macroscopic behavior.
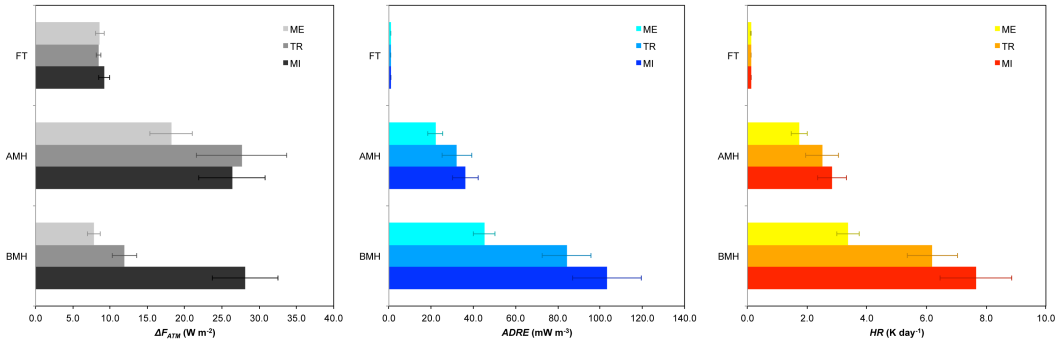
Figure 6.8: ΔDRE_{ATM} (a), $ADRE$ (b) and HR (c) calculated for each site and broad-range altitude layers: BMH (from ground to MH), AMH (from MH to 1 km) and FT ($>$ 1 km).

However, as stated in Sect. 2.4, ΔDRE_{ATM} quantifies the integrated radiative power density absorbed by the aerosol within each atmospheric layer. Therefore, the aforementioned ΔDRE_{ATM} data did not allow comparing the atmospheric absorption both among the three sites and, within each site, along the atmospheric column. The main reasons are the different MH found over TR, MI and ME (142 $\pm$ 22, 272 $\pm$ 50 and 173 $\pm$ 42 m, respectively; Sect. 3.1.1) and the broader altitude range of the FT compared to the BMH and AMH layers.

Thus, in order to describe and compare the vertical behavior of atmospheric absorption in different situations, the absorptive DRE (ADRE, Sect. 2.4) was

calculated accordingly to Eq. (14) normalizing ΔDRE_{ATM} by the thickness of each layer; since the wintertime aerosol absorption was mainly due to the presence of BC, the ADRE represented, in first approximation, the atmospheric DRE induced by BC.

ADRE values for each site and broad-range altitude layers (BMH, AMH and FT) are reported in Fig. 6.8. By excluding the effect of the layer thickness, it is now possible to realize that the most intense atmospheric absorption was observed BMH, particularly over MI (103.3 ± 16.2 mWm^{-3}) followed by TR (84.3 ± 11.5 mWm^{-3}) and by ME (45.2 ± 5.1 mWm^{-3})); the same order was observed considering AMH data: higher values were found over MI (36.2 ± 6.2 mWm^{-3})) followed by TR (32.2 ± 7.1 mWm^{-3})) and ME (22.0 ± 3.4 mWm^{-3}). Finally, the FT experienced the lower absorption: 0.9 ± 0.1 mWm^{-3} over the three sites.

Interestingly, these data evidenced an average decrease of ADRE across the MH of $-64.9 \pm 0.6\%$ over MI, of $-61.8 \pm 3.2\%$ over TR and of $-51.3 \pm 2.0\%$ over ME, in keeping with the vertical behavior of both BC and b_{abs} (Sects. 3.1.1 and 3.3). Also the continuous ADRE vertical profiles (Fig. 6.9) are in agreement with data shown in Figs. 6.4 and 6.7. Thus, despite the absolute values, a common feature occurred over MI, TR, and ME as a sharp decrease of the ADRE was observed at the MH (Hs = 0). Most of the ADRE occurred within the mixing layer, in agreement with the BC pollution loading in basin valleys, especially over the most urbanized and industrialized sites of MI and TR.

This behavior has an important feature, as the ADRE induces an instantaneous HR that was computed following Eq. (16) (Sect. 2.4). The calculated HR values are reported in Fig. 6.8c (for BMH, AMH and FT). The highest degree of instantaneous heating rate was observed BMH: 7.7 ± 1.2 K day^{-1} over MI, 6.2 ± 0.8 K day^{-1} over TR and 3.4 ± 0.4 K day^{-1} over ME. Above the MH values were lower, but the same order was observed: higher values were found over MI (2.8 ± 0.5 K day^{-1}) followed by TR (2.5 ± 0.5 K day^{-1}) and by ME (1.7 ± 0.3 K day^{-1}). Finally, in the FT the HR was the lowest over the three sites: $0.1 \pm$

1×10^{-2} K day^{-1}. These results are very important, as in literature vertical profiles of HR are few and usually only the average columnar HR is estimated. For example, Chakrabarty et al. (2012) estimated a columnar average HR of $\sim$2 K day^{-1} considering a Δp of 300 hPa; as a comparison, using the same approach over TR, MI and ME, the average columnar HR was $\sim$1-2 K day^{-1} in agreement with that study. However, the estimation of the average columnar HR could be misleading as it does not give any information regarding where the HR is located and which feedbacks can trigger.
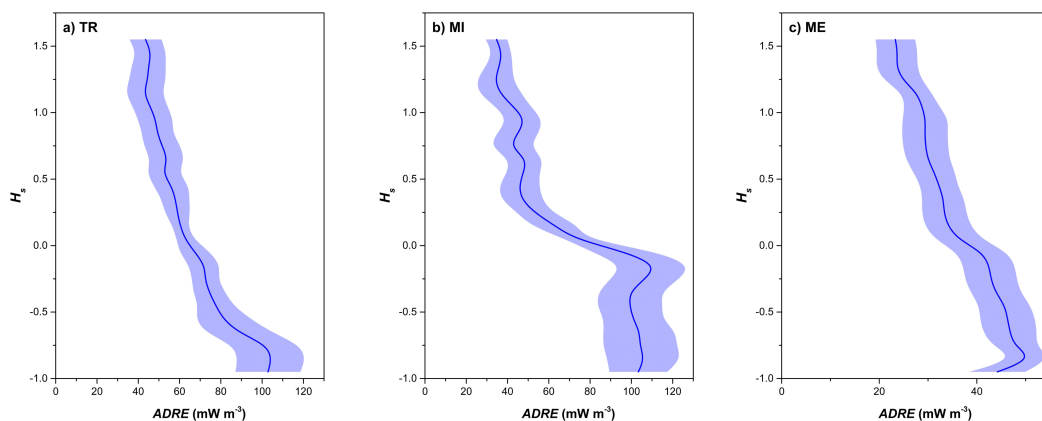
Figure 6.9: Continuous vertical profiles of ADRE over TR (a), MI (b) and ME (c).

In the present work, due to the high vertical resolution of balloon soundings, a step forward can be done as the heating dynamics across the MH was well characterized. In this respect, continuous HR profiles are reported in Fig. 6.10 and showed (together with Fig. 6.8c) that most of the HR occurred within the mixing layer and that a strong vertical gradient was present at the MH, in agreement with ADRE (Figs. 6.8b and 6.9). This happened over TR, MI and ME, pointing towards a common behavior over basin valleys, where stagnant atmospheric conditions are present (Sect. 3.1.1 and Fig. 6.2).

As the vertical behavior of the HR can trigger different feedbacks able to promote the aerosol semi-direct effect, it is interesting to note (Fig. 6.10) that the highest HR values were observed BMH and that they could turn into a weakening

of the ground-based thermal inversion, which are common in basin valleys (Ferrero et al., 2012).

Consequently, it would be helpful to "describe" the vertical behavior of the HR in terms of the potential feedbacks that it could promote using a simple parameter. Here we propose the use of the heating rate vertical gradient (K day^{-1} km^{-1}) as a proxy of the feedback potential (HERFPO: heating rate feedback potential). The HERFPO represents the atmospheric thermal lapse rate that would take place if the forcing induced by the instantaneous HR profile would last all day.
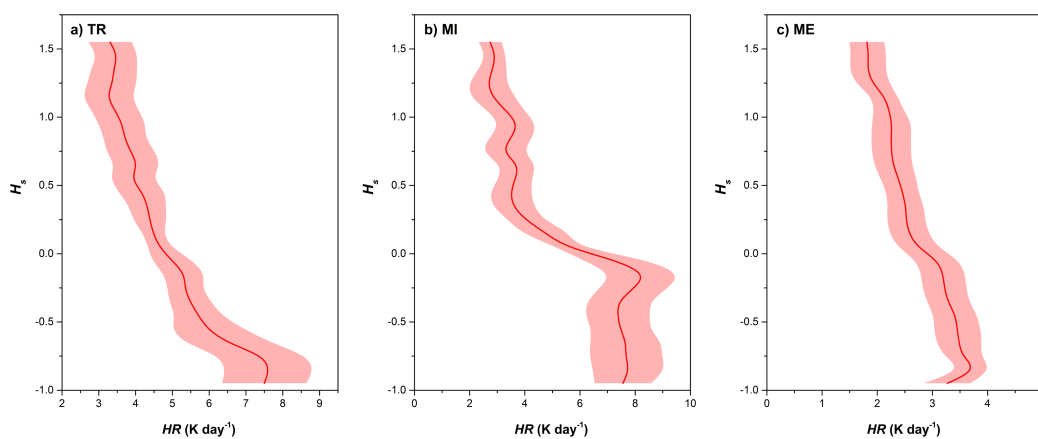
Figure 6.10: Continuous vertical profiles of HR over TR (a), MI (b) and ME (c).

Thus, the HERFPO was calculated along the HR profiles (from the bottom to the top) over each measuring site obtaining the following values: -8.3 ± 1.2 K day^{-1} km^{-1} over MI, -6.1 ± 0.5 K day^{-1} km^{-1} over TR and -2.6 ± 0.2 K day^{-1} km^{-1} over ME.

The comparison of these data with the atmospheric dry adiabatic lapse rate (-10 K km^{-1}) suggested that the vertical HR had really the potential to result in a negative feedback promoting an increase of the atmospheric dispersal conditions, by weakening the ground-based thermal inversions, especially over MI and TR. However, it is of great importance to consider that HERFPO refers only the to the behavior of the atmosphere. Hence, in order to fully understand the feedback induced by the aerosol and BC on the atmospheric turbulence, the energy fluxes

between ground and the atmosphere have also to be considered. In this respect, the high level of dimming induced by aerosol at the surface (as shown at the beginning of this section) could balance the atmospheric effect of HERFPO.

In conclusion, in the context of future applications of this concept and of the aforementioned results, the role of each parameter in determining atmospheric feedbacks, as well as their net effect, has to be considered and investigated.

6.5 Conclusions

Vertical profiles of BC and aerosol number-size distribution were measured over three Italian basin valleys (Terni Valley, Po Valley and Passiria valleys) allowing the characterization of the aerosol and BC dispersion under similar orographic conditions. Changes of BC concentrations and of aerosol BC fraction as a function of the height were related with variations of aerosol optical properties, radiative forcing and heating rate.

Measurements were conducted during three week-long wintertime campaigns. The aerosol vertical profiles have been determined by means of a tethered balloon-based moving platform (fitted with a micro-Aethalometer, an OPC, a cascade impactor and a meteorological station) while the aerosol chemical composition was determined analyzing $PM_{2.5}$ samples collected at different heights.

Results from the measured vertical profiles allowed to clearly identify the mixing height (MH), which was characterized by a strong vertical concentration gradient of both BC (range: from -48.4 $\pm$ 5.3 to -69.1 $\pm$ 5.5%) and aerosol (range: form -23.9 $\pm$ 4.3 to -46.5 $\pm$ 7.3%). Above the MH, not only the BC concentration, but also its aerosol fraction decreased (range: from -33.2 $\pm$ 4.9 to -47.5 $\pm$ 7.9%) while a shallow BC layer of higher concentrations (range: from +16.1 to +34.2%) was found close to the ground, in the first 50-100m of the atmosphere, due to the proximity of BC sources.

These behaviors caused important changes of the optical properties of the aerosol (b_{abs}, b_{sca}, b_{ext}, SSA) at different heights that were quantified applying Mie theory to aerosol data. Before this step, the aerosol refractive index was calculated using the effective medium approximation applied to aerosol chemical composition and the OPC number-size distribution was corrected for the ambient aerosol refractive index and log-normally interpolated. Results were validated with AERONET data and evidenced an increase of the single-scattering albedo with height (range: from $+4.9 \pm 2.2$ to $+7.4 \pm 1.0\%$).

The effect of optical properties changes with height was assessed using a radiative transfer model (libRadtran) from which vertical profiles of direct aerosol radiative forcing, atmospheric absorption and heating rate were calculated. atmosphere along continuous vertical profiles, a new parameter, the absorptive direct radiative effect (ADRE) was developed normalizing the radiative power density absorbed into each atmospheric layer by the layer height. The highest atmospheric absorption (ADRE) was observed below the mixing height (range: from $+45.2 \pm 5.1$ to $+103.3 \pm 16.2$ mW m^{-3}) influencing the heating-rate profile. Hence, the heating rate vertical gradient (K day^{-1} km^{-1}) was investigated allowing to estimate the heating rate feedback potential (HERFPO). The HERFPO ranged from -2.6 $\pm$ 0.2 to -8.3 $\pm$ 1.2 K day^{-1} km^{-1}. Thus, the behavior of BC loaded below the MH promoted a negative feedback favorable to the increase of the atmospheric dispersal conditions.

The obtained results were similar over the three sites and pointed towards a common aerosol dynamics over basin valleys characterized by comparable atmospheric stagnant conditions. These data represent the first high-resolution vertical profile of aerosol radiative forcing and heating rate obtained over Italy and Europe and allowed to describe with a great vertical detail the radiative forcing induced by BC (and aerosol) in the lower troposphere, across the mixing layer and within it, where the anthroposphere is located.

Chapter 7

Remote sensing of solar radiation

7.1 Basics of satellite remote sensing

The use of sensors on satellite platforms offers one way for monitoring many geo-physical parameters at the Earth's surface and in the atmosphere. Satellite remote sensing has advantages and disadvantages compared to ground-based observations (Table 7.1).

Advantages	Disadvantages
Global coverage, including remote areas and oceans	Indirect measurement of atmospheric and surface parameters
High time resolution	Low spatial resolution
Synchronous measurement of many parameters	Computational effort for processing large amount of data

Table 7.1: Advantages and disadvantages of satellite remote sensing compared to ground based measurements.

Before describing remote sensing of solar radiation, it is impotant to have a clear idea of the geometry of satellite aquisitions, and thus to understand the physical laws governing satellite motion. These are referred to as Kepler's laws, which apply to any orbit around the Sun.

125

The only force acting on a satellite is gravity, which is central and conservative, thus the total mechanical energy E is conserved. Gravity acts along the line between the satellite and the Earth, so the total angular momentum L of the system about the origin is conserved. The trajectory is determined by the values of E and L.

The kinetic energy of the satellite can be expressed as the sum of two components:

$$K = \frac{1}{2}mv_r^2 + \frac{1}{2}mv_t^2 \tag{7.1}$$

where m is the mass of the satellite, and v_r and v_t are respectively the radial and tangential component of the velocity of the satellite v, with v_r parallel and v_t perpendicular to the position vector of the satellite:

$$v = v_t + v_r. \tag{7.2}$$

The magnitude of the angular momentum of the satellite is:

$$L = mrv_t \tag{7.3}$$

where r is the distance between the satellite and the Earth, thus:

$$K = \frac{1}{2}mv_r^2 + \frac{L^2}{2mr^2} \tag{7.4}$$

Adding the potential energy, we get the total energy:

$$E = \frac{1}{2}mv_r^2 + \frac{L^2}{2mr^2} - G\frac{Mm}{r} \tag{7.5}$$

Equation 7.5 is formally one-dimensional, because the only variables are the speed along the radial line between the Earth and the satellite and their distance along that line. Thus we can simply obtain the turning points in the radial motion, which will give us the distances of closest approach and furthest recession of the

satellite. At this points the velocity component v_r is zero. We can define an effective potential energy, U_{eff}, as:

$$U_{eff} = \frac{L^2}{2mr^2} - G\frac{Mm}{r} \tag{7.6}$$

thus:

$$E = \frac{1}{2}mv_r^2 + U_{eff} \tag{7.7}$$

Turning points in the radial motion are those at which E is equal to U_{eff}. From Equation 7.6 we see that for increasing r, U_{eff} approaches zero. This means that if E is positive or zero there is no turning points for large r values, and the motion in unbound. But if E is negative, there are two turning points and the orbit is bound and is an ellipse, with M at one focus (Kepler 1st law). The names of the turning points are perigee and apogee, since they are the points of minimum and maximum distance between the Earth and the satellite. Their distances from the Earth, r_a and r_p, can be found by setting $U_{eff} = E$.

$$\frac{L^2}{2mr^2} - G\frac{Mm}{r} = E \tag{7.8}$$

thus:

$$r^2 + \frac{GMm}{E}r - \frac{L^2}{2mE} = 0 \tag{7.9}$$

The roots of this equation are r_a and r_p, so according to Vieta's formula it must be:

$$r_a + r_b = -\frac{GMm}{E} \tag{7.10}$$

$$r_a r_b = -\frac{L^2}{2mE} \tag{7.11}$$

The relations between r_a and r_p and the axes of the ellipse, a and b, are the following:

$$r_a + r_b = 2a \tag{7.12}$$

$$r_a r_b = b^2 \tag{7.13}$$

so we can obtain the following expressions for E and L:

$$E = -\frac{GMm}{2a} \tag{7.14}$$

$$L^2 = -2mEb^2 \tag{7.15}$$

Equation 7.14 means that the total energy E depends only on the orbit length, a, and Equation 7.15 shows that L is proportional to b, so it is lower for orbits having high eccentricity.

Let's consider the position of the satellite at two times, t and $t + dt$. The satellites moves of a distance ds along the orbit, and the radius connecting it to the Earth turns of an angle $d\theta$. The area:

$$dA = \frac{1}{1}rds = \frac{1}{2}r^2 d\theta \tag{7.16}$$

is swept by the radius at a rate:

$$\frac{dA}{dt} = \frac{1}{2}r^2 d\frac{\theta}{dt} = \frac{1}{2}r^2 \boldsymbol{\omega} \tag{7.17}$$

where $\boldsymbol{\omega}$ is the angular velocity. Since $r\boldsymbol{\omega} = v$ and $mr^2\boldsymbol{\omega} = L$, we find:

$$\frac{dA}{dt} = L\frac{L}{2m} \tag{7.18}$$

Since L is constant, Equation 7.18 shows that the rate at which the area is swept out by the line joining the satellite and the Earth is constant (Kepler 2nd law). Integrating dA over the period T (the time for a complete revolution), we obtain the area of the ellipse:

$$A = \frac{LT}{2m} \tag{7.19}$$

Since the area of an ellipse is πab, we find Kepler 3rd law:

$$\frac{a^3}{T^2} = \frac{GM}{4\pi^2} \tag{7.20}$$

showing that the square of the period of any satellite is proportional to the cube of the semi-major axis of its orbit.

According to Kepler laws, two main types of satellite orbit can be identified, i.e. geostationary orbit ans polar orbit.

A geostationary orbit is a circular orbit above the equator in which the satellite rotates in the same direction and with the same rotational period as the Earth. Consequently an observer on the Earth's surface sees the satellite as fixed in the sky, and the satellite always views the same area on the Earth's surface. From Kepler 3rd law applied to a circular orbit $(a=r)$ we can derive the height of a geostationary orbit:

$$r = \sqrt[3]{\frac{T^2 GM}{4\pi^2}} \tag{7.21}$$

Substituting:

$$G = 6.61 \times 10^{-11} \, m^3 kg^{-1} s{-}2$$

$$T = 86160 \, s$$

$$M = 5.97 \times 10^{24} \, kg$$

we get an orbit radius $r \approx 42155$ km. In terms of height above surface, h, if we subtract from r the Earth's radius $R \approx 6378$ km, we get:

$$h = r - R \approx 35785 \, km \tag{7.22}$$

A polar orbit is one in which the satellite passes above or nearly above both poles of the Earth on each revolution. It therefore has an inclination of around

90 degrees to the equator. Polar orbiting satellites orbit at an height above the Earth's surface between 100 km and 200 km, taking around 90 min to cover each orbit. A satellite in a polar orbit will pass over the equator at a different longitude on each of its orbits.

7.2 Meteosat geostationary satellites

Meteosat is the European meteorological program in geostationary orbit that was initiated in 1972 by ESRO (European Space Research Organization). ESRO was founded in 1962 and was the predecessor organization to ESA (European Space Agency) which was founded in 1975.

Meteosat-1 was the first European meteorological geostationary satellite, launched on November 23, 1977 (MFG, www). The mission failed in 1979, but in 1981 and 1988 Meteosat-2 and Meteosat-3 were launched. The main objective of the Meteosat system was the provision of cost-effective satellite data and products on a continuous basis. The data were mainly focused on the needs of operational meteorology and supported especially operational weather forecasting. The geographical coverage region of the Meteosat satellites was most of Europe, the whole of Africa, the Atlantic Ocean and the eastern part of South America, and the Middle East

In 1986 the EUMETSAT (European Organisation for the Exploitation of Meteorological Satellites) convention was signed by 16 countries. EUMETSAT operates and owns Meteosat satellites starting from Meteosat-4.

The primary observation payload of the 1st generation of Meteosat satellites was MVIRI (Meteosat Visible and Infrared Imager), consisting of a high-resolution 3-band radiometer, providing images every half hour in the visible range (VIS), thermal infrared region (TIR), and in the water vapor absorption bands (WV). The ground pixel size (at nadir) was of 2.5 km x 2.5 km for the VIS band and of 5 km x 5 km for the other two.

The first generation Meteosat series (MFG, Meteosat-1 to -7) was gradually replaced by a second generation series (MSG). The first satellite MSG-1 was launched on August 28, 2002, and was followed by three more satellites, ensuring operational continuity for at least 16 years (Met, www). MSG-1 became Meteosat-8 in 2004 when the mission was declared operational, i.e. when routine operations started after the commissioning phase.
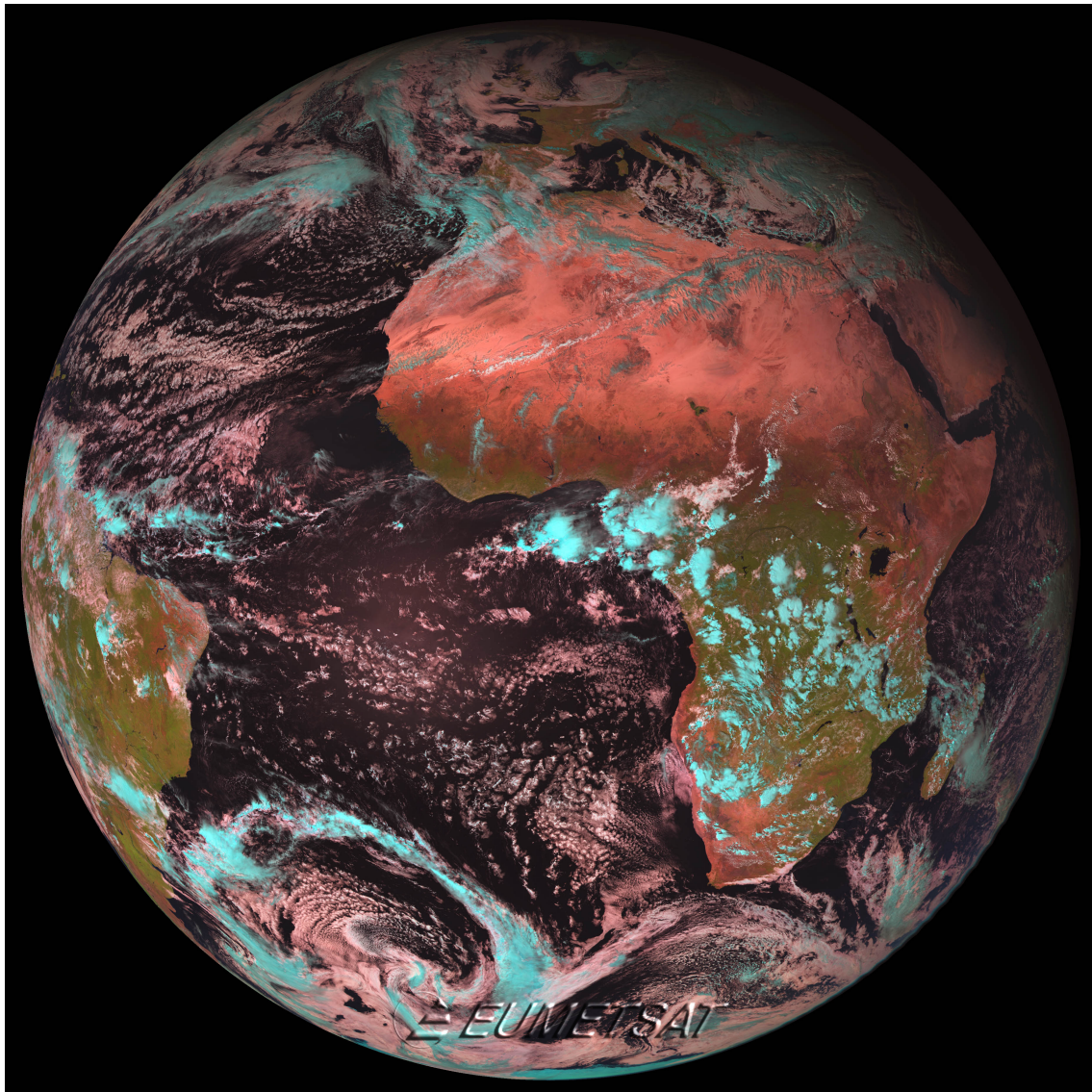
Figure 7.1: First natural-color RGB image of the Earth acquired by the MSG-2 satellite on 25 January 2006. Low clouds are white, vegetation is green, deserts are reddish brown, and snow cover and high ice clouds are cyan.

MSG is designed to support nowcasting, short range forecasting, numerical

weather forecasting and climate applications over Europe and Africa. It offers multispectral imaging of clouds, the Earth surface and radiance emitted by the atmosphere, with improved radiometric, spectral, spatial and temporal resolution as compared to the first generation Meteosat.

Te main payload of MSG is SEVIRI (Spinning Enhanced Visible and Infrared Imager), with 4 VIS/NIR channels (0.4-1.6 μm) and 8 IR channels (3.9-13.4 μm), and a resolution at nadir of 1 km for the high-resolution visible channel and 3 km for the IR and the 3 other VIS channels. It produces one image every 15 min. Figure 7.2 shows the first color image of the Earth acquired by SEVIRI on board the MSG-2 satellite on 25 January 2006.

Since 2000 EUMETSAT has been working at the definition of a Meteosat Third Generation (MTG) programme (MTG, www). The MTG series will include six satellites, with the first one likely to be ready for launch from 2018. The in orbit configuration will consist of two parallel positioned satellites, the MTG-I imager and the MTG-S sounder. The sounder will be one of the innovations in the new programme, allowing Meteosat satellites to not just image weather systems but to analyse the atmosphere layer-by-layer and perform detailed chemical composition studies.

MTG-I satellites will fly the Flexible Combined Imager (FCI) and an imaging lightning detection instrument the Lightning Imager (LI). The MTG-S will include an interferometer, the InfraRed Sounder (IRS), with hyper-spectral resolution in the thermal spectral domain, and the Sentinel-4 instrument, the high resolution Ultraviolet Visible Near-infrared (UVN) spectrometer.

Methods for deriving solar irradiance at the Earth's surface were developed for MFG and were modified for application to MSG satellite data. In the next sections these algorithms are described, with a special focus on the algorithm HelioMont which was developed for having best performances over mountainous regions and bright surfaces.

7.3   The method HELIOSAT

The algorithm HELIOSAT exploits the high temporal resolution of imagery produced by instruments on board geostationary Meteosat satellites. It was originally proposed by Cano (Cano et al., 1986) for uncalibrated radiances measured by sensors on board Meteosat first generation satellites, and modified by Beyer (Beyer et al., 1996) and Hammer (Hammer et al., 2003).

The basic idea of the first formulation of HELIOSAT is that the amount of cloud cover of an area statistically determines global irradiance on that area. The first step was calculating a reference albedo (ρ_{min}) map for clear-sky conditions, i.e. a map of minimum reflectance, considering that the albedo of the Earth's surface is usually lower than the albedo of clouds. This map was updated daily for each pixel. Then a cloud index, n, was calculated by comparing the radiance measured by the satellite sensor, ρ, with the reference albedo:

$$n = \frac{\rho - \rho_{min}}{\rho max - \rho_{min}} \tag{7.23}$$

where ρ_{max} is the maximum albedo observed in overcast conditions.

The cloud cover index varies from 0 to 1 and represents the percentage of cloud cover of a pixel. A linear relation was assumed between n and an atmospheric transmission factor, K, defined as the ratio between global horizontal irradiance at the Earth's surface and horizontal irradiance at the top of the atmosphere. The coefficients of this relation were derived from ground measurements of global irradiance.

Global irradiance under clear-sky conditions (SIS_{cs}, Surface Incoming Shortwave radiation under clear-sky conditions) was expressed with the simple model proposed by Bourges (1979):

$$SIS_{cs} = G_0 cos(\theta)^{1+a} \tag{7.24}$$

where θ is the sun zenith angle, the subscript cs indicates clear-sky conditions, and a is a parameter characterizing total atmospheric transmittance varying with the coordinates of the location. Finally the all-sky irradiance was calculated as the product of K and SIS_{cs}:

$$SIS = K(n)SIS_{cs} \qquad (7.25)$$

The main limitation of this approach was the dependency of global irradiance on ground measurements for determining the relation between K and n.

In later versions of the algorithm K was substituted by a clearness index, k_{clear}, defined as the ratio between all-sky irradiance and clear-sky irradiance to account for atmospheric transmittance variability with sun zenith angle. Furthermore a new relation between n and k_{clear} was assumed, no more dependent on ground measurements. Finally the clear-sky model was changed, and direct and diffuse irradiance were calculated with empirical models using the Linke turbidity factor to describe atmospheric extinction.

Direct irradiance was derived with the model of Page (1996):

$$DIR_{cs} = e \times S \times exp(-0.8662 T_L m \delta_R(m)) \qquad (7.26)$$

where all variables have been already defined in Chapter 2.

Diffuse irradiance was derived with the formula of (Dumortier, 1995):

$$DIF_{cs} = G_0(0.0065 + (-0.045 + 0.0646 T_L)cos(\theta) + (0.014 - 0.0327 T_L)cos^2(\theta))$$
$$(7.27)$$

A climatological model was applied to consider the inter-annual variability of atmospheric turbidity.

At the end clear-sky global irradiance was calculated as:

$$SIS_{cs} = DIR_{cs}cos(\theta) + DIF_{cs} \qquad (7.28)$$

The fraction of diffuse irradiance was calculated with the statistical model of Skartveit et al. (1998), which exploits the hourly variability of global irradiance.

In 2009 HELIOSAT was modified by Dürr and Zelenka (2009) for application in such a complex terrain like the alpine region by adding to the algorithm image georeferencing, snow-cover detection, identification of clouds above snow and correction of terrain effects. First MSG pixels were classified in cloud-free, cloudy, and snow-covered by combining spectral information of different MSG channels and the spatial and temporal variability of the observed reflectance. Then the cloud index was calculated with a formulation dependent on the pixel classification, which considered that the albedo of snow could be higher that the maximum reference albedo of clouds. Terrain effects correction was based on the Shuttle Radar Topographic Mission (SRTM) 90 m digital elevation model (DEM), which was used for deriving a binary shadow map anf the sky-view factor. Clear-sky irradiance was calculated with the empirical formulation of Kasten (Kasten, 1996), based on the Linke turbidity and modified to consider the effect of altitude. Finally all-sky global irradiance was calculated as:

$$SIS_{cs} = DIR_{cs}cos(\theta) + DIF_{cs} \tag{7.29}$$

The next section describes the last HELIOSAT formulation, HelioMont, in which the empirical clear-sky model is substituted by radiative transfer model calculations.

7.4   The algorithm HelioMont

HelioMont is a processing framework developed by Meteo Swiss for retrieving solar radiation at the Earth's surface from Meteosat Second Generation (MSG) satellite data. The details of the algorithm are described in Stöckli (2013a). On one hand it inherits from HELIOSAT the derivation of the all-sky surface radiation from the

clear-sky surface radiation and the cloud index. On th other hand it differs from HELIOSAT in the clear-sky model, in fact it uses the approach of Müller et al. (2004), which is based on radiative transfer model simulations.

HelioMont empoys the MSG SEVIRI High Resolution Visible (HRV; 0.45-1.1 μm) channel in combination with five other near-infrared and infrared channels (0.6, 0.8, 1.6, 10.8, 12.0 μm). Data from MSG SEVIRI are availabre from 2004 to the present time. While the original HELIOSAT method relied on raw digital data, HelioMont uses calibrated radiances which are generated and distributed by space agencies.

The main time-dependent input for HelioMont consists of MSG Level 1.5 digital numbers (DN), which are sensor counts, every 15 min or 30 min. First the satellite data is adapted to the geographical domain. Second, top-of-atmosphere (TOA) radiances are calculated as a linear function of DN, with slope and aspect parameters wich change in time and are different for each channel. Third, brightness temperatures T_x (for thermal channels) and reflectances ρ_x (for solar channels) are calculated (x is the channel number). Fourth, low-resolution visible (VIS), near-infrared (NIR), water vapor (WV) and infrared (IR) channels are re-gridded by bilinear interpolation to the spatial resolution of the high resolution visible (HRV) channel.
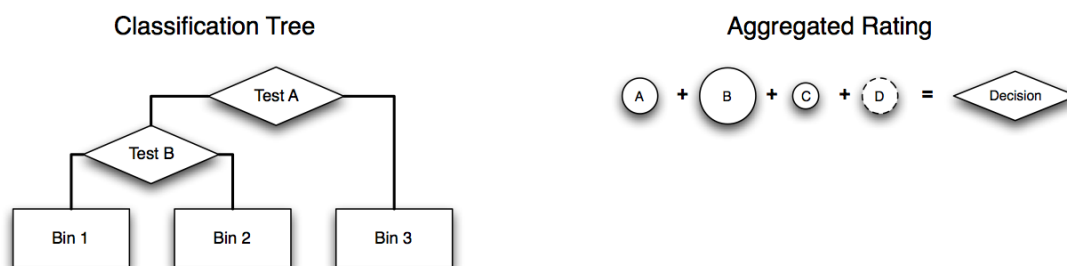
Figure 7.2: The classification tree (left) versus the aggregated rating (right) cloud masking method, from Stöckli (2013b).

7.4.1 Cloud Mask

The cloud mask is derived by the SPARC algorithm (Separation of Pixels using an Aggregated Rating over Canada, by Khlopenkov and Trishchenko (2007)). It was originally developed for the polar orbiting Advanced Very High Resolution (AVHRR) sensor from the National Oceanic and Atmospheric Administration (NOAA), and it is also suitable for SEVIRI sensor data (Fontana et al., 2010).

Most cloud masks use a decision tree classification, in which each step depends on the previous one. SPARC, instead, uses an additive rating scheme, which is more spectrally flexible and works even if the spectral coverage is not complete. See Figure 7.2 for a schematic comparison between the two approaches.

The SPARC algorithm produces an aggregated rating F from the sum of individual scores A, B, C, D etc.,

$$F = A + B + C + (D) + ... \tag{7.30}$$

where each score generates a continuous measure of cloudiness. It is negative for a clear-sky and positive for a cloudy scene. It can happen that one score is positive and another one is negative, resulting in a cloud mask with high uncertainty. This possibility is missing in the decision tree approach.

The SPARC algorithm is very empirical, in fact each score needs to be weighted with two sensor-dependent coefficients, a scale and an offset (see Stöckli (2013b)).

In the following the scores of SPARC applied to MSG are described.

Temperature score, T_{score}

T_{score} compares the brightness temperature of the thermal channel at 10.8 μm with the clear-sky temperature.

$$T_{score} = (T_{10.8} - T_{cf} - T_{offset})T_{scale} \tag{7.31}$$

where T_{cf} is an estimate of the cloud-free brightness temperature, which for MSG is based on the fitting of a diurnal temperature model.

Brightness score, B_{score}

B_{score} operates during daytime and it tests the brightness temperature in the visible channel, ρ, against the backgroun reflectance, ρ_{cf}.

$$B_{score} = (\rho - B_{offset})B_{scale} \tag{7.32}$$

Reflectance score, R_{score}

R_{score} compares the spectral reflectance of different surface types with the one of clouds in the 0.6 μm and 1.6 μm channels.

$$R_{score} = \left[\frac{\rho_{0.6}^2 \rho_{1.6}^2}{1.5\rho_{1.6}^{2.8}(3.0\rho_{1.6} + 0.5\rho_{0.6} + 3.5) + 1.5\rho_{0.6}^2} - R_{offset}^{1.6} \right] R_{scale}^{1.6} \tag{7.33}$$

Simple ratio score, N_{score}

N_{score} is a score assuming limited values which can help the decision when the separation of cloud-free and cloudy pixels is not clear. It tries to identify clouds from NDVI, since it should be around 1, but the same is true for non vegetated soils.

$$N_{score} = \left(\left| \frac{\rho_{0.8}}{\rho_{0.6}} - 1 \right| - N_{offset} \right) N_{scale} \tag{7.34}$$

Spatial texture uniformity score, UR_{score}

UR_{score} detects cloud boundaries from the spatial variancae of the visible reflectance for each pixels. It assumes limited values, because high variance may also correspond to complex terrain or costal lines.

$$UR_{score} = f_w(\sigma_{xy}(\rho_{vis}) - UR_{offset})UR_{scale} \tag{7.35}$$

where f_w is an attenuation function based on the background clear-sky map of the spatial variance derived from the water mask.

Spatial temperature uniformity score, UT_{score}

UT_{score} is similar to UR_{score} but applied to the radiative temperature.

$$UT_{score} = (\sigma_{xy}(T_{10.8}) - UT_{offset})UT_{scale} \tag{7.36}$$

Cirrus score, C_{score}

C_{score} detects thin and hight clouds which cannot be detected from T_{score} and B_{score}.

$$C_{score} = (T_{10.8} - T_{12.0} - C_{offset})C_{scale} \tag{7.37}$$

Temporal temperature uniformity score, TT_{score}

TT_{score} can be applied only to the high temporal resolution geostationary satellite data. It is very effective in detecting clouds from the high temporal variability of the brightness temperature.

$$TT_{score} = (\sigma_t^{2h}(T_{10.8}) - TT_{offset})TT_{scale} \tag{7.38}$$

where σ_t^{2h} is the temporal variance of a pixel over the last 2 hours.

Diurnal temperature uniformity score, DT_{score}

DT_{score} is also only applicable to geostationary satellite data. It discriminates low-level stratiform clouds from the low diurnal variability of their brightness temperature in the channel at 10.8 μm. In fact the main temperature score does not help in identifying these clouds, because they often occurr when there is a strong inversion of the planetary boundary layer, thus they can have a cloud top temperature very similar to surface temperature.

$$DT_{score} = ((5 - \sigma_t^{24h}(T_{10.8}) - DT_{offset})DT_{scale} \tag{7.39}$$

NDSI score, S_{score}

S_{score} is based on the Normalized Difference Snow Index, NDSI, which is a well-known empirical snow detection method.

$$S_{score} = \left(\frac{\rho_{0.6} - \rho_{1.6}}{\rho_{0.6} + \rho_{1.6}} - S_{offset} \right) S_{scale} \tag{7.40}$$

Freeze score, F_{score}

F_{score} is another test which helps snow detection.

$$F_{score} = \left(- \left| T_{10.8} - T_f + 2 \right| - F_{offset} \right) F_{scale} \tag{7.41}$$

where T_f is the seasonally oscillating maximum radiative surface temperature for snow cover.

Snow detection, $snow_{score}$

$snow_{score}$ derives from the aggregation of four scores:

$$snow_{score} = (3 - T_{score}) + (3 - R_{score}) + S_{score} + F_{score} \tag{7.42}$$

The snow mask, $snow_{mask}$, and a snow cover probability, f_{snow}, are calculated if at least two snow score are available and for sun zenith angle below $80°$.

$$snow_{mask} = \begin{cases} 0 \; if \; snow_{score} \leq 0; \\ \\ 1 \; if \; snow_{score} > 0. \end{cases} \tag{7.43}$$

$$f_{snow} = 1 - \frac{snow_{score} - f_{snow}^{min}}{f_{snow}^{max} - f_{snow}^{min}} \tag{7.44}$$

with f_{snow} ranging between 0 (fully snow covered) and 1 (no snow), $f_{snow}^{min} = $ -15 and $f_{snow}^{max} = 10$.

Cloud detection

The $sparc_{score}$ is calculated as follows:

$$
\begin{aligned}
sparc_{score} = {}&(1 - f_{glint})f_{snow}f_{night}B_{score} + (1 + f_{glint})(2 - f_{snow})(2 - f_{night})T_{score} \\
&+ (1 - 0.6f_{glint})(2 - f_{snow})f_{night}R_{score} + (1 - f_{glint})f_{snow}f_{night}N_{score} \\
&+ (1 - f_{glint})f_{snow}f_{night}UR_{score} + (1 - f_{night})UT_{score} + C_{score} \\
&+ (1 - f_{night})TT_{score} + (1 - f_{night})DT_{score} \quad (7.45)
\end{aligned}
$$

where f_{glint} is an attenuation function which considers that in areas of sun glint the brightnes score is ineffective, and f_{night} is a night mask.

The $sparc_{score}$ is only calculated if the T_{score} is available, thus it is suitable also for sensors having just one thermal channel. From the $sparc_{score}$ a could mask and a classification uncertainty can be derived:

$$
cloud_{mask} = \begin{cases} 0 \; if \; sparc_{score} \; < -4; \\ 1 \; if \; -4 \; \leq sparc_{score} \; < 4; \\ 2 \; if \; sparc_{score} \; > 4. \end{cases} \quad (7.46)
$$

$$
\sigma_{cloud-mask} = exp\left(-\frac{(sparc_{score} - 0.0)^2}{2 \times 10^2}\right) \quad (7.47)
$$

7.4.2 Clear-sky radiation

Clear-sky radiation is global radiation at the Earth's surface under cloud-free conditions. It can be estimated by empirical formulas which consider air mass as an indicator of atmospheric turbidity, or can be calculated by a radiative transfer model (RTM) using specific information on the composition of the atmosphere. HelioMont includes both the methods, in fact the empirical clear-sky model of Kasten et al. (1984) and the algorithm gnu-MAGIC of Müller et al. (2009) are both implemented. The work done in this thesis is based on solar radiation derived with the clear-sky model gnu-MAGIC, which we describe in the following.

Clear-sky model gnu-MAGIC

The clear-sky model gnu-MAGIC (GNU-licensed Mesoscale Atmospheric Irradiance Code) uses the radiative transfer model (RTM) libRadtran (Mayer and Kylling, 2005) with solver DISORT (Stamnes et al., 2000), 16 streams and the correlated-k band parameterization for the solar spectrum (Kato et al., 1999). RTM simulations are performed off-line for discrete values of aerosol optical depth (AOD) and single scattering albedo (ssa), total column water vapor (H_2O), total column ozone (O_3), surface albedo (α) and solar zenith angle (θ_z). A look up table (LUT) is derived, which is used afterwards to reproduce RTM simulations for actual values of atmosphere and surface parameters.

The approach of Müller et al. (2009) is called eigenvector approach. It assumes that aerosol, water vapor, ozone and surface albedo act independently from each other on shortwave radiation, thus their effects can be summed. LUT are computed for different values of AOD and ssa, while H_2O, O_3, α and θ_z are kept constant in these calculations. The effect of H_2O, O_3 and α is included afterwards, by additive correction terms, while the effect of θ_z is considered by applying the so called Modified Lambert-Bear function (MLB). The MLB adapts Equation 5.5, which is monochromatic and valid for direct radiation, to broadband calculations and to global radiation. The monochromatic equation of Lambert-Beer would be:

$$DIR_{cs,\lambda} = I_{0,\lambda} exp \frac{-\tau_{0,\lambda}}{cos(\theta_z)} \tag{7.48}$$

The MLB, instead, is expressed as follows:

$$SIS_{cs} = I_0^* exp \frac{-\tau_0}{cos^a(\theta_z)} cos(\theta_z) \tag{7.49}$$

where the empirical exponent a is calculated from RTM simulations for θ_z equal to 0° and 60°, and I_0^* is the extraterrestrial irradiance at the top of the atmosphere modified to adapt to high AOD values:

$$I_0^* = I_0 \left(1 + I_0 \frac{DIF}{DIR \times SIS} \right) I_0 \tag{7.50}$$

The MLB-eigenvector approach allows to reduce significantly the calculation time compared to running RTM simulations for all the involved parameters. Nevertheless it reproduces very well RTM simulations (Müller et al., 2004).

The effect of surface albedo on diffuse radiation is included by an empirical fit:

$$SIS_{cs} = SIS_{cs}(0.98 + 0.1\alpha) \tag{7.51}$$

The calculations are performed for a Sun-Earth distance of 1 AU, and the final value of $SIS_c f$ for the Earth's orbit eccentricity.

7.4.3 All-sky radiation

All-sky radiation is calculated by a modified HELIOSAT model. First the reference albedo (maximum reflectance) is derived. Then the visible cloud index, as defined in the HELIOSAT method, and the infrared cloud index are calculated. The VIS and IR cloud indexes are combined in a new cloud index, which is used for calculating the clear-sky index. Surface incoming radiation is calculated from the clear-sky index and the clear-sky radiation. Corrections for terrain shading, sky-view and reflections from the surroundings are finally applied.

Reference albedo map

The maximum reflectance, ρ_{max}, corresponding to a fully cloud covered pixel, is calculated from one of the Meteosat SEVIRI visible bands (HRV, 0.6 or 0.8 μm). RTM simulations are performed for the HRV channel of SEVIRI. Top of atmosphere reflectances are calculated considering a set of sun zenith, view zenith, relative sun-view azimuth angles and surface albedo, with a cloud optical thickness of 128. The spectral filter function of the channel is used with the spectral solar

flux.Two look up tables are produced, one for water an one for ice clouds, which give ρ_{max} as a function of view and solar geometry. Water and ice clouds are distinguished according to the fraction of water clouds of each pixel, ϕ_{wc}, calculated as:

$$\phi_{wc} = min \left(max \left(\frac{T_{10.8} - T_{min}}{T_{max} - T_{min}}, 0 \right) \right) \tag{7.52}$$

The LUT values for water and ice clouds are combined linearly by ϕ_{wc}.

This method, which accounts for directional properties of clouds, is very useful in regions characterized by high background reflectance values, where the difference between the clear-sky reflectance, ρ_{cf}, and the cloudy reflectance, ρ_{max}, is reduced, and the cloud index strongly depends on ρ_{max}.

Visible cloud index

The VIS cloud index, N_{vis}, is calculated by the original HELIOSAT formulation as:

$$N_{vis} = \frac{\rho - \rho_{cf}}{\rho_{max} - \rho_{cf}} \tag{7.53}$$

where ρ is the instantaneous pixel reflectance of the visible channel, and ρ_{cf} is calculated by fitting a parameterized curve through all valid clear sky retrievals covering a full day.

The N_{vis} has two main problems. The first regards shadowed pixels, which receive a negative cloud index and are identified as very clear-sky pixels. The second regards snow-covered pixels, which due to the directional effect of snow reflectance have a very high and unrealistically varying N_{vis}, due to the small or negative difference between ρ_{cf} and ρ_{max}.

Infrared cloud index

The IR cloud index, N_{ir}, is calculated as follows:

$$N_{ir} = min(max(a(T_{score} - b) + c(R_{score} - d), 0))^e + N_{min}, N_{max}) \qquad (7.54)$$

where the T_{score} detects very high and thick clouds and is defined as:

$$T_{score} = T_{cf} - T_{10.8} \qquad (7.55)$$

while the modified R_{score} detects low clouds over bright surfaces and is defined as:

$$R_{score} = 500 \frac{\rho_{0.6}^2 \rho_{1.6}^2}{1.5\rho_{1.6}^{2.8}(3.0\rho_{1.6} + 0.5\rho_{0.6} + 3.5) + 1.5\rho_{0.6}^2} \qquad (7.56)$$

The coefficients a, b, c, d and e are estimated once per day by fitting all daily N_{ir} to N_{vis} for pixels with $\rho_{cf} \leq 0.5$. Fitting is performed for regions covering 50×50 pixels and 500 m surface elevation difference. N_{min} and N_{max} are fixed to 0 and 1.05. More details on the calculation of N_{ir} can be found in Stöckli (2013a).

Cloud index

The cloud index is calculated by combining the visible cloud index for dark surfaces and the infrared cloud index for bright surfaces:

$$N = fN_{ir}'' + (1 - f)N_{vis} \qquad (7.57)$$

where

$$f = min\left(max\left(\frac{\rho_{cf} - 0.3}{0.5 - 0.3}, 0\right), 1\right) \qquad (7.58)$$

$$N_{ir}'' = N_{ir}' - \alpha N_{ir}' + \alpha N_{ir}'2 \qquad (7.59)$$

$$N'_{ir} = (N_{ir} - b)/a \tag{7.60}$$

N_{ir} is modified through surface albedo, α. This reduces the radiative effect of clouds over bright surfaces and partially accounts for multiple surface-cloud reflections. The parameters $a = 1.45$ and $b = 0.075$ were estimated with alpine Surface Radiation Budget (ASRB) station data. As an approximation of α the 10% percentile of the diurnal course of ρ_{cf} is used.

Clear-sky index

The clear-sky index K is calculated from the cloud index N by the empyrical relations presented in Hammer et al. (2003):

$$K = \begin{cases} 1.2 \; if \; N \leq -0.2; \\ 1 - N \; if \; -0.2 < N \leq 0.8; \\ 2.0667 - 3.6667N + 1.6667N^2 \; if \; 0.8 < N \leq 1.1; \\ 0.05 \; if \; 1.1 < N. \end{cases} \tag{7.61}$$

Completely clear-sky produces $K = 1.2$ and total cloud-cover produces $K = 0.05$. K exceeds 100% for negative N, i.e. from very dark surfaces. This could be the effect of cloud shadows whose treatment also requires the consideration of cloud parallax.

Terrain shadows

Terrain shadow is calculated by comparing the solar elevation angle, H_s, to the horizon angle, H_t, in the mean direction of the horizon azimuthal sector, a, closest to the azimuth direction, ϕ:

$$S_t = \begin{cases} 1 \; if \; H_s \leq H; \\ 0 \; if \; H_s > H. \end{cases} \tag{7.62}$$

where

$$a = min(ceil(\phi\,n/360 - 0.5), n - 1) \tag{7.63}$$

where n is the number of azimuthal sectors, which in HelioMont was set to 100. On tilted planes:

$$S_p = \begin{cases} 1 \; if \; \theta_{s-p} > 90; \\ \\ 0 \; if \; \theta_{s-p} \leq 90. \end{cases} \tag{7.64}$$

where θ_{s-p} is the angle between the sun direction and normal to the plane.

Clouds shadows

HelioMont includes a geometric and a radiometric cloud shadow detection. According to the radiometric detection S_c becomes larger for surfaces which have a reflectance which is lower than the non-shadowed clear-sky reflectance. S_c is 1 when ρ is less than 50% of ρ_{cf}, and is 0 when ρ is higher than 90% of ρ_{cf}.

$$S_c = 1 - min\left(max\left(\frac{\rho - 0.5\rho_{cf}}{0.9\rho_{cf} - 0.5\rho_{cf}}, 0\right), 1\right) \tag{7.65}$$

Thus S_c is 1 when ρ is less than 50% of ρ_{cf}, and is 0 when ρ is higher than 90% of ρ_{cf}.

The geometric correction is a shift in the cloud shadow position with respect to the cloud position that depends on the cloud height.

Surface radiation

Surface radiation is calculated with the gnu-MAGIC approach. The gnu-MAGIC clear-sky model gives as output both the global and direct beam irradiance. Non-shadowed global, direct beam and diffuse radiation can be calculated as follows:

$$SIS = K \; SIS_{cf} \tag{7.66}$$

$$DIR = f_{dir}DIR_{cf} \tag{7.67}$$

$$DIF = SIS - DIR \tag{7.68}$$

where:

$$f_{dir} = \begin{cases} (K - 0.38(1 - K))^{0.25} \; if \; K \geq 0.5; \\ \\ 0 \; if \; K < 0.5. \end{cases} \tag{7.69}$$

Direct beam irradiance is set to 0 for K below 0.5, since it can be ignored for high cloud optical thickness. Finally, terrain, tilted plane and cloud shadows are added:

$$DIR = DIR(1 - S_t)(1 - S_p)(1 - S_c)cos(\theta_{s-p})/cos(\theta) \tag{7.70}$$

$$DIF = f_{sky}DIF + \alpha(1 - f_{sky})SIS \tag{7.71}$$

$$SIS = DIR + DIF \tag{7.72}$$

Chapter 8

Validation and improvement of the algorithm HelioMont

8.1 Abstract

This chapter evaluates the suitability of the method HelioMont, developed by MeteoSwiss for estimating solar radiation from geostationary satellite data over the alpine region[1]. The algorithm accounts for the influence of topography, clouds, snow cover and the atmosphere on incoming solar radiation. The main error sources are investigated for both direct and diffuse solar radiation components by comparison with ground based measurement taken at three sites, namely Bolzano (IT), Davos (CH) and Payerne (CH), encompassing different topographic conditions. The comparison shows that the method provides high accuracy of the yearly cycle: the mean absolute bias (MAB) is below 5 Wm^{-2} at the lowland station Payerne and below 12 Wm^{-2} at the other two mountainous stations for the monthly averages of global and diffuse radiation. For diffuse radiation the MAB is in the range 11-15 Wm^{-2} for daily means and 34-40 Wm^{-2} for hourly means. It is found that the largest errors in diffuse and direct radiation components at shorter time scales occur during summer and for cloud-free days. In both Bolzano and Davos

---

[1]This chapter is based on Castelli et al. (2014)

the errors for daily-mean diffuse radiation can exceed 50 Wm^{-2} under such conditions. As HelioMont uses monthly climatological values of atmospheric aerosol characteristics, the effects of this approximation are investigated by simulating clear-sky solar radiation with the Radiative Transfer Model (RTM) libRadtran using measured data on aerosols. Both ground based and satellite data on aerosols optical properties and water vapor column amount are evaluated. Using daily atmospheric input the estimation of the hourly averages improves significantly and the mean error is reduced to 10-20 Wm^{-2}. These results suggest the need for a more detailed characterization of the local-scale clear-sky atmospheric conditions for modeling solar radiation at daily and hourly time scales.

8.2 Introduction

Heliosat versions including the look up table (LUT) approach were variously validated and results are reported in many papers. For example in Ineichen et al., 2009 the hourly averages of global irradiance were validated against 8 European stations during 4 months. An overall Root Mean Square Error (RMSE) between 80 and 100 Wm^{-2} and Mean Bias Deviation (MBD) between -15 and 20 Wm^{-2} were found. Clear-sky and overcast conditions were also considered separately, finding an underestimation in the first case and an overestimation in the second one. The underestimation in clear-sky cases was also correlated to an overestimation of the Aerosol Optical Thickness (AOT) used for the interpolation from the LUTs. Furthermore, Journée and Bertrand, 2010 validated global irradiance at 13 sites in Belgium. The 10 minutes averages of ground measurements were compared to the satellite estimations derived from the corresponding instantaneous observations, with a resolution of 1 hour. Mean Absolute Bias (MAB) larger than 60 Wm^{-2} and MBD between -18 and 8 Wm^{-2} were observed. An underestimation in clear-sky conditions has been noticed also in the last mentioned paper. Some validation results can also be found in Betcke et al., 2006. However, to the best of

our knowledge, no detailed analysis of the diffuse and direct irradiance components calculated with the LUT approach has been done so far. Moreover no validation studies have been performed with satellite-derived solar irradiance over complex terrain, with the exception of Dürr et al., 2010.

This paper aims at assessing the reliability of the HelioMont method for retrieving irradiance from Meteosat Second Generation (MSG) satellite data at three specific measurement locations in the Alps encompassing different topographic conditions. In particular the realism of the algorithm in estimating the direct and diffuse components of solar radiation is investigated with respect to atmospheric input data, such as aerosol properties.

The structure of this paper is the following: section 2 describes the algorithm HelioMont and gives the technical details of the ground measurements used for the validation; section 3 presents the results of the validation at different time scales and under different sky conditions; section 4 shows the results of RTM simulations of solar radiation to emphasize the role of aerosols; in last section the conclusions derived from the outcome of the present analysis are summarized and discussed, and possible applications of the present study are proposed.

8.3   Data and method

The present study validates shortwave solar radiation at the Earth surface, derived by MeteoSwiss from MSG data, against surface based point measurements. We investigated separately global irradiance (SIS, Surface Incoming Shortwave Radiation) and its diffuse (SISDIF, Surface Incoming Shortwave Radiation - Diffuse component) and direct normal (SISDNI, Surface Incoming Shortwave Radiation - Direct Normal Irradiance) components, since they can be used in different applications and their relative amount influences the efficiency of their exploitation.

The statistical parameters adopted here to compare the irradiance components are the Mean Bias Deviation (MBD), the Mean Absolute Bias (MAB), the Root

Mean Square Error (RMSE), and the R squared correlation coefficient of the linear regression between satellite estimate and ground based measurements (R^2). All these parameters are calculated according to the formulation of Wilks, 2011.

Since the processing of MSG data is limited to slots corresponding to sun elevation angles above 3°, we filled the few missing MSG data using the relation between all-sky and cloud-free irradiance, whose ratio is generally referred to as clear-sky index (k). We calculated the daily average clear-sky index (k_d), both for global and direct irradiance, as the ratio between the daily mean irradiance and the daily mean clear-sky radiation (SISCF):

$$k_d = \frac{SIS_d}{SISCF_d} \tag{8.1}$$

Afterwards we replaced instantaneous missing data with the product of k_d and the instantaneous clear-sky irradiance, which is modeled with the MAGIC approach:

$$SIS(missing) = k_d \times SISCF \tag{8.2}$$

The cloud-free SISDNI was calculated as the radio between the cloud-free direct irradiance and the sun zenith angle θ.

After filling missing values, we generated hourly and daily means of MSG data from instantaneous measurements taken every 15 min, while we aggregated hourly and daily averages of ground based data from measurements taken at 1 min sampling interval. In both cases monthly means were produced from daily means, considering only those days in which both satellite and ground measurements were available. The procedure, generally adopted in literature, of comparing instantaneous satellite data with the synchronous 10 min averages of ground measurements, was not used in this paper, because the scope was to investigate if the model describes properly the variability of solar radiation at different time resolutions, rather than if it accurately reproduces ground measurements at the time of acquisition.

First we validated *all-sky* data. Then we split them according to three sky condition categories, namely *cloud-free*, *thin clouds* and *overcast*, and repeated the validation for each class. The discrimination was performed coherently with the cloud mask calculated with the method of Stöckli, 2013a, presented in next subsection.

8.3.1 The method HelioMont for deriving SIS from MSG data

The algorithm implemented by MeteoSwiss for retrieving solar radiation from MSG data is presented in Stöckli, 2013a and shortly summarized here. Data from the SEVIRI (Spinning Enhanced Visible and Infrared Imager) instrument on board the MSG satellites are used. This instrument has 12 channels in the visible and infrared bands for monitoring the reflected solar radiation and thermal emission of the Earth. SEVIRI has a spatial resolution at nadir of around 1 km for the High Resolution Visible (HRV) channel and 3 km for the other channels.

The retrieval of the clear-sky global (SISCF) and direct beam irradiance (SIS-DIRCF) is based on the GNU-MAGIC clear-sky model Müller et al., 2009. RTM simulations with libRadtran Mayer et al., 2005 are conducted for discrete values of aerosol optical properties, total column water vapor and ozone concentrations. The resulting LUTs are then applied to 6-hourly atmospheric states (water vapor and ozone) determined on the basis of numerical model output from ECMWF Dee et al., 2011 and a monthly aerosol climatology Kinne, 2008.

The cloud effect on clear-sky SIS is calculated by applying the well established Heliosat algorithm for dark surfaces, extended by a newly developed near-infrared and infrared cloud index for bright surfaces such as snow or desert. For identifying the state of each pixel MeteoSwiss adopts a probabilistic cloud mask based on the algorithm SPARC (Separation of Pixels using Aggregated Rating over Canada),

proposed by Khlopenkov and Trishchenko, 2007. The method was originally developed for AVHRR (Advanced Very High Resolution Radiometer) and adapted by MeteoSwiss to MSG SEVIRI Fontana et al., 2010. While most cloud masks use a classification tree, SPARC produces an additive rating from individual tests, which represents the probability of cloud contamination for each pixel. In addition to analyzing temperature, reflectance, and their spatial uniformity, two new tests are added to SPARC for testing the temporal variability of reflectance and temperature.

The surface radiation is finally calculated by scaling the expected clear-sky radiation with the clear-sky index (k), which is a function of the cloud index:

$$SIS = k(n) \times SISCF \tag{8.3}$$

MeteoSwiss has also implemented correction methods accounting for the effects of topography, such as shadowing, reflection, local horizon elevation angle and sky view factor. The Shuttle Radar Topography Mission (SRTM) digital elevation model, with a spatial resolution of 3 arc-second, is downscaled to $0.02° \times 0.02°$ and used to determine the altitude and the horizon of each pixel.

8.3.2 Ground based radiation data

We used three ground stations for the validation, two in the Swiss Alps and one in the Italian Alps (Fig. 8.1). All of the stations measure SIS, SISDIF and SISDNI.
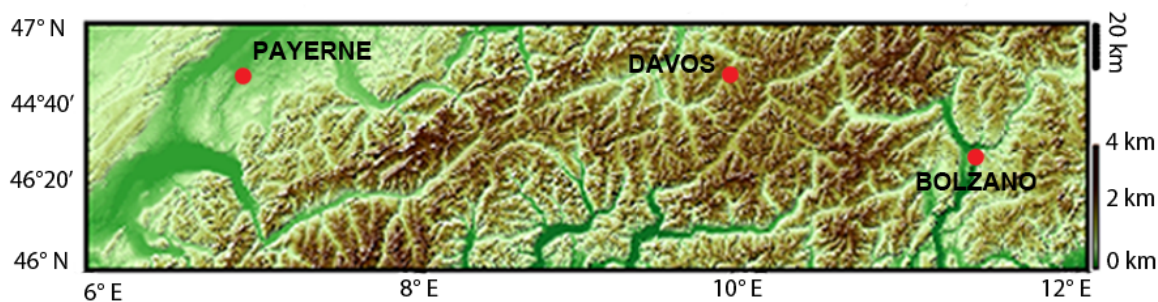
Figure 8.1: Digital elevation model of the area of interest. Data from SRTM/NASA (Shuttle Radar Topography Mission) at 3 arc-second resolution. The red dots represent the measurement stations of solar radiation which we use in this paper.

The station of Bolzano (IT) is located at the valley floor, at an altitude of 262 MSL, at the junction of the three valleys: Val d'Isarco, Val Sarentina and Val d'Adige. The instruments are mounted at 1 m above ground, and in the surroundings there are the airport runway, crops and industrial facilities. In Bolzano observations are collected by three Kipp&Zonen instruments, i.e. 2 pyranometers model CMP11 (one measuring global irradiance and the other one combined with a sun tracker equipped with a shadow sphere that intercepts direct solar radiation for measuring diffuse radiation), and a pyrheliometer model CHP1 measuring direct irradiance. All the instruments used for the validation are regularly calibrated once per year.

In Davos (CH) instruments are mounted at the Physical-Meteorological Observatory and World Radiation Center (PMO/WRC), at an altitude of 1610 MSL, on the wind mast of the Swiss Meteorological Institute, with grassland underneath. Data from Davos used in the present analysis were measured by two Kipp&Zonen CM21 pyranometers, one for SIS and the other for SISDIF, and a Kipp&Zonen CHP1 pyrheliometer for direct normal irradiance. All the radiation instruments are mounted on an arm fixed at about 2 m distance from the main mast and about 4-8 m above the ground. The pyranometer measuring diffuse irradiance is equipped with a fixed shadow band pointing South.

The station of Payerne (CH) is part of the Baseline Surface Radiation Network (BSRN), which is a project of the Radiation Panel from the Global Energy and Water Cycle Experiment (GEWEX). The experiment aims at acquiring the best possible surface radiation budget information, and was initiated by the World Climate Research Programme (WCRP). The radiation instruments of Payerne are located at MeteoSwiss, at an altitude of 491 MSL, and have grassland with crops in the vicinity. In Payerne DNI is measured with Kipp & Zonen CHP1, whereas SIS and SISDIF are measured by two Kipp&Zonen CM21 pyranometers.

For this validation study we adopted 2011 as test year for performing the comparison between satellite and ground data in Bolzano and Davos, while in

Payerne we carried out the analysis with data since 2004 to 2009, according to the availability of ground measurements.

8.3.3 Satellite and ground based atmospheric data

In order to test the sensitivity of radiation components to atmospheric input, we also simulated SIS, SISDIF and SISDNI with the RTM libRadtran by using atmospheric inputs with a higher temporal resolution than the climatological ones used in the method of Stöckli, 2013a.

At a first stage, we took AERONET (AErosol RObotic NETwork) measurements of Aerosol Optical Thickness (AOT), Single Scattering Albedo (SSA), and precipitable water. AERONET is a global network of sun photometers (SP) Holben et al., 1998. The SP performs one direct measurement pointing at the sun, and one direct at the sky, at different wavelengths in the range 0.34-1.02 μm. This set of measurements allows a direct estimation of aerosol macro-physical properties such as AOT, and an indirect estimation of micro-physical properties, like the SSA. All the data from the sites around the world are collected and processed by NASA. Level 1.5 (cloud-screened) AOT, SSA and water vapor data for the stations of Bolzano and Davos have been downloaded from the AERONET website (http://aeronet.gsfc.nasa.gov).

At a second stage, considering the low number of AERONET stations in the Alps, for water vapor column amount we used the ERA Interim reanalysis of the ECMWF (European Centre for Medium-Range Weather Forecasts) at 0.25×0.25 degree grid, and for aerosols satellite data, specifically MODIS (MODerate resolution Imaging Spectroradiometer) retrieval of AOT, and OMI (Ozone Monitoring Instrument) SSA product. The instrument MODIS is on the EOS (Earth Observing System) Terra and Aqua polar orbiting satellites. It has 36 spectral bands between 0.41 and 14 μm. The satellites Terra and Aqua cross Europe at around 10:30 and 13:30 local solar time. MODIS AOT Collection 5 Levy et al., 2007

overland retrievals use four channels centered at 0.47, 0.66, 1.24 and 2.1 μm with a nominal resolution of 500 or 250 m at nadir. To reduce noise, the AOT at 0.55 μm is calculated in boxes of 10 $\times$ 10 km^2, averaging the 20 to 50 percentile of surface reflectance in each box. OMI is on EOS Aura polar orbiting satellites. Its measurements cover the spectral region between 264 and 504 nm, with a spectral resolution between 0.42 nm and 0.63 nm and a nominal ground footprint of 13 $\times$ 24 km^2 at nadir. Complete global coverage is achieved in one day.

8.4   Results

8.4.1   Validation of all-sky SIS, SISDIF and SISDNI

The results of the validation for the three stations of interest are summarized in Tables 8.1 - 8.3, respectively at the hourly, daily and monthly time scale, in terms of MAB and MBD, including both the all-sky and the specific sky conditions.

The validation of the monthly averages (Figs. 8.2a - 8.2c) indicates that the satellite estimation is useful to reproduce the seasonal cycle of the components of global radiation with a MAB of 3 Wm^{-2} in flat terrain like Payerne and 7 and 12 Wm^{-2} in steep terrain like Davos and Bolzano, respectively. Despite the agreement between the monthly averages of satellite and ground based data, both in Bolzano and Davos diffuse irradiance is always overestimated by the satellite algorithm in the period of analysis (Tab. 8.3). This makes it interesting to investigate what happens at shorter time scales.

STATION	YEARS	SKY COND.	MAB [Wm^{-2}]			MBD [Wm^{-2}]		
			SIS	SISDIF	SISDNI	SIS	SISDIF	SISDNI
Bolzano (IT)	2011	all sky	52	40	128	6	15	-10
		cloud free	40	45	116	17	36	-24
		thin clouds	51	31	121	4	-1	16
		overcast	62	35	137	-17	-10	-18
Davos (CH)	2011	all sky	52	42	144	-6	14	-49
		cloud free	27	41	134	-5	38	-89
		thin clouds	54	30	182	6	9	2
		overcast	72	48	136	-12	-2	-45
Payerne (CH)	2004-2009	all sky	40	34	110	2	-5	22
		cloud free	20	30	96	10	12	-6
		thin clouds	46	29	148	15	-13	73
		overcast	49	38	89	-8	-11	17

Table 8.1: MAB and MBD (Wm^{-2}) of the validation of hourly averages of SIS, SISDIF and SISDNI for different sky conditions in Bolzano, Davos and Payerne.

In Bolzano positive values of MBD were observed for all the irradiance components, both in the monthly, daily and hourly validation, suggesting that satellite data generally overestimate irradiance at this location. The local minimum of the monthly averages of SIS and SISDNI in June (Fig. 8.2a) is clearly associated with the low number of cloud free days (only 2) and with the secondary peak of convective precipitations which is typically observed in the Alps. The validation of the daily averages (Tab. 8.2) outlines difficulties in estimating diffuse irradiance from satellite data ($R^2 = 0.758$, MBD = 8 Wm^{-2}, MAB = 15 Wm^{-2}). Analogous results were observed for the hourly averages (Tab. 8.1) ($R^2 = 0.735$, MBD = 15 Wm^{-2}, MAB = 40 Wm^{-2}).

In Davos (Fig. 8.2b) the validation gives results similar to those recorded for Bolzano. A minimum of SIS and SISDNI is observed again in summer, and is associated with the high number of cloudy days (in June and July there were only 2 cloud-free days in total). Both monthly, daily and hourly analyses show

that satellites overestimate diffuse irradiance (MBD > 12%) and underestimate direct normal irradiance (MBD < -4%), although global irradiance turns out to be slightly underestimated in the hourly (MBD = -6 Wm^{-2}) and daily (MBD = -2 Wm^{-2}) analysis. Like for Bolzano, daily averages of diffuse irradiance are not as strongly correlated with ground data (R^2 = 0.808) as for global irradiance (R^2 = 0.909).

In Payerne (Fig. 8.2c) the validation shows high accuracy of the monthly-mean satellite global irradiance (MAB = 3 Wm^{-2}, MBD = 1 Wm^{-2}), and diffuse irradiance is only slightly underestimated (MBD = -3 Wm^{-2}), whereas direct normal irradiance is overestimated (MBD = 14 Wm^{-2}). The daily averages of the diffuse component over the 6 years of analysis are underestimated (MAB = -3 Wm^{-2}) with R^2 = 0.853.

STATION	YEARS	SKY COND.	MAB [Wm^{-2}]			MBD [Wm^{-2}]		
			SIS	SISDIF	SISDNI	SIS	SISDIF	SISDNI
Bolzano (IT)	2011	all sky	14	15	33	4	8	4
		cloud free	30	40	236	19	31	168
		thin clouds	46	30	115	1	-2	9
		overcast	47	21	124	-20	-7	-31
Davos (CH)	2011	all sky	14	15	33	-2	7	-11
		cloud free	19	34	250	1	33	111
		thin clouds	49	24	162	7	4	22
		overcast	51	29	102	-16	-2	-34
Payerne (CH)	2004-2009	all sky	10	11	31	1	-3	12
		cloud free	19	24	333	12	3	269
		thin clouds	41	27	140	14	-13	74
		overcast	32	25	70	-9	-12	16

Table 8.2: MAB and MBD (Wm^{-2}) of the validation of daily averages of SIS and SISDIF for different sky conditions in Bolzano, Davos and Payerne

	SIS			SISDIF			SISDNI		
STATION	RMSE	MAB	MBD	RMSE	MAB	MBD	RMSE	MAB	MBD
Bolzano	16	12	6	12	10	9	27	23	8
	6%	7%	4%	22%	1%	16%	14%	12%	4%
Davos	9	7	-1	9	7	7	18	13	-11
	5%	5%	0.2%	14%	14%	13%	9%	10%	-9%
Payerne	4	3	2	6	5	-3	21	18	14
	3%	2%	1%	9%	8%	-4%	15%	12%	10%

Table 8.3: RMSE, MAB and MBD (Wm^{-2}) for the monthly averages of SIS, SISDIF and SISDNI in Bolzano, Davos and Payerne. The second row indicates for each station the same parameters in percentage of the corresponding mean value of ground measurements.

(a) Bolzano
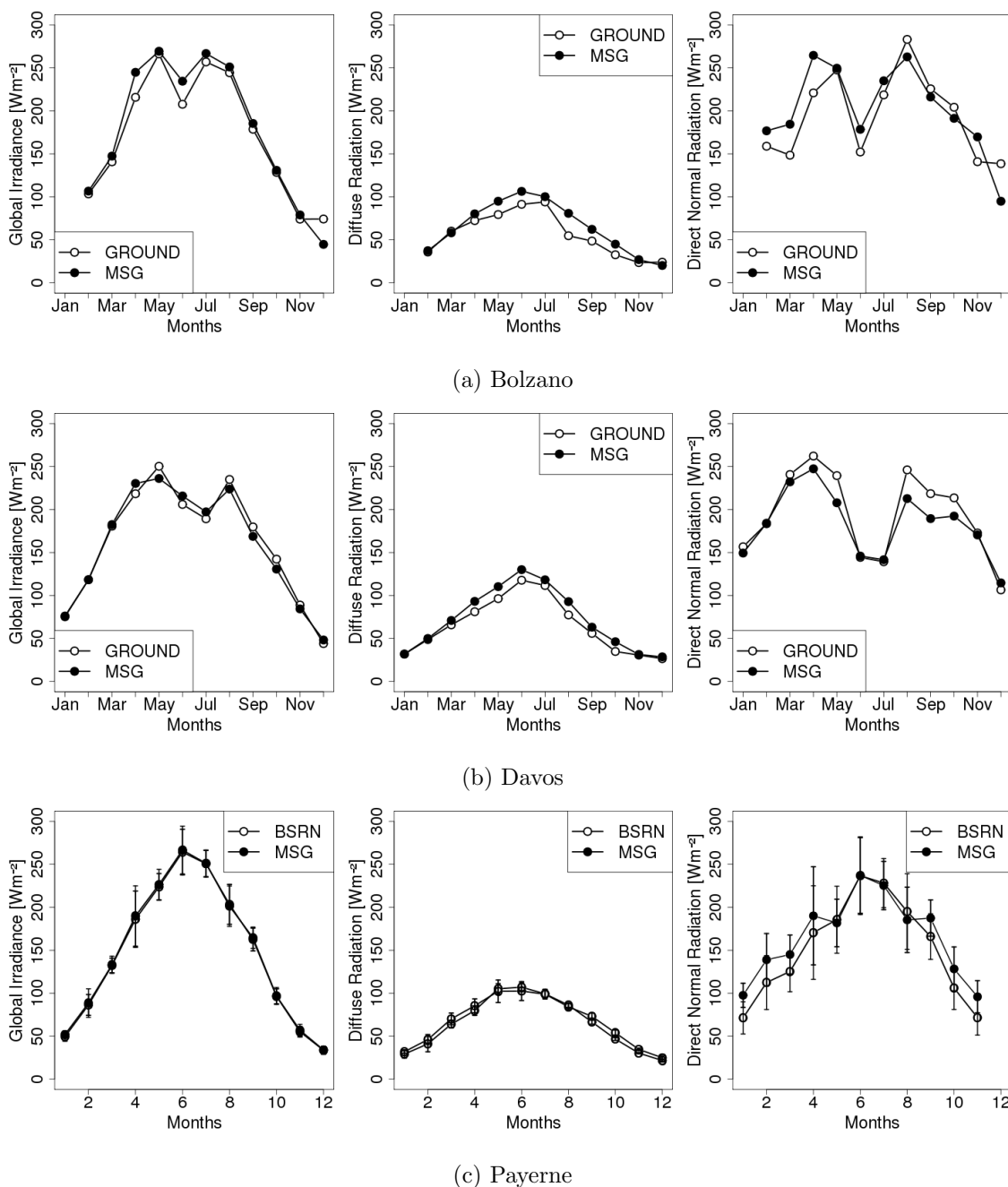
(b) Davos

(c) Payerne

Figure 8.2: Monthly averages of satellite and ground based irradiance in Bolzano (2011), Davos (2011) and Payerne (2004-2009). The local minima of global and direct normal irradiance in June and July in Bolzano and Davos are due to the high percentage of cloudy days. In Bolzano no data were available for January because the radiometers were installed in February 2011. In Figure 8.2c the error bars represent the inter-annual standard deviation of monthly averages of satellite and ground measurements. Given its low variability from year to year, the climatology of SISDIF can be considered representative of the single years.

After having summarized the outcome of the analysis, it is important to clarify

that the results obtained in Payerne are not climatologically equivalent with the ones obtained for the other two stations. The periods of investigation, in fact, have different lengths and do not overlap. In Bolzano and Davos we validated data of the year 2011 only, thus results are affected by the specific conditions of the year under investigation and are suitable for understanding if the satellite algorithm describes properly the short term variability of the irradiance components. On the other hand, results for Payerne were derived from the analysis of six years of data, consequently they can be considered representative for the long term pattern of the error in the satellite estimation of solar radiation.

8.4.2 Validation of the mean diurnal cycle of SIS, SISDIF and SISDNI

In Bolzano and Davos the mean diurnal cycle (Fig. 8.3) reveals a strong overestimation of diffuse irradiance. Furthermore global irradiance is overestimated in the morning and underestimated during the rest of the day.

In Payerne the mean diurnal cycle (Fig. 8.4) shows a strong overestimation of direct normal irradiance, while diffuse irradiance is underestimated around noon, and global irradiance is overestimated in the morning and underestimated in the afternoon, similarly to the results observed for Bolzano and Davos.

The strong diurnal cycle of the estimation error is likely connected to the difference in spatial footprint of the data that we compared. A satellite pixel of 2 km^2 represents, in fact, the mean over substantial subgrid-scale topographic variability (slope, orientation, horizon altitude) and surface reflectance, whereas a station measurement is representative only for a small part of these topographic boundary conditions.
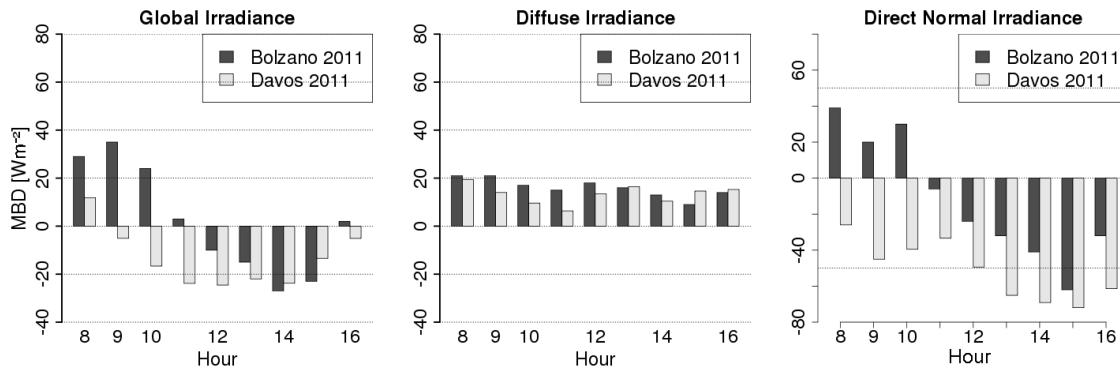
Figure 8.3: Mean diurnal cycle of MBD of irradiance components in Bolzano and Davos. Only the data between 8 a.m. and 4 p.m. are represented because they are descriptive of the entire dataset, in fact in the remaining hours, during autumn and winter, the sun is below the local horizon.
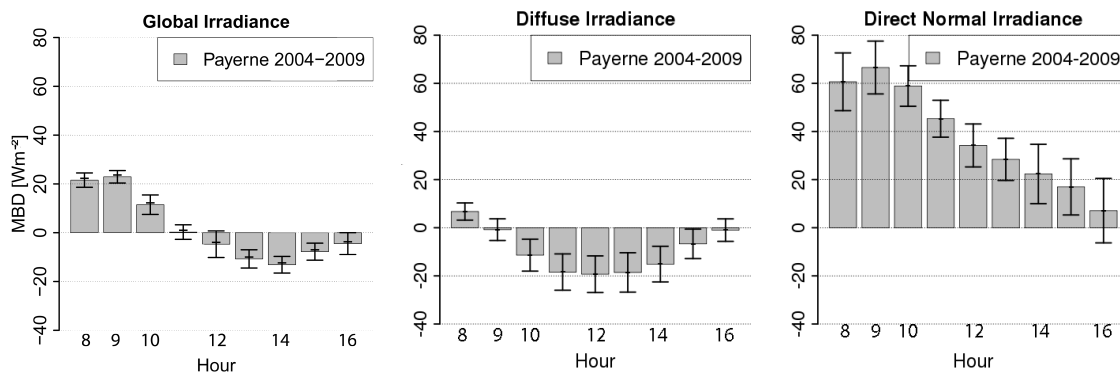
Figure 8.4: Mean diurnal cycle of MBD of irradiance components in Payerne. Only the data between 8 a.m. and 4 p.m. are represented because they are descriptive of the entire dataset, in fact in the remaining hours, during autumn and winter, the sun is below the local horizon. The error bars represent the standard deviation of the daily cycle of MBD in the 6 years 2004-2009.

8.4.3 Validation of SIS, SISDIF and SISDNI under different sky conditions

In order to examine the most problematic conditions, we split data in classes according to the season and to the cloudiness status. Three cloudiness classes, i.e. cloud-free (CF), thin clouds (TC) and overcast (OC), were adopted, in accordance with the cloud mask computed by HelioMont. We considered an hour either cloud free or overcast only if the cloud mask was equal to 0 or 2 respectively for all the

time slots, while we classified an hour as TC for mean hourly values of the cloud mask between 0.8 and 1.2. The remaining intermediate cases were excluded for avoiding to mix different sky conditions. For computing daily averages we selected only those hours in which both satellite and ground data belonging to a specific class were available.

The hourly (Tab. 8.1) and daily (Tab. 8.2) validation show that in CF conditions the estimation error of the irradiance components is much higher than in the other cases, especially in Bolzano and Davos, where diffuse radiation is strongly overestimated (MBD is in the range 31-38 Wm^{-2}). Considering these results, we calculated the monthly averages of diffuse radiation including only the time interval between 10 a.m. and 2 p.m., in order to quantify the influence on the yearly cycle of the estimation error considering only those hours in which most radiation is available (Fig. 8.6). In Bolzano and Davos MBD and MAB resulted much higher than under the other sky conditions, while in Payerne there was the opposite situation (see Tab. 8.4 for MBD and MAB values under TC and OC conditions).

	MBD [Wm^{-2}]		MAB [Wm^{-2}]	
	TC	OC	TC	OC
Bolzano	-9	-23	19	24
Davos	2	-14	38	22
Payerne	-21	-24	32	25

Table 8.4: MAB and MBD (Wm^{-2}) for the monthly averages of SISDIF in Bolzano (2011), Davos (2011) and Payerne (2004-2009) under thin clouds (TC) and overcast (OC) conditions. Only the time interval between 10 a.m. and 2 p.m. was considered in the averaging of cloud mask and irradiance because it was observed that most of the estimation error was concentrated in these hours, which are also those in which most of the irradiance is available.

In next subsection we examine the possible causes of error in the satellite estimation of diffuse radiation under clear-sky conditions.

(a) Bolzano
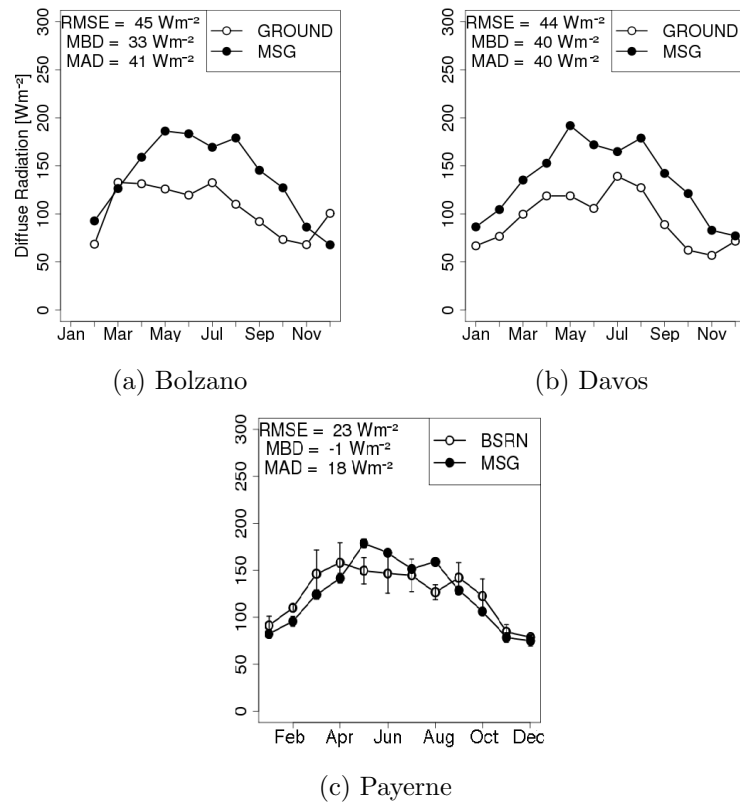
(b) Davos

(c) Payerne

Figure 8.5: Monthly averages of satellite and ground measurement of diffuse irradiance in Bolzano (2011), Davos (2011) and Payerne (2004-2009) under clear-sky conditions. Only the time interval between 10 a.m. and 2 p.m. was considered in the averaging of cloud mask and irradiance because in these hours most of the irradiance is available.

(a) Bolzano   (b) Davos
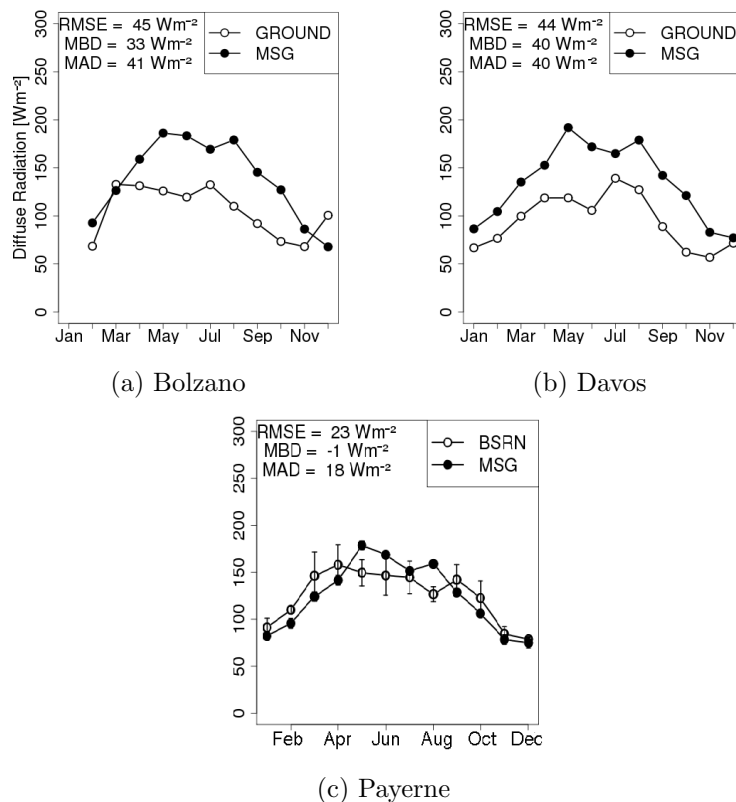
(c) Payerne

Figure 8.6: Monthly averages of satellite and ground measurement of diffuse irradiance in Bolzano (2011), Davos (2011) and Payerne (2004-2009) under clear-sky conditions. Only the time interval between 10 a.m. and 2 p.m. was considered in the averaging of cloud mask and irradiance because in these hours most of the irradiance is available.

8.4.4 Sources of error in the estimation of diffuse radiation

The behavior observed under clear-sky conditions can be partially explained considering processes and factors contributing to diffuse irradiance in absence of clouds. They can be summarized as follows, together with a description of the model simplifications:

1. Mie scattering by aerosols is weakly wavelength selective, and particularly effective on visible light, where most of solar energy is concentrated: monthly values of aerosol optical characteristics are used to interpolate irradiance values from the LUTs. The global-scale $1° \times 1°$ aerosol data cannot represent the vertical stratification of aerosols within the ABL in complex topography.

AOD at high elevation locations is thus likely to be overestimated by the satellite retrieval;

2. Rayleigh scattering by atmospheric gases, whose effectiveness is confined in the ultraviolet part of solar spectrum, is much less relevant than Mie scattering on broadband radiation: the model assumes a fixed atmospheric profile (US standard atmosphere) and uses the *Kato band-parameterization* Kato et al., 1999;

3. surface reflection: the impact of surface albedo on clear-sky irradiance is approximated by using the clear-sky top-of-atmosphere reflectance as a surrogate for surface albedo. This approximation would need to be replaced by the estimation of an atmospherically corrected hemispherical surface albedo;

4. the sky-view-factor (see next section for its definition) reduces diffuse radiation according to the visible portion of the sky vault: it is calculated from the horizon angle, thus is affected by the low resolution of the DEM, originally set at a resolution of 100 m, and then down-sampled to the MSG HRV (High Resolution Visible) pixel size, which is around 1 km East-West and around 1.7 km North-South. It is thus likely that the local-scale sky-view-factor at valley stations Bolzano and Davos is lower compared to the sky view factor of the mean MSG HRV pixel;

5. the diffuse-to-global ratio increases with optical air mass, i.e. with the sun zenith angle: this effect is considered by applying the *modified Lambert-Beer* relation, developed and validated in Müller et al., 2004 and EHF et al., 2003, and also verified in Ineichen, 2006.

To summarize, the most critical approximations in the satellite-based clear-sky model are associated with aerosols scattering and surface reflectance. More in-depth examination is necessary for solving the surface-related issues. These

problems have been partially addressed in Lee et al., 2011. In next section we investigate the effects of aerosols and suggest a way to introduce more accurate data in the model.

8.5 Modeling the effect of aerosols

Since the validation study highlighted problems in the estimation of diffuse irradiance under clear-sky conditions, it is interesting to quantify the influence of atmospheric absorption and scattering on the diffuse fraction of solar radiation. We carried out this study for Bolzano and Davos, which are equipped with a sunphotometer measuring aerosol optical properties and water vapor column amount, and are part of the AERONET network. The most interesting days to investigate would have been the summer days in which the largest discrepancy was observed. However data analysis had to be adapted to data availability, thus it was limited to the months containing most cloud free days and for which most AERONET data were available, i.e. August for Bolzano and November for Davos.

We used AERONET measurements of AOT, SSA, and precipitable water. Then we calculated daily averages of these atmospheric parameters and assumed them constant throughout each day in the simulations. Surface albedo was set constant and equal to 0.4 in Davos and 0.1 in Bolzano, and ozone column amount was also fixed at 300 Dobson units.

We modeled diffuse radiation by the RTM libRadtran, adopting as radiative transfer equation solver the discrete ordinate code *disort* Stamnes et al., 1988 with 6 streams. The correlated-k approach of Kato Kato et al., 1999 was used to compute the spectral transmittance assembling the absorption coefficients of different gases. We performed RTM runs every 15 minutes in the time interval between 10 a.m. and 2:45 p.m. in which the influence of shadowing is the smallest.

We reduced the simulated diffuse irradiance considering the Sky View Factor (SVF) calculated for Bolzano and Davos from the horizon angle:

$$SISDIF_{cor} = SISDIF \times SVF + SISDIF \times \alpha(1 - SVF) \qquad (8.4)$$

where α is the surface albedo and SVF is the ratio between diffuse irradiance at a point and that on an unobstructed horizontal surface Dozier and Marks, 1987 under the assumption of isotropic distribution of diffuse irradiance.

As shown in Figs. 8.8a and 8.8b, libRadtran simulates diffuse radiation with high accuracy when site-specific aerosol and water vapor measurements are used (MAB on hourly averages is 13 Wm^{-2} in Bolzano and 5 Wm^{-2} in Davos, MBD is 4 Wm^{-2} in Bolzano and 4 Wm^{-2} in Davos), while the satellite estimate significantly exceeds ground measurements in clear-sky days (MBD is 72 Wm^{-2} in Bolzano and 32 Wm^{-2} in Davos).

Only four AERONET stations are based in the Alps at Davos, Bolzano, Laegern (47°.48 N, 8°.35 E, 735 m MSL) and Jungfrau (46°.55 N, 7°.98 E, 3580 m MSL). Consequently, in order to obtain spatially distributed information on aerosols, we used AOT from MODIS (10 km × 10 km), SSA from OMI (0.25° × 0.25°) and water vapor total column amount from the ERA Interim reanalysis of the ECMWF (0.25° × 0.25°).

In Bolzano we selected the clear-sky days of August 2011 in which MODIS data were available, and run simulations with the same settings as in the previous analysis. Finally we compared the hourly averages of simulated and ground based data. The MAB against ground data resulted twice as large (20 Wm^{-2}) as that obtained by using AERONET data. Nevertheless results were much better than for the satellite estimation of diffuse radiation (MAB = 65 Wm^{-2}).

These results suggest that an accurate satellite estimate of diffuse irradiance requires at least daily data on the composition and optical properties of the atmosphere.
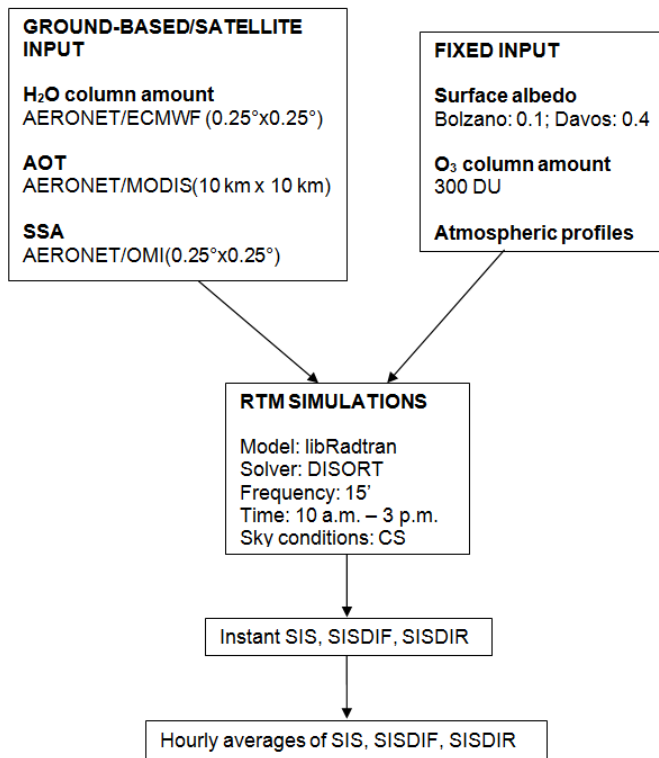
Figure 8.7: Summary of the input used for performing RTM simulations in Bolzano and Davos.
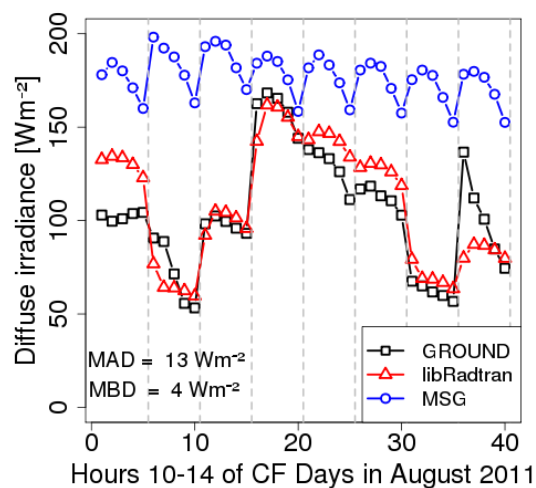
(a) Bolzano. Cloud-free days of August 2011.
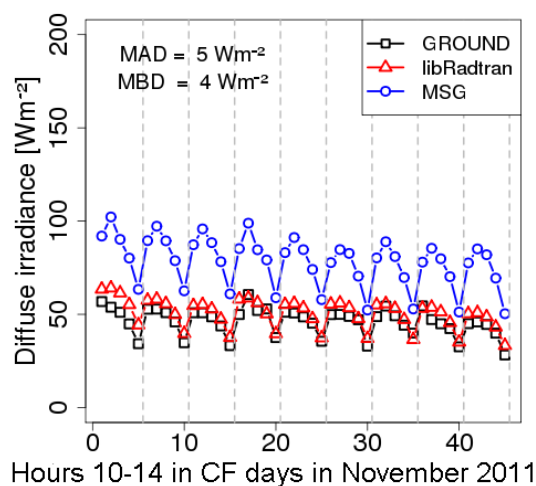
(b) Davos. Cloud-free days of November 2011.

Figure 8.8: Hourly averages of RTM simulations, ground measurements, and satellite retrieval of diffuse irradiance in Bolzano and Davos. MAB and MBD refer to the comparison between RTM simulations and ground measurements. Only the hours between 10 a.m. and 2 p.m. were considered. The daily averages of AOT, SSA and water vapor column amount measured by AERONET sun photometers were used as input for RTM simulations. The vertical dashed lines separate the days from each other. On the x axis there is the sequence cloud-free hours (40 for Bolzano, 45 for Davos) for which averages were computed. The surface albedo was set to 0.1 in Bolzano and 0.4 in Davos.

8.5.1 MACC aerosol data

Re-analysis projects like MACC (Inness et al., 2012) and GOCART (Chin et al., 2000, 2002) could offer a better description of the composition of the atmosphere used in satellite-based models for estimating irradiance components. These projects assimilate satellite-based aerosol states, integrate them with known aerosol sources, and project their global distribution by use of atmospheric transport models.

Here we perform an exploratory study on MACC. MACC and its successor, MACC-II (MACC - Interim Implementation), are EU funded funded projects which deliver quality-assessed data on atmospheric composition. MACC'II routinely runs a NRT data assimilation and forecasting system. A 4D-Var data assimilation system is used to produce global reanalysis, whose data can be downloaded from the ECMWF Data Server. Observations of the current state of the atmosphere are combined with a numerical forecast model to produce an analysis, which gives the best estimate of the current state of the atmosphere. The resolution of the standard near real time (NRT) MACC reanalysis is T255 L60 (approximately 80 km on 60 vertical levels). However, the Chemical Aspects Section of the ECMWF also generates higher resolution data T511 L60 (approximately 40 km) in delayed-mode. These data are still not available for download from the ECMWF archive, however a limited dataset was personally communicated to the author by the model developers.

Daily averages of MACC AOD were compared to the other data sources included in this study, i.e. AERONET, MODIS and the Kinne climatological data, at the site of Bolzano, in August 2011 (Figure 8.9). The results of this analysis are not very encouraging, because MACC data underestimate daily AOD. If we take AERONET AOD as reference, MACC reproduces the low values with a good approximation, but is far from the high values.

In order to quantify the eventual error deriving from using MACC data in HelioMont, we performed RTM simulations of irradiance components with the

same configuration used for AERONET and MODIS data (Figure 8.10). We found that the error is close to the one produced by MODIS (MAB=25 Wm^{-2}, MBD=-10 Wm^{-2}), and much lower than the error of HelioMont based on climatological data.

In conclusion, MACC data could allow a better estimation of direct and diffuse radiation compared to climatological data.
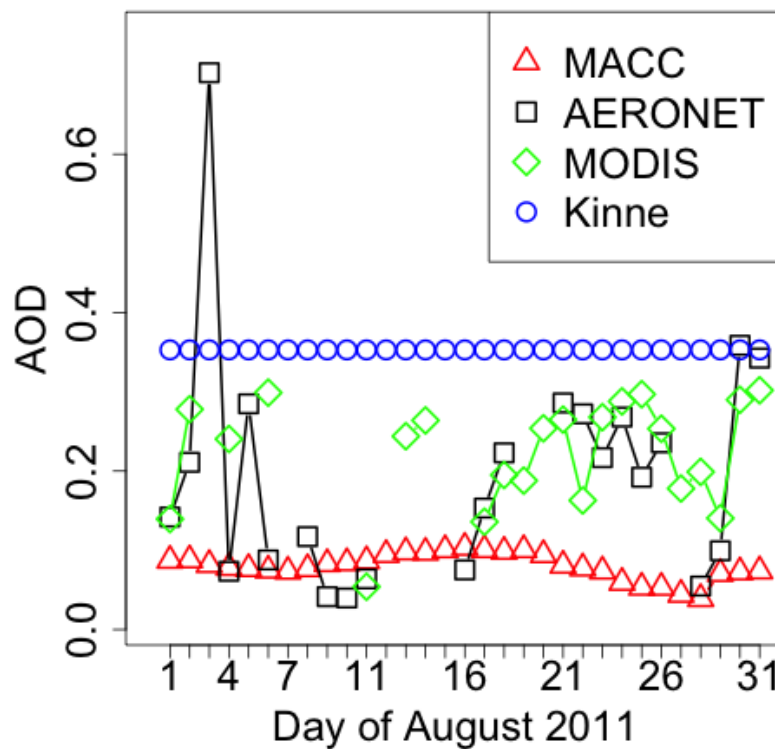
Figure 8.9: Comparison between daily AOD values obtained by different models and measurement instruments at Bolzano, during August 2011. For AERONET and MACC data, daily averages were computed from the original dataset, while MODIS data are available daily, and the Kinne database includes monthly climatologies.

8.6   Conclusions

This study examined the performance of the HelioMont algorithm for estimating solar radiation from MSG data in complex terrain. The validation employs ground-based measurements collected at three alpine sites, namely Bolzano, Davos and
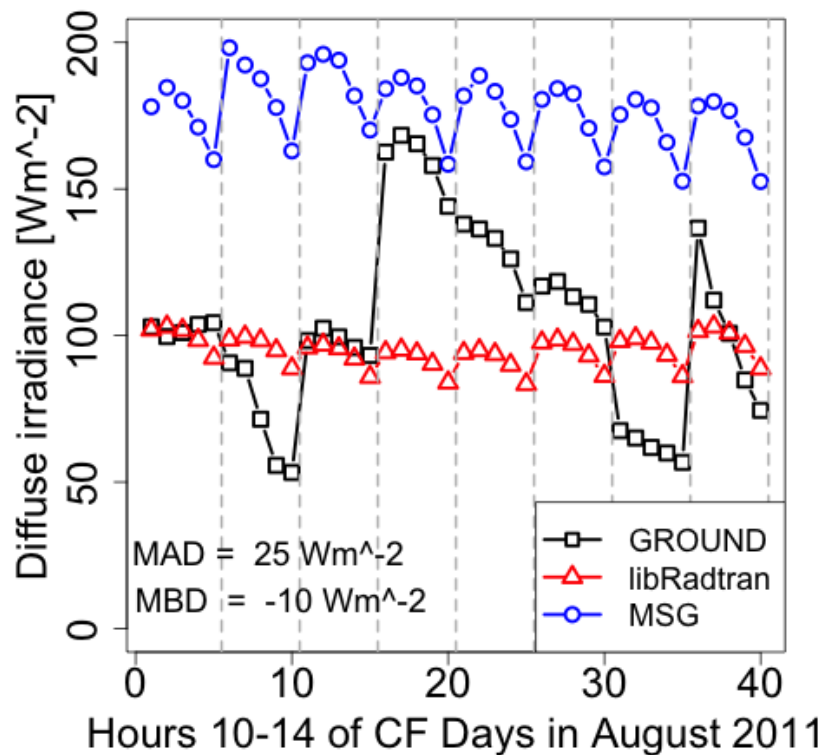
Figure 8.10: Comparison between hourly averages of diffuse irradiance simulated by libRadtran with MACC aerosol data, estimated by HelioMont, and measured by ground-based instruments.

Payerne. The first two lie on a valley floor, and both are surrounded by a steep orography. The first is at low altitude, the second at high altitude. The third station is located on the Swiss Main Plateau. We analyzed the performance of the algorithm for different time scales, seasons and sky conditions in order to isolate specific drivers for the major remaining error sources.

The validation demonstrates that the algorithm is able to provide monthly climatologies of both global irradiance and its components over complex terrain. In addition the use of a cloud index based on the SEVIRI HRV channel, as well as its subsequent extension with near-infrared and infrared channels over bright snow surfaces, provides a realistic radiative cloud forcing for the three sites of interest as already shown by Stöckli, 2013a. However the estimation of the diffuse and direct components of irradiance at daily and hourly time scale is associated with

considerable error. This problem is most prominent under clear-sky conditions, during summer-time, in the central hours of the day. In conclusion, the satellite algorithm overestimates atmospheric diffusivity, which in clear-sky conditions is mainly due to Mie scattering by aerosols and reflection by the Earth surface.

The clear-sky scheme of the satellite algorithm is driven with a monthly $1°$ x $1°$ climatology of aerosol distribution in the atmosphere. This external boundary condition offers a rather inadequate representation, both in spatial and in temporal resolution, of the real conditions occurring in alpine valleys. To envisage how the estimation of the irradiance components can be improved, we used daily averages of accurate aerosol and water vapor data, available from the AERONET stations of Bolzano and Davos. For each station we selected the month with the highest number of cloud free days and simulated the corresponding radiation by the RTM libRadtran, the same used in the satellite algorithm, also considering the sky view factor. Therefore we compared hourly averages of simulated, measured and estimated diffuse irradiance. The low values of MBD and MAB between RTM simulations and ground measurements, compared to the strong overestimation of satellite data, confirmed that model performance would benefit from more accurate local-scale aerosol boundary conditions.

AERONET stations give very accurate information on aerosols, but are sparsely distributed all over the world. Consequently it is crucial to rely on other sources of data. The easiest choice is using satellite data. This option was tested in Bolzano running RTM simulations using MODIS AOT, OMI SSA and ERA Interim water vapor column amount. MAB duplicated compared to AERONET, but was still much lower than in satellite estimations. MACC re-analysis data were also tested, and showed performances similar to the ones of MODIS, with the advantages of no gaps in the data. It can be concluded that despite having a reliable cloud forcing when deriving solar radiation from satellite data, there is room for improving such estimates by optimizing the prescribed atmospheric state under clear-sky conditions.

One option would be to use daily satellite-based aerosol maps. Known limitations of this method include the high retrieval errors of AOT over land with associated gaps in the dataset over regions with bright surfaces and cloud cover. Specifically non-vegetated mountainous regions with snow cover are often not sufficiently covered by satellite-based aerosol datasets. Nevertheless this choice is promising considering the availability of the new MODIS high resolution (1 km) AOT product obtained with the algorithm MAIAC (Multi-Angle Implementation of Atmospheric Correction) (Emili et al., 2011a; Lyapustin et al., 2012). Another option could be that of integrating satellite and in-situ measurements Emili et al., 2011b in order to reduce the uncertainty in satellite retrieval of AOT.

8.7   Outlook

The proposed integration of surface aerosol measurements with satellite measurements enhances the applicability of satellite data and is more valuable than the analysis of single isolated stations or station networks Grigiante et al., 2011. The resulting method improves the reliability and precision of solar radiation estimates over complex terrain, which is a key requirement for applications pertaining both to short-term weather forecasting, and to long-term climatological assessment of available radiation.

One example of such an application is the mitigation of one main weakness of technologies based on solar energy, like PV and CSP, i.e. the fluctuating nature of the solar resource and its poor predictability. An accurate solar radiation estimate is useful for solar energy assessments since it supports decision-making in both the private and public sector, e.g. in building solar atlases, defining suitable plant locations, calculating the return of the investments, assessing the solar energy potential and the energetic scenario of a region.

Agriculture and forest management are other examples of fields where such valuable information is required. Furthermore in the mountains incoming short-

wave radiation is also the main driver of a number of typical atmospheric boundary-layer processes Rotach and Zardi, 2007, especially in connection with the development of thermally driven winds along the inclines and the valleys Serafin and Zardi, 2010a,b, 2011. The latter are key factors for the assessment of air quality in mountain valleys, where pollutants may arise from the main traffic corridors de Franceschi and Zardi, 2009, as well as from major plants, such as waste incinerators Ragazzi et al., 2013.

Chapter 9

Conclusions and outlook

9.1 Achievements

This thesis examines various methods for estimating spatially distributed solar radiation and its diffuse/direct components at the Earth's surface. The study area is South Tyrol, an alpine region characterized by complex terrain, which is poorly equipped with ground-based instruments measuring irradiance components.

We started, in Chapter 3, by collecting data from the meteorological stations of the Province of Bolzano. Since a proper maintenance procedure is not applied to these stations, old data were excluded, and only stations installed after 2009 were included in the study, assuming a limited instrumental drift from the calibration curve. By analyzing the spatial distribution of the instruments we deduced that an interpolation based on geostatistical methods is not feasible, because distances are much longer than the spatial autocorrelation of solar radiation in complex terrain. Consequently other approaches have to be exploited, like satellite-based algorithms, which are the subject of Chapters 7 and 8.

Since none of the stations of the Province of Bolzano measures irradiance components, in Chapter 4 we tested three kinds of decomposition methods, i.e. models which decompose solar radiation in the direct and diffuse fraction: the piecewise

regression of Reindl-Helbig, the BRL logistic function, and a model based on artificial neural networks (ANN). The first two models resulted inaccurate in our study-area, thus we developed two models specifically tuned with the data of three alpine stations which measure diffuse irradiance, i.e. Bolzano, Davos and Payerne. First we fitted a specific logistic function from alpine data. This function allows to estimate the diffuse component with MAB $\in$ [25, 51] Wm^{-2} and MBD $\in$ [-17, 1] Wm^{-2}. Second, we developed two neural networks: the first one with meteorological input data collected at the station of Payerne, and the second with the same input features as the predictors of the logistic model, including data from three alpine stations. The first ANN estimates diffuse irradiance with MAB $\in$ [33, 50] Wm^{-2} and MBD $\in$ [-6, -10] Wm^{-2}, and the second ANN with MAB $\in$ [32, 43] Wm^{-2} and MBD $\in$ [-7, -25] Wm^{-2}. In conclusion, both ANN and the logistic function can be exploited for estimating radiation components with acceptable error at stations measuring global radiation.

After having inspected data-driven approaches for estimating radiation components, in Chapter 5 and 6 we considered a physically based model, i.e. a radiative transfer model (RTM), which numerically solves the equation of radiative transfer. As a local scale application, by the RTM libRadtran we modeled the radiative forcing and heating rate of black carbon aerosol vertical profiles measured over three Italian basin valleys (Merano, Terni and Milano) (Ferrero et al., 2014). The quality of the data and the flexibility of the RTM model allowed to estimate aerosol absorption and scattering along height, and also its influence on the thermal structure of the atmosphere.

RTMs are also employed in satellite-based algorithms (described in Chapter 7) for retrieving spatially distributed irradiance. In Chapter 8 we validated the model HelioMont, a successor of Heliosat, which derives solar radiation from Meteosat data in mountainous regions (Castelli et al., 2014). The clear-sky scheme of HelioMont exploits the RTM libRadtran for modeling atmospheric extinction by aerosols and gases. The validation demonstrates that the algorithm is able to

provide monthly climatologies of both global irradiance and its components over complex terrain, and reproduces a realistic radiative cloud forcing. However the estimation of the diffuse and direct components of irradiance on daily and hourly time scale is associated with considerable error. In fact, the satellite algorithm overestimates atmospheric diffusivity, which in clear-sky conditions is mainly due to Mie scattering by aerosols and reflection by the Earth's surface, and underestimates atmospheric absorption by aerosols and water vapor. These problems are caused by the use of a monthly $1° \times 1°$ climatology of aerosol in the clear-sky scheme. We simulated irradiance components with the same RTM as HelioMont, with local inputs from AERONET and satellite input from MODIS, and we obtained very good results. However, AERONET stations are sparsely distributed, and MODIS data are affected by many gaps, especially in mountainous regions. As an alternative, we tested the aerosol data of the MACC re-analysis, with daily coverage. Results were similar to the ones obtained with MODIS. In conclusion, there is room for improving irradiance estimates by optimizing the prescribed atmospheric state under clear-sky conditions.

9.2   Outlook

The results achieved in this thesis will be exploited in two main fields. The first regards technologies converting solar energy into electric power. The assessment of the available solar resource and of its direct and diffuse components, combined with the knowledge of the performance of different solar technologies, will allow to choose the best performing devices for a certain area. This means optimizing the design of PV and CSP plants for exploiting solar energy in the most efficient way.

The second field of application involves the assessment and modeling of water and carbon exchanges between the biosphere and the atmosphere. Radiation dataset examined and developed in this thesis will be exploited for modeling spatially distributed and local scale photosynthesis and evapotranspiration in the

alpine region. The quantification of these fluxes is essential for many applications, like drought monitoring, water resources management and hydrological decision support. Furthermore it will be possible to investigate the sensitivity of these fluxes to climate change, especially focusing on observed and expected changes in solar radiation and on the relative fraction of diffuse and direct radiation, which is dependent on cloud cover and atmospheric aerosol loads.

Bibliography

Bibliography

EUMETSAT - Meteosat First Generation. `http://www.eumetsat.int/website/home/Satellites/PastSatellites/index.html`, www.

EUMETSAT - Meteosat Third Generation. `http://www.eumetsat.int/website/home/Satellites/FutureSatellites/MeteosatThirdGeneration/index.html`, www.

EUMETSAT - Meteosat Second Generation. `http://www.eumetsat.int/website/home/Satellites/CurrentSatellites/Meteosat/index.html`, www.

T.P. Ackerman and O.B. Toon. Absorption of visible radiation in atmosphere containing mixtures of absorbing and nonabsorbing particles. *Applied Optics*, 20(20):3661–3667, 1981.

E.A. Alsema, M.J. de Wild-Scholten, and V.M. Fthenakis. Environmental impacts of PV electricity generation-a critical comparison of energy supply options. In *21st European photovoltaic solar energy conference, Dresden, Germany*, volume 3201, 2006.

G.P. Anderson, S.A. Clough, F.X. Kneizys, J.H. Chetwynd, and E.P. Shettle. Afgl atmospheric constituent profiles (0.120 km). Technical report, DTIC Document, 1986.

M.C. Anderson, W.P. Kustas, J.M. Norman, C.R. Hain, J.R. Mecikalski, L. Schultz, M.P. González-Dugo, C. Cammalleri, G. d'Urso, A. Pimstein, et al.

Mapping daily evapotranspiration at field to continental scales using geostationary and polar orbiting satellite imagery. *Hydrology and Earth System Sciences*, 15(1):223–239, 2011.

F. Angelini, F. Barnaba, T.C. Landi, L. Caporaso, and G.P. Gobbi. Study of atmospheric aerosols and mixing layer by LIDAR. *Radiation protection dosimetry*, 137(3-4):275–279, 2009.

W.P. Arnott, K. Hamasha, H. Moosmüller, P.J. Sheridan, and J.A. Ogren. Towards aerosol light-absorption measurements with a 7-wavelength aethalometer: Evaluation with a photoacoustic instrument and 3-wavelength nephelometer. *Aerosol Science and Technology*, 39(1):17–29, 2005.

D.E. Aspnes. Local-field effects and effective-medium theory: A microscopic perspective. *Am. J. Phys*, 50(8), 1982.

S.S. Babu, V. Sreekanth, K.K. Moorthy, M. Mohan, N.V.P. Kirankumar, D.B. Subrahamanyam, M.M. Gogoi, S.K. Kompalli, N. Beegum, J.P. Chaubey, et al. Vertical profiles of aerosol black carbon in the atmospheric boundary layer over a tropical coastal station: Perturbations during an annular solar eclipse. *Atmospheric Research*, 99(3):471–478, 2011.

G.D. Barber, P.G. Hoertz, S.-H.A. Lee, N. Abrams, J. Mikulca, T.E. Mallouk, P. Liska, S.M. Zakeeruddin, M. Grätzel, A. Ho-Baillie, and M.A. Green. Utilization of direct and diffuse sunlight in a dye-sensitized solar cell - silicon photovoltaic hybrid concentrator system. *The Journal of Physical Chemistry Letters*, 2(6):581–585, 2011.

J. Betcke, R. Kuhlemann, A. Hammer, A. Drews, E. Lorenz, M. Girodo, D. Heinemann, L. Wald, S. Cros, M. Schroedter-Homscheidt, et al. Final report of the HELIOSAT-3 project. 2006.

H.G. Beyer, C. Costanzo, and D. Heinemann. Modifications of the Heliosat procedure for irradiance estimates from satellite images. *Solar Energy*, 56(3):207–212, 1996.

C.F. Bohren and D.R. Huffman. Absorption and scattering by a sphere. *Absorption and Scattering of Light by Small Particles*, pages 82–129, 1983.

J. Boland, J. Huang, and B. Ridley. Decomposing global solar radiation into its direct and diffuse components. *Renewable and Sustainable Energy Reviews*, 28: 749–756, 2013.

G. B. Bonan. *Ecological climatology: concepts and applications.* Cambridge University Press, 2002.

T.C. Bond and R.W. Bergstrom. Light absorption by carbonaceous particles: An investigative review. *Aerosol science and technology*, 40(1):27–67, 2006.

T.C. Bond, S.J. Doherty, D.W. Fahey, P.M. Forster, T. Berntsen, B.J. De Angelo, M.G. Flanner, S. Ghan, B. Kärcher, D. Koch, et al. Bounding the role of black carbon in the climate system: A scientific assessment. *Journal of Geophysical Research: Atmospheres*, 118(11):5380–5552, 2013.

B. Bourges. Courbes de fréquence cumulées de l'irradiance solaire globale horaire recue par une surface plane. *Technical Report. Centre d'Energétique de l'Ecole Nationale Supérieure des Mines de Paris*, 1979.

D.A.G. Bruggeman. Calculation of various physics constants in heterogenous substances i dielectricity constants and conductivity of mixed bodies from isotropic substances. *Ann. Phys*, 24(7):636–664, 1935.

J.F. Cahill, K. Suski, J.H. Seinfeld, R.A. Zaveri, and K.A. Prather. The mixing state of carbonaceous aerosol particles in northern and southern california mea-

sured during cares and calnex 2010. *Atmospheric Chemistry and Physics*, 12 (22):10989–11002, 2012.

D. Cano, J.M. Monget, M. Albuisson, H. Guillard, N. Regas, and L. Wald. A method for the determination of the global solar radiation from meteorological satellite data. *Solar Energy*, 37(1):31–39, 1986.

J.N. Cape, M. Coyle, and P. Dumitrean. The atmospheric lifetime of black carbon. *Atmospheric Environment*, 59:256–263, 2012.

C. Carbone, S. Decesari, M. Mircea, L. Giulianelli, E. Finessi, M. Rinaldi, S. Fuzzi, A. Marinoni, R. Duchi, C. Perrino, et al. Size-resolved aerosol chemical composition over the italian peninsula during typical summer and winter conditions. *Atmospheric Environment*, 44(39):5269–5278, 2010.

D. Carrer, S. Lafont, J.-L. Roujean, J.-C. Calvet, C. Meurey, P. Le Moigne, and I.F. Trigo. Incoming solar and infrared radiation derived from METEOSAT: Impact on the modeled land water and energy budget over France. *Journal of Hydrometeorology*, 13(2):504–520, 2012.

M Castelli, R Stöckli, D Zardi, A Tetzlaff, JE Wagner, G Belluardo, M Zebisch, and M Petitta. The heliomont method for assessing solar irradiance over complex terrain: Validation and improvements. *Remote Sensing of Environment*, 152: 603–613, 2014.

R.K. Chakrabarty, M.A. Garro, E.M. Wilcox, and H. Moosmüller. Strong radiative heating due to wintertime black carbon aerosols in the brahmaputra river valley. *Geophysical Research Letters*, 39(9), 2012.

P. Chazette and C. Liousse. A case study of optical and chemical ground apportionment for urban aerosols in thessaloniki. *Atmospheric Environment*, 35(14): 2497–2506, 2001.

Y. Chen and KN Liou. A Monte Carlo method for 3d thermal infrared radiative transfer. *Journal of Quantitative Spectroscopy and Radiative Transfer*, 101(1): 166–178, 2006.

M. Chin, R.B. Rood, S.-J. Lin, J.-F. Muller, and A.M. Thompson. Atmospheric sulfur cycle simulated in the global model GOCART - Model description and global properties. *Journal of Geophysical Research*, 105(D20):24–671, 2000.

M. Chin, P. Ginoux, S. Kinne, O. Torres, B.N. Holben, B.N. Duncan, R.V. Martin, J.A. Logan, A. Higurashi, and T. Nakajima. Tropospheric aerosol optical thickness from the GOCART model and comparisons with satellite and sun photometer measurements. *Journal of the atmospheric sciences*, 59(3):461–483, 2002.

P. Chylek and J. Wong. Effect of absorbing aerosols on global radiation budget. *Geophysical Research Letters*, 22(8):929–931, 1995.

S.L. Clegg, P. Brimblecombe, and A.S. Wexler. Thermodynamic model of the system h+-nh4+-so42–no3–h2o at tropospheric temperatures. *The Journal of Physical Chemistry A*, 102(12):2137–2154, 1998.

C.E. Corrigan, G.C. Roberts, M.V. Ramana, D. Kim, and V. Ramanathan. Capturing vertical profiles of aerosols and black carbon over the indian ocean using autonomous unmanned aerial vehicles. *Atmospheric Chemistry and Physics*, 8 (3):737–747, 2008.

A.L. Crosbie and G.W. Davidson. Dirac-delta function approximations to the scattering phase function. *Journal of Quantitative Spectroscopy and Radiative Transfer*, 33(4):391–409, 1985.

S.K. Das and A. Jayaraman. Role of black carbon in aerosol properties and radiative forcing over western india during premonsoon period. *Atmospheric Research*, 102(3):320–334, 2011.

M. de Franceschi and D. Zardi. Study of wintertime high pollution episodes during the Brenner-South ALPNAP measurement campaign. *Meteorology and Atmospheric Physics*, 103(1-4):237–250, 2009.

D.P. Dee, S.M. Uppala, A.J. Simmons, P. Berrisford, P. Poli, S. Kobayashi, U. Andrae, M.A. Balmaseda, G. Balsamo, P. Bauer, et al. The ERA-Interim reanalysis: Configuration and performance of the data assimilation system. *Quarterly Journal of the Royal Meteorological Society*, 137(656):553–597, 2011.

T. Deshler, M.E. Hervig, D.J. Hofmann, J.M. Rosen, and J.B. Liley. Thirty years of in situ stratospheric aerosol size distribution measurements from laramie, wyoming (41 N), using balloon-borne instruments. *Journal of Geophysical Research: Atmospheres (1984–2012)*, 108(D5), 2003.

W. Di Nicolantonio, A. Cacciari, A. Petritoli, C. Carnevale, E. Pisoni, M.L. Volta, P. Stocchi, G. Curci, E. Bolzacchini, L. Ferrero, et al. Modis and omi satellite observations supporting air quality monitoring. *Radiation protection dosimetry*, page ncp231, 2009.

J. Dozier and D. Marks. Snow mapping and classification from landsat thematic mapper data. *Annals of Glaciology*, 9:97–103, 1987.

R. Dubayah. Estimating net solar radiation using landsat thematic mapper and digital elevation data. *Water Resources Research*, 28(9):2469–2484, 1992a. ISSN 1944-7973. doi: 10.1029/92WR00772. URL `http://dx.doi.org/10.1029/92WR00772`.

R. Dubayah. Estimating net solar radiation using Landsat Thematic Mapper and digital elevation data. *Water resources research*, 28(9):2469–2484, 1992b.

R. Dubayah and M. Paul. Topographic solar radiation models for GIS. *International Journal of Geographical Information Systems*, 9(4):405–419, 1995.

R. Dubayah and V. van Katwijk. The topographic distribution of annual incoming solar radiation in the rio grande river basin. *Geophysical Research Letters*, 19 (22):2231–2234, 1992. ISSN 1944-8007. doi: 10.1029/92GL02284. URL `http://dx.doi.org/10.1029/92GL02284`.

Ralph C. Dubayah. Modeling a solar radiation topoclimatology for the rio grande river basin. *Journal of Vegetation Science*, 5(5):627–640, 1994. ISSN 1654-1103. doi: 10.2307/3235879. URL `http://dx.doi.org/10.2307/3235879`.

D. Dumortier. Modelling global and diffuse horizontal irradiances under cloudless skies with different turbidities. *Daylight II, jou2-ct92-0144, final report vol*, 2, 1995.

B. Dürr and A. Zelenka. Deriving surface global irradiance over the alpine region from Meteosat Second Generation data by supplementing the HELIOSAT method. *International Journal of Remote Sensing*, 30(22):5821–5841, 2009.

B. Dürr, A. Zelenka, R. Müller, and R. Philipona. Verification of CM-SAF and MeteoSwiss satellite based retrievals of surface shortwave irradiance over the Alpine region. *International Journal of Remote Sensing*, 31(15):4179–4198, 2010.

EHF, UiB, and ARMINES. Report of the Heliosat-3 software package for solar irradiance retrieval, all sky working version. Deliverable D8.1 and D8.2. 2003.

H.K. Elminir, Y.A. Azzam, and F.I. Younes. Prediction of hourly and daily diffuse fraction using neural network, as compared to linear regression models. *Energy*, 32(8):1513–1523, 2007.

E. Emili, C. Popp, M. Petitta, M. Riffler, S. Wunderle, and M. Zebisch. Pm 10 remote sensing from geostationary seviri and polar-orbiting modis sensors over the complex terrain of the european alpine region. *Remote sensing of environment*, 114(11):2485–2499, 2010.

E. Emili, A. Lyapustin, Y. Wang, C. Popp, S. Korkin, M. Zebisch, S. Wunderle, and M. Petitta. High spatial resolution aerosol retrieval with MAIAC: Application to mountain regions. *Journal of Geophysical Research*, 116(D23211), 2011a. doi: 10.1029/2011JD016297.

E. Emili, C. Popp, S. Wunderle, M. Zebisch, and M. Petitta. Mapping particulate matter in alpine regions with satellite and ground-based measurements: An exploratory study for data assimilation. *Atmospheric Environment*, 45(26):4344–4353, 2011b. doi: 10.1016/j.atmosenv.2011.05.051.

L. Ferrero, M.G. Perrone, S. Petraccone, G. Sangiorgi, B.S. Ferrini, C.L. Porto, Z. Lazzati, D. Cocchi, F. Bruno, F. Greco, et al. Vertically-resolved particle size distribution within and above the mixing layer over the milan metropolitan area. *Atmospheric Chemistry and Physics*, 10(8):3915–3932, 2010.

L. Ferrero, G. Mocnik, B.S. Ferrini, M.G. Perrone, G. Sangiorgi, and E. Bolzacchini. Vertical profiles of aerosol absorption coefficient from micro-aethalometer data and mie calculation over milan. *Science of the Total Environment*, 409(14): 2824–2837, 2011a.

L. Ferrero, A. Riccio, M.G. Perrone, G. Sangiorgi, B.S. Ferrini, and E. Bolzacchini. Mixing height determination by tethered balloon-based particle soundings and modeling simulations. *Atmospheric Research*, 102(1):145–156, 2011b.

L. Ferrero, D. Cappelletti, B. Moroni, G. Sangiorgi, M.G. Perrone, S. Crocchianti, and E. Bolzacchini. Wintertime aerosol dynamics and chemical composition across the mixing layer over basin valleys. *Atmospheric Environment*, 56:143–153, 2012.

L. Ferrero, G. Sangiorgi, B.S. Ferrini, M.G. Perrone, M. Moscatelli, L. D'Angelo, G. Rovelli, A. Ariatta, R. Truccolo, and E. Bolzacchini. Aerosol corrosion pre-

vention and energy-saving strategies in the design of green data centers. *Environmental science & technology*, 47(8):3856–3864, 2013.

L. Ferrero, M. Castelli, B.S. Ferrini, M. Moscatelli, M.G. Perrone, G. Sangiorgi, L. D'Angelo, G. Rovelli, B. Moroni, F. Scardazza, et al. Impact of black carbon aerosol over italian basin valleys: high-resolution measurements along vertical profiles, radiative forcing and heating rate. *Atmospheric Chemistry and Physics*, 14(18):9641–9664, 2014.

R. Fierz-Schmidhauser, P. Zieger, M. Gysel, L. Kammermann, P.F. De Carlo, U. Baltensperger, and E. Weingartner. Measured and predicted aerosol light scattering enhancement factors at the high alpine site jungfraujoch. *Atmospheric Chemistry and Physics*, 10(5):2319–2333, 2010.

F. Fontana, R. Stöckli, and S. Wunderle. SPARC: a new scene identification algorithm for MSG SEVIRI. Report on modifications and validation. Visiting scientist report., EUMETSAT Satellite Application Facility on Climate Monitoring, 2010.

M. Grigiante, F. Mottes, D. Zardi, and M. De Franceschi. Experimental solar radiation measurements and their effectiveness in setting up a real-sky irradiance model. *Renewable Energy*, 36(1):1–8, 2011.

P.l. Guyon, O. Boucher, B. Graham, J. Beck, O.L. Mayol-Bracero, G.C. Roberts, W. Maenhaut, P. Artaxo, and M.O. Andreae. Refractive index of aerosol particles over the amazon tropical forest during lba-eustach 1999. *Journal of Aerosol Science*, 34(7):883–907, 2003.

A. Hammer, D. Heinemann, C. Hoyer, R. Kuhlemann, E. Lorenz, R. Müller, and H.G. Beyer. Solar energy assessment using remote sensing technologies. *Remote Sensing of Environment*, 86(3):423–432, 2003.

C.L. Heald, D.A. Ridley, J.H. Kroll, S.R.H. Barrett, K.E. Cady-Pereira, M.J. Alvarado, and C.D. Holmes. Contrasting the direct radiative effect and direct radiative forcing of aerosols. *Atmospheric Chemistry and Physics*, 14(11):5513–5527, 2014.

M. Heim, B.J. Mullins, H. Umhauer, and G. Kasper. Performance evaluation of three optical particle counters with an efficient "multimodal" calibration method. *Journal of aerosol science*, 39(12):1019–1031, 2008.

N. Helbig. *Application of the radiosity approach to ther adiation balance in complex terrain*. PhD thesis, Mathematisch-naturwissenschaftlichen Fakultät der Universität Zürich, PhD thesis presented by Nora Helbig, 2010, Supervisor: Dr Wilfried Haeberli, 2009.

N. Helbig, H. Löwe, and M. Lehning. Radiosity approach for the shortwave surface radiation balance in complex terrain. *Journal of the Atmospheric Sciences*, 66 (9):2900–2912, 2009.

N. Helbig, H. Löwe, B. Mayer, and M. Lehning. Explicit validation of a surface shortwave radiation balance model over snow-covered complex terrain. *Journal of Geophysical Research: Atmospheres (1984–2012)*, 115(D18), 2010.

W. Heller. Remarks on refractive index mixture rules. *The Journal of Physical Chemistry*, 69(4):1123–1129, 1965.

M. Hess, P. Koepke, and I. Schult. Optical properties of aerosols and clouds: The software package opac. *Bulletin of the American meteorological society*, 79(5): 831–844, 1998.

J. Heyder and J. Gebhart. Optimization of response functions of light scattering instruments for size evaluation of aerosol particles. *Applied optics*, 18(5):705–711, 1979.

J. Hofierka and M. Šúri. The solar radiation model for open source gis: implementation and applications. *Proceedings of the open souce GIS - GRASS users conference. Trento, Italy, 11-13 September 2002*, pages 1–19, 2002. doi: 10.1.1.19.9831.

B.N. Holben, T.F. Eck, I. Slutsker, D. Tanre, J.P. Buis, A. Setzer, E. Vermote, J.A. Reagan, Y.J. Kaufman, T. Nakajima, et al. AERONET-a federated instrument network and data archive for aerosol characterization. *Remote sensing of environment*, 66(1):1–16, 1998.

S.G. Howell, A.D. Clarke, Y. Shinozuka, V. Kapustin, C.S. McNaughton, B.J. Huebert, S.J. Doherty, and T.L. Anderson. Influence of relative humidity upon pollution and dust during ace-asia: Size distributions and implications for optical properties. *Journal of Geophysical Research: Atmospheres (1984–2012)*, 111 (D6), 2006.

Christoph Hueglin, Robert Gehrig, Urs Baltensperger, Martin Gysel, Christian Monn, and Heinz Vonmont. Chemical characterisation of pm2. 5, pm10 and coarse particles at urban, near-city and rural sites in switzerland. *Atmospheric Environment*, 39(4):637–651, 2005.

P. Ineichen. Comparison of eight clear sky broadband models against 16 independent data banks. *Solar Energy*, 80(4):468–478, 2006.

P. Ineichen, C.S. Barroso, B. Geiger, R. Hollmann, A. Marsouin, and R. Mueller. Satellite Application Facilities irradiance products: hourly time step comparison and validation over Europe. *International Journal of Remote Sensing*, 30(21): 5549–5571, 2009.

A. Inness, F. Baier, A. Benedetti, I. Bouarar, S. Chabrillat, H. Clark, C. Clerbaux, P. Coheur, R. J. Engelen, Q. Errera, J. Flemming, M. George, C. Granier,

J. Hadji-Lazaro, V. Huijnen, D. Hurtmans, L. Jones, J. W. Kaiser, J. Kapsome-nakis, K. Lefever, J. Leitão, M. Razinger, A. Richter, M. G. Schultz, A. J. Simmons, M. Suttie, O. Stein, J.-N. Thépaut, V. Thouret, M. Vrekoussis, C. Zerefos, and the MACC team. The MACC reanalysis: an 8-yr data set of atmospheric composition. *Atmospheric Chemistry and Physics Discussions*, 12(12):31247–31347, 2012.

M.Z. Jacobson. Strong radiative heating due to the mixing state of black carbon in atmospheric aerosols. *Nature*, 409(6821):695–697, 2001.

C.P. Jacovides, F.S. Tymvios, V.D. Assimakopoulos, and N.A. Kaltsounides. Comparative study of various correlations in estimating hourly diffuse fraction of global solar radiation. *Renewable Energy*, 31(15):2492–2504, 2006.

M. Journée and C. Bertrand. Improving the spatio-temporal distribution of surface solar radiation data by merging ground and satellite measurements. *Remote Sensing of Environment*, 114(11):2692–2704, 2010.

A.S. Kassem, A.M. Aboukarima, and N.M. El Ashmawy. Development of neural network model to estimate hourly total and diffuse solar radiation on horizontal surface at alexandria city (egypt). *J. Appl. Sci. Res*, 5(11):2006–2015, 2009.

F. Kasten. The linke turbidity factor based on improved values of the integral rayleigh optical thickness. *Solar Energy*, 56(3):239 – 244, 1996. ISSN 0038-092X. doi: http://dx.doi.org/10.1016/0038-092X(95)00114-7. URL `http://www.sciencedirect.com/science/article/pii/0038092X95001147`.

F. Kasten, K. Dehne, H.D. Behr, and D. Bergholter. Spatial and temporal distribution of diffuse and direct solar radiation in Germany. Research Report N. 84., German Federal Ministry of Research and Technology, 1984.

S. Kato, T.P. Ackerman, J.H. Mather, and E.E. Clothiaux. The k–distribution method and correlated–k approximation for a shortwave radiative transfer

model. *Journal of Quantitative Spectroscopy and Radiative Transfer*, 62(1): 109–121, 1999.

Y.J. Kaufman, D. Tanré, and O. Boucher. A satellite view of aerosols in the climate system. *Nature*, 419(6903):215–223, 2002.

N.D. Kaushika, R.K. Tomar, and S.C. Kaushik. Artificial neural network model based on interrelationship of direct, diffuse and global solar radiations. *Solar Energy*, 103(0):327 – 342, 2014. ISSN 0038-092X. doi: http://dx.doi.org/10. 1016/j.solener.2014.02.015. URL `http://www.sciencedirect.com/science/article/pii/S0038092X14000930`.

S. Kedia, S. Ramachandran, A. Kumar, and M.M. Sarin. Spatiotemporal gradients in aerosol radiative forcing and heating rate over bay of bengal and arabian sea derived on the basis of optical, physical, and chemical properties. *Journal of Geophysical Research: Atmospheres (1984–2012)*, 115(D7), 2010.

K.V. Khlopenkov and A.P. Trishchenko. Sparc: new cloud, snow, and cloud shadow detection scheme for historical 1-km avhhr data over canada. *Journal of Atmospheric and Oceanic technology*, 24(3):322–343, 2007.

S. Kinne. *Clouds in the perturbed climate system*, chapter Climatologies of cloud related aerosols: Particle number and size. MIT Press, 2008. ISBN 978-0-262-01287-4.

Kipp&Zonen. *CHP 1 Pyrheliometer Instruction Manual*. Kipp&Zonen, 2008.

Kipp&Zonen. *CMP series Pyranometer and CMA series Albedometer Instruction Manual*. Kipp&Zonen, 2013.

I. Koren, Y.J. Kaufman, L.A. Remer, and J.V. Martins. Measurement of the effect of amazon smoke on inhibition of cloud formation. *Science*, 303(5662): 1342–1345, 2004.

I. Koren, J.V. Martins, L.A. Remer, and H. Afargan. Smoke invigoration versus inhibition of clouds over the amazon. *science*, 321(5891):946–949, 2008.

S.Y. Kotchenova, E.F. Vermote, R. Matarrese, F.J. Klemm Jr, et al. Validation of a vector version of the 6S radiative transfer code for atmospheric correction of satellite data. part I: Path radiance. *Applied Optics*, 45(26):6762–6774, 2006.

P. Kulkarni, P.A. Baron, and K. Willeke. *Aerosol measurement: principles, techniques, and applications.* John Wiley & Sons, 2011.

F. Lanini. *Division of global radiation into direct radiation and diffuse radiation.* PhD thesis, Master's thesis Faculty of Science University of Bern presented by Fabienne Lanini, 2010, Supervisor: Dr Stefan Wunderle Institute of Geography, University of Bern, 2010.

W.L. Lee, K.N. Liou, and A. Hall. Parameterization of solar fluxes over mountain surfaces for application to climate models. *Journal of Geophysical Research*, 116 (D01101), 2011. doi: 10.1029/2010JD014722.

G. Lesins, P. Chylek, and U. Lohmann. A study of internal and external mixing scenarios and its effect on aerosol optical properties and direct radiative forcing. *Journal of Geophysical Research: Atmospheres (1984–2012)*, 107(D10):AAC–5, 2002.

R.C. Levy, L.A. Remer, S. Mattoo, E.F. Vermote, and Y.J. Kaufman. Second-generation operational algorithm: Retrieval of aerosol properties over land from inversion of moderate resolution imaging spectroradiometer spectral reflectance. *Journal of Geophysical Research*, 112(D13211), 2007. doi: 10.1029/2006JD007811.

Kuo-Nan Liou. *An introduction to atmospheric radiation*, volume 84. Academic press, 2002.

B.Y.H. Liu and R.C. Jordan. The interrelationship and characteristic distribution of direct, diffuse and total solar radiation. *Solar energy*, 4(3):1–19, 1960.

Q. Liu and F. Weng. Advanced doubling-adding method for radiative transfer in planetary atmospheres. *Journal of the atmospheric sciences*, 63(12):3459–3465, 2006.

Y. Liu and P.H. Daum. Relationship of refractive index to mass density and self-consistency of mixing rules for multicomponent mixtures like ambient aerosols. *Journal of Aerosol Science*, 39(11):974–986, 2008.

A. Lyapustin, Y. Wang, I. Laszlo, and S. Korkin. Improved cloud and snow screening in MAIAC aerosol retrievals using spectral and spatial analysis. *Atmospheric Measurement Techniques*, 5:843–850, 2012.

X. Ma, J.Q. Lu, R.S. Brock, K.M. Jacobs, P. Yang, and X.-H. Hu. Determination of complex refractive index of polystyrene microspheres from 370 to 1610 nm. *Physics in medicine and biology*, 48(24):4165, 2003.

A. Maletto, I.G. McKendry, and K.B. Strawbridge. Profiles of particulate matter size distributions using a balloon-borne lightweight aerosol spectrometer in the planetary boundary layer. *Atmospheric Environment*, 37(5):661–670, 2003.

S.T. Martin. Phase transitions of aqueous atmospheric particles. *Chemical Reviews*, 100(9):3403–3454, 2000.

M. Matricardi, F. Chevallier, and S. Tjemkes. *An improved general fast radiative transfer model for the assimilation of radiance observations.* European Centre for Medium-Range Weather Forecasts, 2001.

E.L. Maxwell. A quasi-physical model for converting hourly global horizontal to direct normal insolation. Technical report, Solar Energy Research Inst., Golden, CO (USA), 1987.

B. Mayer and A. Kylling. Technical note: The libradtran software package for radiative transfer calculations - description and examples of use. *Atmospheric Chemistry and Physics*, 5(7):1855–1877, 2005. doi: 10.5194/acp-5-1855-2005. URL `http://www.atmos-chem-phys.net/5/1855/2005/`.

B. Mayer, A. Kylling, et al. Technical note: The libRadtran software package for radiative transfer calculations: description and examples of use. *Atmospheric Chemistry and Physics Discussions*, 5(2):1319–1381, 2005.

G.R. McMeeking, T. Hamburger, D. Liu, M. Flynn, W.T. Morgan, M. Northway, E.J. Highwood, R. Krejci, J.D. Allan, A. Minikin, et al. Black carbon measurements in the boundary layer over western and northern europe. *Atmospheric Chemistry and Physics*, 10(19):9393–9414, 2010.

G.R. McMeeking, W.T. Morgan, M. Flynn, E.J. Highwood, K. Turnbull, J. Haywood, and H. Coe. Black carbon aerosol mixing state, organic aerosols and aerosol optical properties over the united kingdom. *Atmospheric Chemistry and Physics*, 11(17):9037–9052, 2011.

P. Minnis, K.N. Liou, and Y. Takano. Inference of cirrus cloud properties using satellite-observed visible and infrared radiances. part I: Parameterization of radiance fields. *Journal of the atmospheric sciences*, 50(9):1279–1304, 1993.

W.T. Morgan, J.D. Allan, K.N. Bower, G. Capes, J. Crosier, P.I. Williams, and H. Coe. Vertical distribution of sub-micron aerosol chemical composition from north-western europe and the north-east atlantic. *Atmospheric Chemistry and Physics*, 9(15):5389–5401, 2009.

W.T. Morgan, J.D. Allan, K.N. Bower, E.J. Highwood, D. Liu, G.R. McMeeking, M.J. Northway, P.I. Williams, R. Krejci, and H. Coe. Airborne measurements of the spatial distribution of aerosol chemical composition across europe and

evolution of the organic fraction. *Atmospheric Chemistry and Physics*, 10(8): 4065–4083, 2010.

B. Moroni, D. Cappelletti, F. Marmottini, F. Scardazza, L. Ferrero, and E. Bolzacchini. Integrated single particle-bulk chemical approach for the characterization of local and long range sources of particulate pollutants. *Atmospheric Environment*, 50:267–277, 2012.

B. Moroni, L. Ferrero, S. Crocchianti, M.G. Perrone, G. Sangiorgi, E. Bolzacchini, and D. Cappelletti. Aerosol dynamics upon terni basin (central italy): results of integrated vertical profile measurements and electron microscopy analyses. *Rendiconti Lincei*, 24(4):319–328, 2013.

R.W. Müller, K.F. Dagestad, P. Ineichen, M. Schroedter-Homscheidt, S. Cros, D. Dumortier, R. Kuhlemann, J.A. Olseth, G. Piernavieja, C. Reise, et al. Rethinking satellite-based solar irradiance modelling: The SOLIS clear-sky module. *Remote Sensing of Environment*, 91(2):160–174, 2004.

R.W. Müller, C. Matsoukas, A. Gratzki, H.D. Behr, and R. Hollmann. The CM-SAF operational scheme for the satellite based retrieval of solar surface irradiance–A LUT based eigenvector hybrid approach. *Remote Sensing of Environment*, 113(5):1012–1024, 2009.

J.D. Olden, M.K. Joy, and R.G. Death. An accurate comparison of methods for quantifying variable importance in artificial neural networks using simulated data. *Ecological Modelling*, 178(3):389–397, 2004.

A.J. Oliphant, R.A. Spronken-Smith, A.P. Sturman, and I.F. Owens. Spatial variability of surface radiation fluxes in mountainous terrain. *Journal of Applied Meteorology*, 42(1):113–128, 2003.

J. Page. Algorithms for the Satellight programme. *Technical Report*, 1996.

R.K. Pathak, P.K.K. Louie, and C.K. Chan. Characteristics of aerosol acidity in hong kong. *Atmospheric Environment*, 38(19):2965–2974, 2004.

J.P. Peixoto and Abraham H. Oort. Physics of climate, 520 pp. *Am. Inst. of Phys., New York*, 1992.

R. Perez, P. Ineichen, R. Seals, and A. Zelenka. Making full use of the clearness index for parameterizing hourly insolation conditions. *Solar Energy*, 45(2):111–114, 1990.

M.G. Perrone, M. Gualtieri, L. Ferrero, C.L. Porto, R. Udisti, E. Bolzacchini, and M. Camatini. Seasonal variations in chemical composition and in vitro biological effects of fine pm from milan. *Chemosphere*, 78(11):1368–1377, 2010.

M.G. Perrone, B.R. Larsen, L. Ferrero, G. Sangiorgi, G. De Gennaro, R. Udisti, R. Zangrando, A. Gambaro, and E. Bolzacchini. Sources of high pm2. 5 concentrations in milan, northern italy: molecular marker data and cmb modelling. *Science of the total environment*, 414:343–355, 2012.

M.G. Perrone, M. Gualtieri, V. Consonni, L. Ferrero, G. Sangiorgi, E. Longhin, D. Ballabio, E. Bolzacchini, and M. Camatini. Particle size, chemical composition, seasons of the year and urban, rural or remote site origins as determinants of biological effects of particulate matter on pulmonary cells. *Environmental Pollution*, 176:215–227, 2013.

M.R. Perrone and A. Bergamo. Direct radiative forcing during sahara dust intrusions at a site in the central mediterranean: Anthropogenic particle contribution. *Atmospheric Research*, 101(3):783–798, 2011.

P. Pesava, H. Horvath, and M. Kasahara. A local optical closure experiment in vienna. *Journal of Aerosol Science*, 32(11):1249–1267, 2001.

S.r Potukuchi and A.S. Wexler. Identifying solid-aqueous phase transitions in atmospheric aerosols- i. neutral acidity solutions. *Atmospheric Environment*, 29 (14):1663–1676, 1995.

M. Ragazzi, W. Tirler, G. Angelucci, D. Zardi, and E.C. Rada. Management of atmospheric pollutants from waste incineration processes: the case of Bozen. *Waste Management & Research*, 31(3):235–240, 2013.

H. Rahman, B. Pinty, and M.M. Verstraete. Coupled surface-atmosphere reflectance (csar) model: 2. semiempirical surface model usable with noaa advanced very high resolution radiometer data. *Journal of Geophysical Research: Atmospheres (1984–2012)*, 98(D11):20791–20801, 1993.

M.V. Ramana, V. Ramanathan, D. Kim, G.C. Roberts, and C.E. Corrigan. Albedo, atmospheric solar absorption and heating rate measurements with stacked uavs. *Quarterly Journal of the Royal Meteorological Society*, 133(629): 1913–1931, 2007.

M.V. Ramana, V. Ramanathan, Y. Feng, S.C. Yoon, S.W. Kim, G.R. Carmichael, and J.J. Schauer. Warming influenced by the ratio of black carbon to sulphate and the black-carbon source. *Nature Geoscience*, 3(8):542–545, 2010.

V. Ramanathan and G. Carmichael. Global and regional climate changes due to black carbon. *Nature geoscience*, 1(4):221–227, 2008.

V. Ramanathan and Y. Feng. Air pollution, greenhouse gases and climate change: Global and regional perspectives. *Atmospheric Environment*, 43(1):37–50, 2009.

H. Randriamiarisoa, P. Chazette, P. Couvert, J. Sanak, and G. Mégie. Relative humidity impact on aerosol parameters in a paris suburban area. *Atmospheric Chemistry and Physics*, 6(5):1389–1407, 2006.

J.-C. Raut and P. Chazette. Vertical profiles of urban aerosol complex refractive index in the frame of esquif airborne measurements. *Atmospheric Chemistry and Physics*, 8(4):901–919, 2008.

S.L. Rees, A.L. Robinson, A. Khlystov, C.O. Stanier, and S.N. Pandis. Mass balance closure and the federal reference method for pm 2.5 in pittsburgh, pennsylvania. *Atmospheric Environment*, 38(20):3305–3318, 2004.

D.T. Reindl, W.A. Beckman, and J.A. Duffie. Diffuse fraction correlations. *Solar energy*, 45(1):1–7, 1990.

J. Remund, L. Wald, M. Lefèvre, T. Ranchin, and J. Page. Worldwide Linke turbidity information. In *Proceedings of ISES Solar World Congress 2003*, volume 400, 2003.

P. Ricchiazzi, S. Yang, C. Gautier, and D. Sowle. SBDART: a research and teaching software tool for plane-parallel radiative transfer in the earth's atmosphere. *Bulletin of the American Meteorological Society*, 79(10):2101–2114, 1998.

B. Ridley, J. Boland, and P. Lauret. Modelling of diffuse solar fraction with multiple predictors. *Renewable Energy*, 35(2):478–483, 2010.

C. Rigollier, M. Lefèvre, and L. Wald. The method Heliosat-2 for deriving shortwave solar radiation from satellite images. *Solar Energy*, 77(2):159–169, 2004.

S. Rodríguez, R. Van Dingenen, J.P. Putaud, A. Dell'Acqua, J. Pey, X. Querol, A. Alastuey, S. Chenery, K.F. Ho, R. Harrison, et al. A study on the relationship between mass concentrations, chemistry and number size distribution of urban fine aerosols in milan, barcelona and london. *Atmospheric Chemistry and Physics*, 7(9):2217–2232, 2007.

D.M. Roessler. Photoacoustic insights on diesel exhaust particles. *Applied optics*, 23(8):1148–1155, 1984.

M.W. Rotach and D. Zardi. On the boundary-layer structure over highly complex terrain: Key findings from MAP. *Quarterly Journal of the Royal Meteorological Society*, 133(625):937–948, 2007.

P.D. Safai, M.P. Raju, R.S. Maheshkumar, J.R. Kulkarni, P.S.P. Rao, and P.C.S. Devara. Vertical profiles of black carbon aerosols over the urban locations in south india. *Science of the Total Environment*, 431:323–331, 2012.

A. Saha, M. Mallet, J.C. Roger, P. Dubuisson, J. Piazzola, and S. Despiau. One year measurements of aerosol optical properties over an urban coastal site: Effect on local direct radiative forcing. *Atmospheric Research*, 90(2):195–202, 2008.

B.H. Samset, G. Myhre, M. Schulz, Y. Balkanski, S. Bauer, T.K. Berntsen, H. Bian, N. Bellouin, T. Diehl, R.C. Easter, et al. Black carbon vertical profiles strongly affect its radiative forcing uncertainty. *Atmospheric Chemistry and Physics*, 13:2423–2434, 2013.

G. Sangiorgi, L. Ferrero, M.G. Perrone, E. Bolzacchini, M. Duane, and B.R. Larsen. Vertical distribution of hydrocarbons in the low troposphere below and above the mixing height: Tethered balloon measurements in milan, italy. *Environmental Pollution*, 159(12):3545–3552, 2011.

R. Saunders, M. Matricardi, and P. Brunel. An improved fast radiative transfer model for assimilation of satellite radiance observations. *Quarterly Journal of the Royal Meteorological Society*, 125(556):1407–1425, 1999.

O. Schmid, P. Artaxo, W.P. Arnott, D. Chand, L.V. Gatti, G.P. Frank, A. Hoffer, M. Schnaiter, and M.O. Andreae. Spectral light absorption by ambient aerosols influenced by biomass burning in the amazon basin. i: Comparison and field calibration of absorption measurement techniques. *Atmospheric Chemistry and Physics*, 6(11):3443–3462, 2006.

T. Schumann. On the use of a modified clean-room optical particle counter for atmosperic aerosols at high relative humidity. *Atmospheric Research*, 25(6): 499–520, 1990.

J.P. Schwarz, R.S. Gao, D.W. Fahey, D.S. Thomson, L.A. Watts, J.C. Wilson, J.M. Reeves, M. Darbeheshti, D.G. Baumgardner, G.L. Kok, et al. Single-particle measurements of midlatitude black carbon and light-scattering aerosols from the boundary layer to the lower stratosphere. *Journal of Geophysical Research: Atmospheres (1984–2012)*, 111(D16), 2006.

J.P. Schwarz, J.R. Spackman, R.S. Gao, L.A. Watts, P. Stier, M. Schulz, S.M. Davis, S.C. Wofsy, and D.W. Fahey. Global-scale black carbon profiles observed in the remote atmosphere and compared to models. *Geophysical Research Letters*, 37(18), 2010.

J.P. Schwarz, B.H. Samset, A.E. Perring, J.R. Spackman, R.S. Gao, P. Stier, M. Schulz, F.L. Moore, E.A. Ray, and D.W. Fahey. Global-scale seasonally resolved black carbon vertical profiles over the pacific. *Geophysical Research Letters*, 40(20):5542–5547, 2013.

J.H. Seinfeld and S.N. Pandis. *Atmospheric chemistry and physics: from air pollution to climate change*. John Wiley & Sons, 2012.

P.J. Sellers, D.A. Randall, G.J. Collatz, J.A. Berry, C.B. Field, D.A. Dazlich, C. Zhang, G.D. Collelo, and L. Bounoua. A revised land surface parameterization (SiB2) for atmospheric GCMs. part I: Model formulation. *Journal of climate*, 9(4):676–705, 1996.

P.J. Sellers, R.E. Dickinson, D.A. Randall, A.K. Betts, F.G. Hall, J.A. Berry, G.J. Collatz, A.S. Denning, H.A. Mooney, C.A. Nobre, et al. Modeling the exchanges of energy, water, and carbon between continents and the atmosphere. *Science*, 275(5299):502–509, 1997.

S. Serafin and D. Zardi. Daytime heat transfer processes related to slope flows and turbulent convection in an idealized mountain valley. *Journal of Atmospheric Science*, (67):3739–3756, 2010a.

S. Serafin and D. Zardi. Structure of the atmospheric boundary layer in the vicinity of a developing upslope flow system: A numerical model study. *Journal of Atmospheric Science*, (67):1171–1185, 2010b.

S. Serafin and D. Zardi. Daytime development of the boundary layer over a plain and in a valley under fair weather conditions: a comparison by means of idealized numerical simulations. *Journal of Atmospheric Science*, (68):2128–2141, 2011.

A. Skartveit and J.A. Olseth. A model for the diffuse fraction of hourly global radiation. *Solar Energy*, 38(4):271–274, 1987.

A. Skartveit, J.A. Olseth, and M.E. Tuft. An hourly diffuse fraction model with correction for variability and surface albedo. *Solar Energy*, 63(3):173–183, 1998.

J. Soares, A. P. Oliveira, M.Z. Božnar, P. Mlakar, J.F. Escobedo, and A.J. Machado. Modeling hourly diffuse solar-radiation in the city of são paulo using a neural-network technique. *Applied energy*, 79(2):201–214, 2004.

R. Spurr. LIDORT and VLIDORT: Linearized pseudo-spherical scalar and vector discrete ordinate radiative transfer models for use in remote sensing retrieval problems. *Light Scattering Reviews 3*, pages 229–275, 2008.

K. Stamnes, S.C. Tsay, K. Jayaweera, W. Wiscombe, et al. Numerically stable algorithm for discrete-ordinate-method radiative transfer in multiple scattering and emitting layered media. *Applied Optics*, 27(12):2502–2509, 1988.

K. Stamnes, S.C. Tsay, W. Wiscombe, and I. Laszlo. *DISORT, a general-purpose Fortran program for discrete-ordinate-method radiative transfer in scattering and*

emitting layered media: documentation of methodology. Goddard Space Flight Center, NASA, 2000.

P. Stier, J.H. Seinfeld, S. Kinne, and O. Boucher. Aerosol absorption and radiative forcing. *Atmospheric Chemistry and Physics*, 7(19):5237–5261, 2007.

T.F. Stocker, D. Qin, G.K. Plattner, M. Tignor, S.K. Allen, J. Boschung, A. Nauels, Y. Xia, B. Bex, and B.M. Midgley. Ipcc, 2013: climate change 2013: the physical science basis. contribution of working group i to the fifth assessment report of the intergovernmental panel on climate change. 2013.

R. Stöckli. The HelioMont Surface Radiation Processing. Scientific Report Meteoswiss, 93, 119 pp., Federal Office of Meteorology and Climatology, MeteoSwiss, 2013a.

R. Stöckli. *The HelioMont surface solar radiation processing.* Bundesamt für Meteorologie und Klimatologie, MeteoSchweiz, 2013b.

R Subramanian, Neil M Donahue, Anna Bernardo-Bricker, Wolfgang F Rogge, and Allen L Robinson. Insights into the primary–secondary and regional–local contributions to organic aerosol and pm 2.5 mass in pittsburgh, pennsylvania. *Atmospheric Environment*, 41(35):7414–7433, 2007.

S.N. Tripathi, A.K. Srivastava, S. Dey, S.K. Satheesh, and K. Krishnamoorthy. The vertical profile of atmospheric heating rate of black carbon aerosols at kanpur in northern india. *Atmospheric Environment*, 41(32):6909–6915, 2007.

W.J. Trompetter, S.K. Grange, P.K. Davy, and T. Ancelet. Vertical and temporal variations of black carbon in new zealand urban areas during winter. *Atmospheric Environment*, 75:179–187, 2013.

E. Weingartner, H. Saathoff, M. Schnaiter, N. Streit, B. Bitnar, and U. Baltensperger. Absorption of light by soot particles: determination of the ab-

sorption coefficient by means of aethalometers. *Journal of Aerosol Science*, 34 (10):1445–1463, 2003.

Wikipedia. Electromagnetic radiation — wikipedia, the free encyclopedia, 2015. URL \url{http://en.wikipedia.org/w/index.php?title= Electromagnetic_radiation&oldid=651028669}.

D. S. Wilks. *Statistical methods in the atmospheric sciences*, volume 91 in the International Geophysisc Series. Academic press, 2011.

World Meteorological Organization World Meteorological Organization. *Guide to meteorological instruments and methods of observation. N. 8, Seventh Edition.* World Meteorological Organization, 2008.

C.M. Zarzycki and T.C. Bond. How much can the vertical distribution of black carbon affect its global direct radiative forcing? *Geophysical Research Letters*, 37(20), 2010.

Y. Zhang, C. Seigneur, J.H. Seinfeld, M. Jacobson, S.L. Clegg, and F.S. Binkowski. A comparative review of inorganic aerosol thermodynamic equilibrium modules: similarities, differences, and their likely causes. *Atmospheric Environment*, 34 (1):117–137, 2000.